The Paton WELDING JOURNAL

January 2000 # 1

English translation of the monthly «Avtomaticheskaya Svarka» journal published in Russian since 1948

«The Paton Welding Journal» monthly is published by the E.O. Paton Electric Welding Institute of the National Academy of Sciences of Ukraine with the support rendered by the International Association «Welding».

Promotion group:
V.N.Lipodaev, V.I.Lokteva
A.T.Zelnichenko (Exec. director)

Editorial and advertising offices are located at PWI, Dept. 51, 11, Bozhenko str., 252650, Kyiv, Ukraine.
Tel.: (38044) 227 67 57
Fax: (38044) 268 04 86
E-mail: paton@i.kiev.ua; paton@iptelecom.net.ua

Subscriptions:
$460, 12 issues

«The Paton Welding Journal» Website: http://www.nas.gov.ua/pwj

CONTENTS

CONTRACTION OF THE WELDING ARC CAUSED BY THE FLUX IN TUNGSTEN-ELECTRODE ARGON-ARC WELDING

B.E. PATON[1], V.N. ZAMKOV[1], V.P. PRILUTSKY[1] and P.V. PORITSKY[2]
[1]The E.O. Paton Electric Welding Institute, NASU, Kyiv, Ukraine
[2]Institute for Nuclear Research, NASU, Kyiv, Ukraine

ABSTRACT

The theoretical model developed to describe contraction of the arc by flux allows for the processes occurring at the anode, variations in thermal conductivity of the arc gas and phenomena taking place on the arc column periphery, and establishes their analytical relationship with size of the conducting arc plasma column and the anode spot. Distribution of current density in the anode spot determined by analytical calculations using the said model is close to that determined by experimental measurements.

Key words: *welding over the flux layer, arc, tungsten electrode, anode, plasma, thermal conductivity, negative ions, current density.*

There are many publications [1 – 8] describing investigations of causes of an increase in the penetrating power of the arc in TIG welding over the flux layer*. Analysis of the results shows that parameters of the welds and primarily the penetration depth can be affected by varying chemical composition of the flux. Thus, other conditions being equal, the maximum penetration depth can be increased 3 – 4 times, as compared with welding using no flux. At the same time, this causes changes in spatial characteristics and electrical parameters of the arc. The objective of this work was to develop a model to describe causes of contraction of the argon welding arc by adding to the welding zone the appropriate fluxes, limitations on size of the weld pool and region of existence of the anode spot.

Melting of metal and formation of the weld pool can occur only in the case where the flux is fully removed from under the arc column root either by evaporation or by forcing out the molten flux to expose the metal, which was before covered with the flux, under the effect of the gas-dynamic plasma and shielding gas flows. This is proved by the fact that at an insufficient welding current and at a substantial thickness of the flux layer, where pressure on the anode is too low to force out the flux, the metal is not melted. As electrical conductivity of the molten flux is lower than that of the metal, the region of existence of the anode spot (irrespective of the arc length [9]) is limited by size of the weld pool. It has been experimentally proved that the basic factors determining the surface area from which the flux is forced out are as follows: adhesive properties of the flux with regard to the metal welded and ability of the vapours formed during evaporation of the flux from the anode surface to cause contraction of the arc column.

The better the flux wets the metal welded, the closer the flux melt located on the metal surface to the arc axis (under constant welding conditions) and the smaller the area of the weld pool and the region of existence of the anode spot. As adhesion of a liquid to the solid substrate is in direct dependence upon the Gibbs energy ΔG° for chemical reaction of interaction between them, ΔG° can be used as the criterion for evaluation of the efficiency of materials in terms of their use as the fluxes or their components [2].

Spectroscopic investigations of the arc in TIG welding over the flux layer showed the presence in the arc gap of vapours of the flux and its dissociation products, and an increase in the intensity of lines of the base metal vapours, as compared with welding using no flux [10, 11]. In addition, products of chemical reactions between the flux and base metal were detected in the arc spectra [10]. It should be noted that luminescence of molecular lines, as well as atomic and ionic lines of the flux and base metal vapours is seen only in the peripheral zones of the arc discharge, whereas the central part of the discharge is an almost pure argon plasma, containing no impurities, like in welding using no flux [12, 13]. All these experimental data allowed an unambiguous conclusion that changes in spatial characteristics and electrical parameters of the arc, contraction of the arc column and increase in the current density at the anode in particular, caused by the flux present in the welding zone, were a result of a set of the inter-related and inter-dependent processes occurring at the anode and in the arc gap.

It is a known fact that the electric arc discharge occurs in the gas channel (plasma) which is characterized by electrical conductivity. Conductivity of the arc plasma is a result of thermal ionization that takes place at relatively high temperatures, as compared with the temperature of the electrodes. This is accompanied by the establishment of balance between the heat released in the plasma because of a flow of the electric current and the electric energy removed as a result of thermal conductivity into the electrodes and the surrounding atmosphere. Spatial characteristic of the arc and distribution of the current density in it depend upon the thermal balance conditions. So, relationships between parameters of the discharge for different conditions can be found by calculations and by analysing a character of distribution of the current density across the discharge section.

Contraction of the discharge takes place if the following conditions are met [14 – 18]: (1) bulk neutralization

*In some publications the method of TIG welding over the flux layer is called A-TIG welding.

of the charged particles dominates their diffusion drift to walls of the discharge chamber; (2) frequency of formation of the charged particles dramatically decreases from axis to walls of the chamber. In this case the degree of contraction of the discharge depends upon non-uniformity of the temperature across its section. Thermal contraction is caused in particular by the fact that temperature at the periphery of the discharge falls and the gas density (under constant pressure) rises. Therefore, electrons at the periphery give up a larger amount of the energy to neutral particles and their temperature falls, which in turn leads to a decrease in the concentration of electrons because of intensification of the recombination processes. It should be noted that with this welding method there is a probability that particles with a large effective cross section of capture of electrons [2, 6, 19, 20] and long-life negative ions may be formed in vapours of the halide fluxes. Their presence leads to an increase in contraction of the arc column [14 – 16] and thermal capacity per unit surface area of the anode heating spot. Thus, the problem is reduced to establishing an analytical dependence of characteristics of the discharge, size of the weld pool and region of existence of the anode spot of the arc upon the effect of the molten flux at the anode and its vapours in the arc gap.

Processes occurring at the anode surface and in the anode region of the arc

Figure 1 shows schematic of the arc discharge under consideration. It is assumed that the problem has a cylindrical symmetry statement and the processes occurring within the welding zone are quasi-stationary.

At the moment of excitation of the arc discharge the flux starts melting under the arc but, as was already noted [1, 2], the weld pool can be formed only with the flux forced out from under the arc column root and from the base metal surface. This takes place as a result of the force action of the arc, F_{arc}, which is formed in the anode region by a flow of electrons, F_e, and complemented by the reactive force induced by the anode material vapours, F_{rm}.*

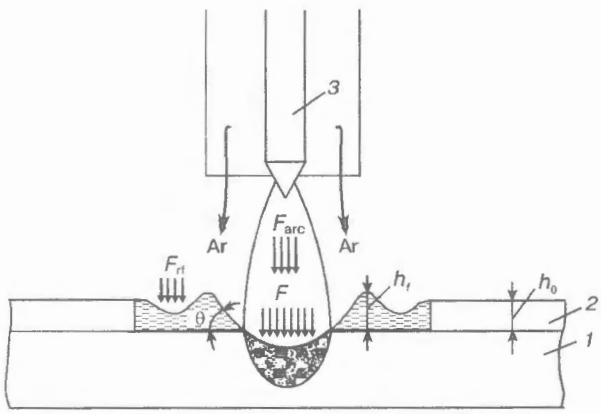

Figure 1. Schematic of the arc discharge in welding over the flux layer: *1* — base metal; *2* — flux; *3* — electrode.

*The gas-dynamic flow of a shielding gas can exert the extra action on the anode, depending upon specific welding conditions.

The action of these forces that press out the flux is hampered by adhesion between the molten flux and the solid metal, pressure of the molten flux layer h_f thick at the weld pool boundary (Archimedean force F_{Arh}) and a reactive force induced by the evaporating flux around the weld pool, F_{rf}. Note that h_f is normally much in excess of thickness of the initially deposited flux layer, h_0, because of the effect of hydro- and gas-dynamic flows formed around the weld pool.

In a general form, the balance of forces at the weld pool boundary can be written as follows:

$$\sum_l F_l = \Delta \sigma \cos \theta , \qquad (1)$$

where $\sum_l F_l \approx F_e + F_{rm} - F_{Arh} - F_{rf} \approx F_e + F_{rm} - \rho_f g h_f$,

ρ_f is the density of the molten flux, σ is the surface tension of the molten flux, g is the free fall acceleration, $\Delta = 2 \pi R_A$ is the perimeter of the weld pool or region of existence of the anode spot (R_A — radius of this region) and θ is the contact angle in wetting the anode surface with the molten flux.

It follows therefrom that

$$R_A = \frac{\sum_l F_l}{2 \pi \sigma \cos \theta} . \qquad (2)$$

Expression (2) establishes dependence of R_A upon the force factors acting within the welding zone. Analysis of this dependence allows a conclusion that, other conditions being equal, R_A is determined by physical-chemical properties of the flux and base metal. Radius of the region of existence of the anode spot decreases with an increase in wetting the base metal with the molten flux and with an increase in its surface tension, density and amount (i.e. thickness of the deposited layer).

For quantitative estimation of the effect of fluxes on R_A, first of all it is necessary to determine the force effect of the arc, F_{arc}, and metal vapours, F_{rm}, on the anode, which can be calculated from the corresponding pressures applied to the anode. For this, we will use an expression from [21] for the pressure exerted by the flow of electrons on the anode:

$$p_e = j(r) \sqrt{\frac{m_e (2 e U_{and} - 3 k T_{and})}{e^2}} , \qquad (3)$$

where $j(r)$ is the current density near the anode as a function of distance r from the discharge axis, U_{and} is the anode voltage drop, T_{and} is the anode surface temperature, m_e is the electron mass, e is the electron charge and k is the Boltzmann's constant.

The reactive pressure of vapours of the base metal acting on the anode can be expressed as follows:

$$p_{rm} = \frac{\varphi_M^2}{m_M n_M} j(r) , \qquad (4)$$

where m_M is the mass of a molecule of the material being evaporated, n_M is its concentration, and the value of φ_M

characterizes properties of the base metal and can be calculated from the following formula:

$$\varphi_M = \frac{k_{evp}\,(U_{and} + U_{\varphi\,,\,and})\,\mu_{and}}{(E_{s\,,\,and} + E_{i\,,\,and} - H_{lq})}. \qquad (5)$$

Here $U_{\varphi\,,\,and}$; $E_{s\,,\,and}$; $E_{i\,,\,and}$ and H_{lq} are the electronic work function, sublimation energy, ionization potential and heat content at a boiling temperature of the anode material, respectively, μ_{and} is the atomic number of the anode material and k_{evp} is the share of the power consumed for evaporation.

Then, assuming the presence of equilibrium at the boundary of the weld pool, $r = R_A$, the following equation can be derived to determine the value of R_A:

$$\rho_f g\, h_f + \frac{2\,\sigma \cos\theta}{r} = \qquad (6)$$

$$= j\,(r)\left(\sqrt{\frac{m_e\,(2e\,U_{and} - 3\,k\,T_{and})}{e^2}} + \frac{\varphi_M^2}{m_M\,n_M}\,j\,(r)\right).$$

Note that p_e, p_{rm} and, hence, R_A are the functions of a spatial distribution of the current density, $j\,(r)$, across the section of the arc discharge near the anode, i.e. they depend upon spatial characteristics of the arc. On the other hand, the very formation of molecular vapours of the flux and products of its interaction with the base metal [3, 4] in the arc gap causes changes in distribution of the current density and other parameters across the arc discharge section. Additions of the molecular gas to the arc gap cause changes in a character of the processes that take place there. It is a known fact [19, 22, 23] that inelastic processes, such as transitions between oscillation and rotation levels of the molecules, dissociation of molecules and association of atoms (molecule formation), as well as chemical reactions (in the gas mixture) become essential in the molecular gases. The inelastic processes lead to a change in the internal energy of the particles and thus affect the energy transfer (thermal conductivity). The excited particles move to the region with a lower temperature and there transfer their internal energy to the translational levels of freedom, thus enhancing the energy transfer. This leads to an increase in thermal conductivity and, hence, intensifies contraction of the discharge.

The processes of formation of negative ions can also play an important role in contraction of the discharge in the anode region [19, 24, 25]. This is associated with the fact that all the currently known fluxes intended for welding over the flux layer are based on halides, oxides or their mixtures, i.e. materials that contain electrically negative elements.

In gases containing electrically negative elements (molecules or radicals) the basic mechanism of neutralization is associated with electrons sticking to them. In this case, neutralization of the charged particles occurs successively in two stages:

$$e + Ng \rightarrow Ng^-, \qquad (7)$$

$$Ng^- + Ng^+ \rightarrow 2Ng, \qquad (8)$$

where the process of sticking (7) normally takes place with the participation of a third particle (Ng^- — electrically negative particle).

If the discharge takes place in a gas containing the electrically negative additions, the resulting negative ions recombine with the positive ions A^+ of the basic component:

$$Ng^- + A^+ \rightarrow X + Y, \qquad (9)$$

where, in a general case, X and Y are the neutral particles: atoms, molecules or complexes.

As in this case the processes described in (7) to (9) occur against the background of other processes of recombination of the charged particles, the electrically negative impurities present in the discharge lead to an extra decrease in size of the region occupied by the discharge, as compared with the case where there are no such impurities.

It should be noted that of the highest interest in terms of formation of negative ions are complex halogen-containing molecules or radicals [19]. The general principles of formation of the negative ions [24, 25] include increase in the effective cross section of adhesion with a decrease in the energy of electrons and the life time of a negative ion, as the temperature falls and pressure rises. Therefore, the formation of the negative ions as a result of capture of the conduction electrons will be more probable in the cooler peripheral regions of the arc, which also cannot but exert a substantial effect on distribution of the current density across the section.

Contraction of the positive arc column

Consider plasma of the positive column of a cylindrical arc discharge, in which a local, including ionization, thermodynamic equilibrium is maintained. Assume that electronic thermal conductivity and inelastic losses of electrons are small, as compared with Joule heating and elastic losses of electrons. Ignore the radiant transfer of the energy, as, according to the data in [21], the radiation losses in the welding arcs are no more than 5 % of the power. At the same time, note that this situation is true for the welding arc burning with a metal (consumable) electrode, where temperature T of the arc discharge is not higher than 12,000 K. At the higher temperatures the radiation losses will increase, and at $T \sim 20{,}000$ K they can amount to 30 % of the total heat balance [26]. In our case the arc temperature is 14,000 – 16,000 K and the radiation losses are much lower. Ignore also the Coulomb collisions, assuming that ionization of the plasma is low: $k\,T << e\,U_{i,\,eff} = E_{i\,,\,eff}$, where $U_{i\,,\,eff}$ is the effective ionization potential of the gas and $E_{i\,,\,eff}$ is the corresponding ionization energy. Assuming that the intensity of heat release is proportional to the local current density and the electron and gas temperatures are equal to each other, the heat transfer equation can be written as follows:

$$\frac{1}{r}\frac{d}{dr}\left(r\chi(T)\frac{dT}{dr}\right)+q(r)=0, \quad (10)$$

where r is the distance from the discharge axis, $\chi(T)$ is the coefficient of thermal conductivity, $q(r)=j(r)E$ is the power of heat release per unit volume, $j(r)=\sigma_e E$ is the electric current density, E is the electric field intensity and σ_e is the conductivity of the plasma. The following boundary conditions are selected: temperature at the discharge axis is $T(0)=T_0$ and that at infinity is $T(\infty)=T_\infty$*.

Write down the coefficient of thermal conductivity in the following form:

$$\chi=\chi_{elst}+\chi_{int}, \quad (11)$$

where χ_{elst} related to the energy transfer by the translation degree of freedom is assumed to be equal to the coefficient of thermal conductivity of argon, $\chi_{ar}(T)$, obeying the following dependence [7]:

$$\chi_{ar}(T)=\chi_*\left(\frac{T}{T_*}\right)^{0.68}, \quad (12)$$

($\chi_*=4.2\times10^{-2}$ W/(m×K), $T_*=1000$ K) and χ_{int} caused by the energy transfer at the internal degrees of freedom can be written as follows:

$$\chi_{int}=\chi_{ros}+\chi_b. \quad (13)$$

Here χ_{ros} is associated with processes occurring at the rotation and oscillation degrees of freedom and χ_b is caused by the processes of splitting of the particles.

Under conditions of the considered arc welding process [1 – 5] the density of particles of the impurity molecular gas, n_f, in argon is low, as compared with the density of the working gas, n_0. Thus, the χ_{ros} value cannot be neglected, as $(\chi_{ros}/\chi_{elst})\sim(n_f/n_0)$. The processes of dissociation of molecules and subsequent ionization of atoms (even at a small concentration of the impurity) can cause a fundamental increase in thermal conductivity. This is related to the fact that, during splitting, a particle transfers the energy which is much in excess of the thermal energy of the particles. In turn, the value of χ_b can be written as the sum of the dissociation (index d) and ionization (index i) contributions:

$$\chi_b=\chi_d+\chi_i. \quad (14)$$

Limit our consideration to a case of relatively low temperatures when $E_D >> kT$ and $E_i >> kT$, where E_D is the energy of dissociation of the molecules and E_i is the ionization potential. Then, for the case of dissociation of a two-atomic perfect gas, χ_d can be approximately calculated from the following formula [23]:

$$\chi_d\approx\frac{D_f p_f}{T}\frac{\alpha_d(1-\alpha_d)}{(2-\alpha_d)}\left(\frac{E_D}{kT}\right)^2, \quad (15)$$

where D_f is the diffusivity of the impurity in the working gas, p_f is the partial pressure of the dissociating gas (molecular impurity), $\alpha_d=\frac{n_{f,a}}{n_M+n_{f,a}}$ is the degree of dissociation, n_M is the density of the molecules and $n_{f,a}$ is the density of the dissociated atoms.

The equation of the reaction of an equilibrium dissociation of the impurity gas molecule $M \rightleftarrows X+Y$ will have the following form:

$$\frac{\alpha_d^2}{1-\alpha_d^2}=\Xi_d(T;M,X,Y)=$$

$$=\frac{L_X L_Y}{L_M}\left(\frac{2\pi m_X m_Y kT}{m_M h^2}\right)^{3/2}\frac{kT}{p_f}\exp\left(\frac{E_D}{kT}\right), \quad (16)$$

where $\alpha_d=\frac{n_X}{n_M+n_Y}$ is the degree of dissociation of the impurity gas, n_l, L_l and m_l $\{l=M,X,Y\}$ are the densities, statistic weights and masses of the particles, respectively and h is the Planck's constant.

Hence, the degree of the equilibrium dissociation is

$$\alpha_d=(1+\Xi_a^{-1}(T))^{1/2}. \quad (17)$$

Accordingly, the contribution of ionization to thermal conductivity can be calculated from the following equation:

$$\chi_i\approx\frac{D_{amb}p_g}{T}\frac{\alpha_i(1-\alpha_i)}{(2-\alpha_i)}\left(\frac{E_i}{kT}\right)^2, \quad (18)$$

where D_{amb} is the coefficient of ambipolar diffusion, p_g is the gas pressure and α_i is the degree of ionization.

Under conditions of TIG welding in argon over the flux layer, the products of dissociation of the flux vapours can be atoms of metals, halogen- or oxygen-containing radicals, molecules or atoms of oxygen and halogens. Metals have lower ionization potentials. That is why they should play the basic role in the ionization processes. Further on, we will consider the case of the impurity of alkali metal halide MeG as the most versatile component of the flux, which is dissociated by the following reaction: MeG → Me + G. As a rule, by the beginning of ionization the two-atomic gas is almost completely dissociated. Therefore, the basic effect on properties of the arc gas can be exerted by ionization of atoms of alkali metal that has a much lower ionization potential than halogens and argon. The ionization potential of atoms of halogens (as well as oxygen) is close to that of argon. That is why, in our case the ionization processes are insignificant.

Limit our consideration to an assumption that the arc plasma has only one type of the singly charged ions, positive (A^+, index p) or negative (Ng^-, index n). The density of electrons at a given point of the discharge is related to the densities of neutrals $n_a\approx n_0$, positive and negative singly charged ions n_p and n_n ($n_n\le n_{Ng}$, where n_{Ng} is the density of the electrically negative particles) by the Sach equations:

*T_∞ corresponds to the temperature of the discharge chamber walls in the experiment (≈ 300 K); therefore, allowing for a significant difference of temperatures at the discharge axis (15,000 – 20,000 K), T_∞ can be assumed to be equal to zero without any loss of generality.

$$\frac{n_e n_p}{n_a} = \frac{2 L_p}{L_a}\left(\frac{2\pi m_e k T}{h^2}\right)^{3/2} \exp\left(-\frac{E_{i,\,eff}}{kT}\right), \quad (19)$$

$$\frac{n_e n_{Ng}}{n_n} = \frac{2 L_{Ng}}{L_n}\left(\frac{2\pi m_e k T}{h^2}\right)^{3/2} \exp\left(-\frac{E_A}{kT}\right), \quad (20)$$

where L_l $\{l = p, a, Ng, n\}$ are the statistic weights for a positive ion, neutral atom, electrically negative particle and negative ion, respectively, E_A is the energy of affinity for electron and n_e is the electron density.

The effective energy of ionization of the arc gas at temperature T is determined as

$$E_{i,\,eff} = -2\,k\,T \ln \sum_l \left(\frac{n_l}{n}\right)^{1/2} \exp\left(-\frac{E_{i,l}}{kT}\right), \quad (21)$$

where n_l and $E_{i,\,l}$ are the concentration and energy of ionization of the gas components. On the other hand, the effective temperature of the arc is related to the ionization energy (potential) by a certain dependence [21]. This makes it possible to determine the values of $E_{i,\,\text{eff}}$ and T_{arc} for specific conditions of the discharge.

Proceeding from (17) and (18) and allowing for the condition of constant pressure $p = n\,k\,T = \sum_l n_l\,k\,T$ across the section of the arc discharge, as well as the law of conservation of the electric charge

$$n_e + n_n = n_p, \quad (22)$$

we will obtain:

$$\frac{n_e}{n_0} = \bar{\omega}\ (T)\left(\frac{2 L_i}{L_a}\right)^{1/2}\left(\frac{2\pi m_e}{h^2}\right)^{3/4} \times$$

$$\times\,(k\,T)^{5/4}\,p^{-1/2} \exp\left(-\frac{E_{i,\,eff}}{2\,kT}\right). \quad (23)$$

Here, function

$$\bar{\omega}\ (T) = \left(1 + \frac{p_{Ng} \exp\left(\frac{E_A}{kT}\right)}{\left(\frac{2 L_{Ng}}{L_n}\right)\left(\frac{2\pi m_e}{h^2}\right)^{3/2} (k\,T)^{5/2}}\right)^{-1/2} \quad (24)$$

determines a decrease in the amount of electrons in the presence of the negative ions (p_{Ng} — partial pressure of the gas of the electrically negative particles). It follows therefrom that under the conditions characteristic of the experiments [2, 20], where $p_{Ng} \le 0.2 - 1.2$ kPa, the effect of the electrically negative particles on contraction of the discharge will show up in the peripheral region, where $T \le 4000$ K, and can be essential only in the presence of particles with the affinity energy of $E_A > 1 - 2$ eV. Allowing for the character of dissociation of the impurity, for the calculations the pressure of the electrically negative particles can be assumed to be equal to $p_{\text{Ng}} = p_f / 2$.

Introduce now a dimensionless parameter

$$\varepsilon = \frac{[T(0) - T(r)]\,E_i}{2\,k\,T^2(0)}. \quad (25)$$

Then, according to formula (23), $n_e(r) = n_e(0)\,\bar{\omega} \times$ $\times\,(\varepsilon) \exp(-\varepsilon)$. Accordingly, the current density and the heat release power in equation (10) will vary across the section in the following manner: $j(r) = j_0\,\bar{\omega}\,(\varepsilon) \exp(-\varepsilon)$ and $q(r) = q_0\,\bar{\omega}\,(\varepsilon) \exp(-\varepsilon)$, where $j_0 = j(0)$ and $q_0 = q(0)$. As it can be seen, parameters of the plasma, including the density of electrons, vary markedly with a small variation in temperature. Therefore, in the region of the plasma which determines its electrical conductivity and energy balance, the temperature will vary but slightly.

As in equation (10) the strongest dependence upon r is of an exponential character, to solve it, we will assume all the coefficients of derivatives to be constant and equal to those at the discharge axis.

By introducing the dimensionless variable

$$x = \left(\frac{r}{r_0}\right)^2, \quad (26)$$

where

$$r_0^2 = \frac{16\,\chi_0\,k\,T_0^2}{q_0\,E_{i,\,eff}}, \quad (27)$$

and allowing for formula (23), we reduce the heat balance equation (10) to the following form:

$$\frac{d}{dx}\left(x\,\frac{d\varepsilon}{dx}\right) - \exp(-\varepsilon) = 0. \quad (28)$$

The equation obtained has the following solution:

$$\varepsilon = 2 \ln [1 + x], \quad (29)$$

which corresponds to the following distribution of the electron density across the section:

$$n_e(r) = n_e(0)\,\bar{\omega}\,(\varepsilon) \exp(-\varepsilon) = \\ = n_e(0)\,\bar{\omega}\,(r)\,f(r), \quad (30)$$

where

$$f(r) = \frac{1}{(1 + (r/r_0)^2)^2}. \quad (31)$$

The temperature, current density and energy release distributions will be described by the similar dependencies. Thus, it holds for the current density

$$j(r) = j_0\,\bar{\omega}\,(\varepsilon) \exp(-\varepsilon) = j_0\,\bar{\omega}\,(r)\,f(r). \quad (32)$$

As q_0 is in inverse proportion to r_0, the energy density in the plasma will grow as its conductivity region decreases.

Based on the obtained dependencies of the considered plasma parameters upon the radius, and allowing for the fact that the effect of negative ions shows up mostly at

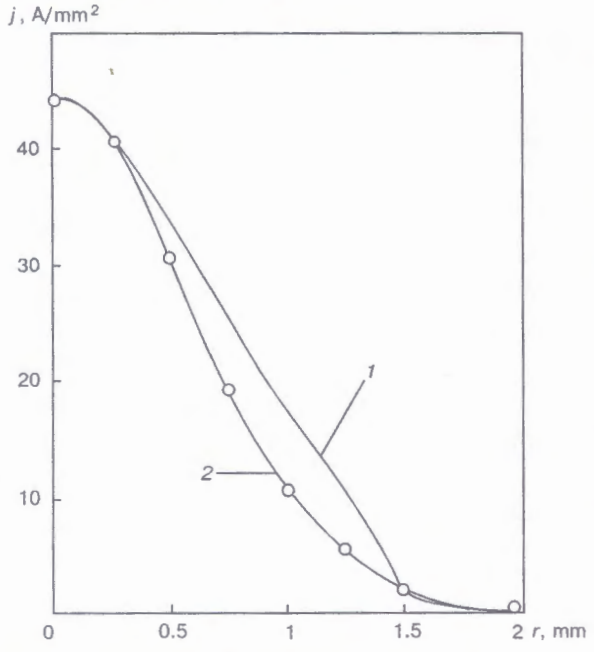

Figure 2. Distribution of the current density, $j(r)$, in the anode region of the positive arc column: *1* — calculation; *2* — experiment.

the periphery of the discharge, we will have that the effective values of these parameters of the arc discharge are related to the corresponding values at the arc axis by a proportionality coefficient of ≈ 0.785.

Estimate the value of the r_0 parameter, which can be interpreted as a characteristic radius of contraction of the positive arc column for conditions of welding titanium using sodium fluoride (NaF) as the flux. For this case, the experimental data on the distribution of the current density in the anode region of the arc are available [3]. This makes it possible to compare the calculation results and evaluate correctness of our theoretical model describing the effect of the flux on the welding arc. As it is shown in [12, 13], since the vapours formed during welding do not enter the arc column, we assume that the effective ionization potential in it is equal to the ionization potential of argon $E_{i,\,\text{eff}} \approx 15.75$ eV, which corresponds to the effective temperature of the arc $T_{\text{arc}} \approx 12{,}000$ K and temperature at the axis $T_0 \approx \dfrac{T_{\text{arc}}}{0.785} \approx 15{,}000$ K. Then we assume that the partial pressure of the vapours is $p_f = 1.2$ kPa and the ratio of the statistic weights is $a^2 = 4$. To estimate the total coefficient of thermal conductivity of the arc gas, the coefficients of mutual [26] and ambipolar [17] diffusion (cm^2 / s) are calculated from the following formulae:

$$D_f(T) = 0.17\left(\frac{T}{273}\right)^{1.752}, \qquad (33)$$

$$D_{\text{amb}}(T) = 3.4\left(\frac{T}{1000}\right)^{1.2}\frac{2}{\left(n_a / 10^{18}\right)}, \qquad (34)$$

where the temperature is expressed in Kelvin and n_a in cm^{-3}.

At $q_0 \approx 2\times10^{10}$ W/m^3 (which corresponds to a welding current of 100 A) and $T_0 \approx 15{,}000$ K, the estimated value of $r_0 \approx 1.3$ mm. Figure 2 shows dependencies of distribution of the current density in the arc column, which were calculated for our conditions from formula (32), as well as experimental data taken from [3]. Here we have a satisfactory agreement between the calculated and experimental data. The difference we see in course of the curves of the current density distribution is likely to be caused by the effect of the radiant transfer, which was not taken into account in the model of the discharge under consideration.

Size of the weld pool and region of existence of the anode spot

Given that the current density is determined by dependence (32), equation (6) for determination of the value of $r = R_A$ can be re-written in the following form:

$$\rho_f g\, h_f + \frac{2\,\sigma\cos\theta}{r} = j_0\,\bar{\omega}\;(r)\,f(r)\times \qquad (35)$$

$$\times\left(\frac{\sqrt{m_e\,(2\,e\,U_{\text{and}} - 3\,k\,T_{\text{and}})}}{e^2} + \frac{\varphi_M^2}{m_M\,n_M}\,j_0\,\bar{\omega}\;(r)\,f(r)\right).$$

The value of φ_M (kg / A) can be calculated from the following formula (see [20]):

$$\varphi_M = \frac{k_{\text{evp}}\,(U_{\text{and}} + U_{\varphi,\,\text{and}})\,\mu_{\text{and}}}{(9.4\times10^4\,T_{k,\,\text{and}} + 9.65\times10^7\,U_{i,\,\text{and}} - H_{\text{lq}})}, \qquad (36)$$

where $U_{i,\,\text{and}}$ is the ionization potential of the anode material, V; $T_{k,\,\text{and}}$ is the boiling temperature of the anode material, K, and H_{lq} is expressed in J / (kg / mole).

The anode voltage drop, V, can be approximately determined [20] from the following expression:

$$U_{\text{and}} = 6.8\times10^{-4}\,\frac{\bar{T}_{\text{and}}^{1.5}\,\Delta T^{3.5}\,I_{\text{arc}}^{2.15}\,S_e^{7.15}}{U_{i,\,\text{eff}}^{19.15}\,a^{4.15}\,S_g^{3.5}\,\mu_{\text{and}}^{3.10}}, \qquad (37)$$

where $\bar{T}_{\text{and}} = \dfrac{T_{\text{arc}} + T_{\text{and}}}{2}$ is the average temperature of the anode region, K; T_{arc} is the average temperature of the arc, K; $\Delta T = T_{\text{arc}} - T_{k,\,\text{and}}$, K; I_{arc} is the arc current, A; S_e and S_g are the sections of collisions of the particles (atoms or molecules) of the arc gas with electrons and with each other, m^2; and a^2 is the ratio of the statistic weights. Substituting the values of the parameters characteristic of our conditions: $U_{i,\,\text{eff}} = 15.75$ V, $a^2 = 4$, $S_e = 2.5\times10^{-20}$ m^2, $S_g = 6.15\times10^{-20}$ m^2, $T_{\text{arc}} = 12{,}000$ K, $T_{\text{and}} = 1941$ K, $T_{k,\,\text{and}} = 3553$ K, $I_{\text{arc}} = 100$ A and $\mu_{\text{and}} = 47.9$, yields $U_{\text{and}} \approx 3.7$ V.

Assuming that $\rho_f = 1.95$ g/cm^3, $\sigma = 187$ MH/m, $\theta = \pi / 6$ ($\cos\theta \approx 0.86$), $h_f = 0.2$ mm, $r_0 = 1.3$ mm, $j_0 = 10^7$ A/m^2, $k_{\text{evp}} = 0.3$, $U_{\text{and}} = 3.7$ V, $U_{\varphi,\,\text{and}} = 3.95$ V, $U_{i,\,\text{and}} = 6.82$ V, $T_{\text{and}} = 1941$ K, $T_{k,\,\text{and}} = 3553$ K, $H_{\text{lq}} = 1.4\times10^8$ J/(kg/mole), $\mu_{\text{and}} = 47.9$, $m_M = 47.9$ amu $= 7.95\times10^{-26}$ kg and $n_M = 1\times10^{22}$ m^{-3}, we will have an es-

timate for the anode spot radius $R_A \approx 1.5$ mm, which is also in agreement with the experimental results.

CONCLUSIONS

Analysis of the results of experimental investigations of the arc in TIG welding of titanium in argon over the flux layer leads to an unambiguous conclusion that the flux effect on the arc consists in contraction of its positive column and the anode spot. This phenomenon is caused by a number of factors, such as: screening of metal around the weld pool by the liquid flux and stabilization of the anode spot within the limits of the weld pool, increase in thermal conductivity of the arc gas caused by impurities of the molecular vapours of the flux appearing in the arc, deionization of the peripheral regions of the arc as a result of capture of conduction electrons by the electrically negative particles of the flux vapours and products of interaction of the flux with the base metal.

The developed theoretical model of contraction of the arc by the flux, which allows for the above processes, makes it possible to analytically estimate sizes of the electrically conducting region of the arc column and the weld pool, and is in good agreement with the experimental results.

REFERENCES

1. Gurevich, S.M., Zamkov, V.N., Kushnirenko, N.A. (1965) Increase in the efficiency of penetration of titanium alloys in argon-arc welding. *Avtomaticheskaya Svarka*, **9**, 1 – 4.
2. Zamkov, V.N., Prilutsky, V.P., Gurevich, S.M. (1977) Effect of flux composition on the process of TIG welding of titanium. Ibid, **4**, 22 – 26.
3. Zamkov, V.N., Prilutsky, V.P. (1987) Distribution of current density in the anode spot in arc welding of titanium. Ibid, **3**, 19 – 22.
4. Savitsky, M.M., Gvozdetsky, V.S., Skrypnik, V.I. et al. (1979) Current density in the anode spot in welding conventional and refined steels. Ibid, **17**, 17 – 20.
5. Makara, A.M., Kushnirenko, B.N., Zamkov, V.N. (1968) Argon-arc welding of high-strength martensitic-grade steels using fluxes. Ibid, 7, 73 – 74.
6. Badianov, B.N., Davydov, V.A., Kolupaev, Yu.F., Tkachev, M.A. (1977) Variations in sizes of the zone of electrical conductivity of the arc caused by adding gaseous halides to argon. Ibid, **4**, 67 – 68.
7. Simonik, A.G. (1974) Effect of halides on penetration in argon-arc welding of titanium alloys. *Svarochnoye Proizvodstvo*, **3**, 52.
8. Simonik, A.G. Petriashvili, V.I., Ivanov, A.A. (1976) Effect of contraction of the arc discharge in adding electrically negative elements. Ibid, **3**, 49 – 51.
9. Mechev, V.S., Zamkov, V.N., Prilutsky, V.P. (1971) Radial distribution of current density in the anode spot of the argon arc. *Avtomaticheskaya Svarka*, **8**, 7 – 10.
10. Yeroshenko, L.E., Zamkov, V.N., Mechev, V.S. Prilutsky, V.P. (1980) Investigation of spectrum of the arc plasma in TIG welding of titanium over the flux layer. Ibid, **9**, 22 – 25.
11. Yeroshenko, L.E., Zamkov, V.N., Mechev, V.S., Prilutsky, V.P. (1979) Investigation of luminescence of the anode vapours for evaluation of welding characteristics of the arc in argon. Ibid, **9**, 33 – 35.
12. Yeroshenko, L.E., Prilutsky, V.P., Zamkov, V.N. (1997) Investigation of luminescence of the anode vapours in TIG welding of titanium over the flux layer. Ibid, **11**, 11 – 13.
13. Yeroshenko, L.E., Prilutsky, V.P., Zamkov, V.N. (1994) Investigation of processes occurring in the arc in TIG welding of titanium. Ibid, **4**, 3 – 5.
14. Pismenny, V.D., Rakhimov, A.T. (1971) Contraction of the positive column with electrically negative impurities. *DAN SSSR*, vol. 200, **1**, 68 – 71.
15. Yeletsky, A.V., Palkina, L.A., Smirnov, B.M. (1975) *Transfer phenomena in the slightly ionized plasma*. Moscow: Atomizdat.
16. Yeletsky, A.V., Rakhimov, A.T. (1977) Instabilities in the gas discharge plasma. In: *Chemistry of Plasma*. Vol. 4, 123 – 167. Moscow: Atomizdat.
17. Rakhimov, A.T., Ulinich, F.R. (1969) Contraction of the cylindrical gas discharge. *DAN SSSR*, vol. 187, **1**, 72 – 74.
18. Smirnov, B.M. (1997) Contraction of the high-pressure positive arc column. In: *Teplofizika vys. temperatur*. Vol. 35, **1**, 14 – 18.
19. McDaniel, I. (1967) *Collision processes in ionized gases*. Transl. from English. Moscow: Mir.
20. Savitsky, M.M., Leskov, G.I. (1980) Mechanism of the effect of electrically negative elements on the penetrating power of the arc with a tungsten cathode. *Avtomaticheskaya Svarka*, **9**, 17 – 22.
21. Leskov, G.I. (1970) *Electric welding arc*. Moscow: Mashinostroyeniye.
22. Gurvich, L.V., Karachevtsev, G.V., Kondratiev, V.N. *et al.* (1974) *Energy of break of chemical bonds*. Ionization potentials and affinity for electrolysis. Manual. Edited by V.N. Kondratiev. Moscow: Nauka.
23. Granovsky, V.L. (1971) *Electric current in gas. Steady current*. Edited by L.A. Sen, V.E. Golant. Moscow: Nauka.
24. Smirnov, B.M. (1978) *Negative ions*. Moscow: Nauka.
25. Messi, G. (1979) *Negative ions*. Transl. from English. Moscow: Mir.
26. Rokhlin, G.N. (1991) *Discharge sources of light*. Moscow: Energoatomizdat.
27. Mechev, V.S., Yeroshenko, L.E. (1975) Axial distribution of temperature of the electric arc in argon. *Avtomaticheskaya Svarka*, **6**, pp. 14 – 17, 54.
28. Babichev, A.P., Babushkina, N.A., Bratkovsky, A.M. *et al.* (1991) *Physical values*. Manual. Edited by I.S. Grigoriev, E.Z. Meilikhov. Moscow: Energoatomizdat.

PRODUCTION AND WELDING OF HIGH-TEMPERATURE COMPOSITE MATERIALS (Review)

V.R. RYABOV
The E.O. Paton Electric Welding Institute, NASU, Kyiv, Ukraine

ABSTRACT

Peculiarities of composite materials (CM) on base of nickel, chromium and cobalt alloys, designed for operation at elevated temperatures, are considered. The methods of CM producing are described and different examples of manufacture of weldments are given.

Key words: composite material, high-temperature resistance, fibres, nickel, chromium, cobalt, diffusion bonding, spot, arc welding.

Investigation and application of high-temperature composite materials (CM) have been continuously expanding over the last years. One of the promising directions in this field is development of high-temperature CM on the base of nickel, chromium and cobalt alloys reinforced with refractory metal fibres. For instance, in gas turbine construction the most urgent task is that of increasing the temperature of the thermodynamic cycle of the power units, as the effectiveness of gas turbine engines (GTE) rises with the increase of the working temperature of the gas [1].

Even a small increase in the temperature of the gas going into the turbine, significantly increases the efficiency of the gas turbine engine. The absence, however, of high-temperature materials capable of standing the temperature of 1473 to 1573 K for a long time, makes it necessary to apply in GTE various methods of cooling the structures from the currently used nickel and cobalt alloys. In this case, the geometry of the blades and vanes becomes more complicated, the dimensions and power of the engine compressor become greater. The operation of a gas turbine without cooling or, at least, with cooling not requiring much more complicated GTE designs, can be achieved by using special high-temperature CM. The nickel and chromium based CM reinforced with filamentary crystals of Al_2O_3 can be used as such materials, as well as compositions in which the matrix is made of the high-temperature alloys, and the reinforcement is from high-temperature refractory fibres. Quite effective for high-temperature parts of GTE is the use of nickel- and cobalt-base eutectic CM. The following of them have been tested with the best results: (Co–Ni–Cr)–TaC; (Ni–Cr–Al)–Ni_3Nb; (Ni–Co–Cr–Al)–TaC [2].

Assessment of CM application in aircraft engineering in the case of their use in the design of Il-62 plane shows that the weight of this air liner can be reduced by 17 % with the same flight characteristics, or the flight range can be increased by 15 % with the same take-off mass [3].

Fibrous frames from nickel and cobalt alloys and stainless steels have a higher damping capacity and are used as gaskets in mounting turbines and instruments. Such frames impregnated by quickly evaporating liquids, are applied in the cooling systems of MHD generators. Let us consider the limited available information on the methods of production and welding of fibrous (FCM) and dispersion-strengthened (DSCM) composite materials with nickel, chromium and cobalt matrices.

Fibrous CM with nickel matrix

The following reinforcers are used for reinforcement of nickel and its alloys: filamentary crystals (FC), refractory metal wires, ceramic and carbon fibres.

Nickel-base CM reinforced with tungsten and molybdenum fibres, are produced by dynamic hot pressing, diffusion bonding, explosion welding and rolling. These compacting methods are the most effective for sandwich type blanks consisting of alternating matrix sheets and layers of reinforcing fibres. In connection with the fact that tungsten and molybdenum intensively oxidise in heating, CM are produced under vacuum or in a shielding atmosphere in diffusion welding machines, vacuum rolling mills or using vacuumized containers [4].

CM with a matrix from high-temperature alloy KhN70Yu (El 652) and a number of other alloys reinforced with fibres of tungsten and TsM2A molybdenum alloy (0.1%Mo; 0.1%Ti–Zr) have been studied [5]. The materials were produced in the form of rods by the method of filling the mould with the reinforcement which was 2 to 4 mm diameter wire with the matrix melt (Figure 1) with subsequent deformation of the cast blank.

Investigation of the mechanical properties of extruded rods from CM showed that up to 1073 K, reinforcement only slightly affects the yield point of nickel alloys and somewhat lowers the ultimate strength, especially, if the materials are reinforced with tungsten fibres (Figure 2). Above 1073 K reinforcement essentially increases the alloys strength, and at 1373 to 1473 K the materials with about 25 vol. % of fibres, are several times stronger than the alloys without reinforcement. The ductility of the reinforced alloys decreases with the increase of the test temperature and of the volume fraction of fibres, but remains on a sufficiently high level (Figure 2).

Decrease of the low-temperature strength of nickel alloys as a result of reinforcement by tungsten fibres, is related to tungsten embrittlement when embedded into the matrix, which was confirmed by bend tests of fibres etched out of the matrix. Figure 3 shows the change of the mechanical properties of KhN70Yu alloy at 1373 K,

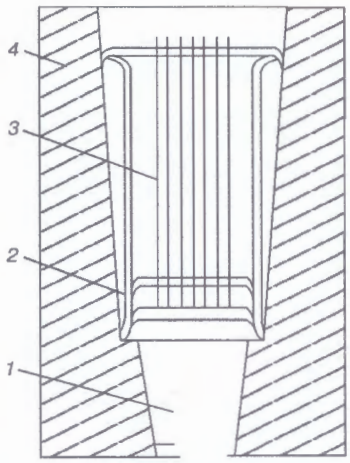

Figure 1. Schematics of production of a cast reinforced billet: *1* — plug for pushing the ingot out; *2* — cassette; *3* — bundle of reinforcing fibres; *4* — mould.

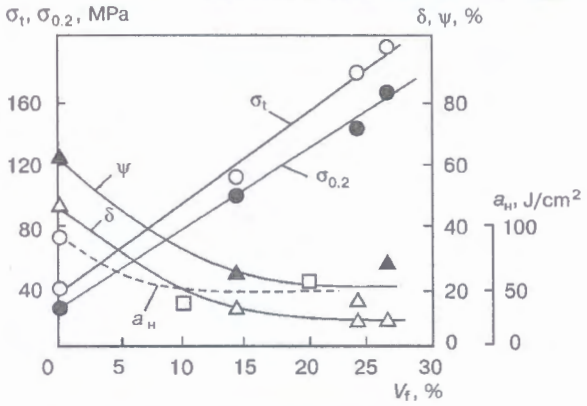

Figure 3. Variation of mechanical properties of KhN70Yu alloy at 1373 K, depending on the volume fraction of tungsten fibres.

depending on the volume fraction of tungsten fibres V_f. With the increase of V_f, the strength properties (σ_t, $\sigma_{0.2}$) increase by a linear dependence which corresponds to the rule of mixtures, and the ductility characteristics (σ, ψ) and impact toughness *KCU* (determined on round samples of 9 mm diameter with a notch of 1 mm radius and 1 mm depth) decrease.

The results of long-term strength tests (Figure 4) showed a considerable increase of high-temperature strength of nickel alloys when reinforced with tungsten fibres. The strength of KhN70Yu + 20 vol. % W material during 100 h at 1173 – 1473 K is more than 10 times higher than the appropriate values for a non-reinforced alloy. Reinforcement of KhN70Yu alloy with the fibres of TsM2A molybdenum alloy, increased the long-term strength at 1173 K. However, with the increase of the test temperature. the relative strengthening as a result of reinforcement decreases continuously, so that at 1372 K the long-term strength of KhN70Yu + 19 % TsM2A material exceeds the strength of the non-reinforced alloy only by 20 to 40 %, and by 10 to 15 % at 1473 K.

Comparison of σ_{100} values derived at different temperatures with σ_t values points to a more intensive softening of the materials reinforced with TsM2A fibres with the increase of the temperature and duration of testing.

In KhN70Yu + TsM2A materials at long-time high-temperature soaking essential changes in the structure and composition of the transition zone on the fibre-matrix interface occur besides the recrystallization of fibres. These changes are characterised by the formation of a continuous zone of a brittle intermetallic phase (hardness of about *HV* 750) and a noticeable decrease in the fibre cross- sectional area (Figure 5).

With longer soaking at higher temperatures, chromium concentration in TsM2A fibres essentially increases, while nickel diffusion into the fibres is quite insignificant.

In KhN70Yu + W materials, the diffusion interaction of the components is much weaker, than in KhN70Yu + + Mo system. No formation of the intermetallic phase on the interface was found in KhN70Yu + W system. After long-time soaking, however, a zone of diffusion porosity (Figure 5, *b*) associated with Kirkendale effect, is found around the fibres. The absence of porosity in Kh70Yu + + TsM2A materials is attributable to the presence of second phase precipitates in the matrix, which are the drains for the vacancies forming the pores.

The given data are indicative of a higher thermal stability of tungsten fibres in nickel-chromium matrix and

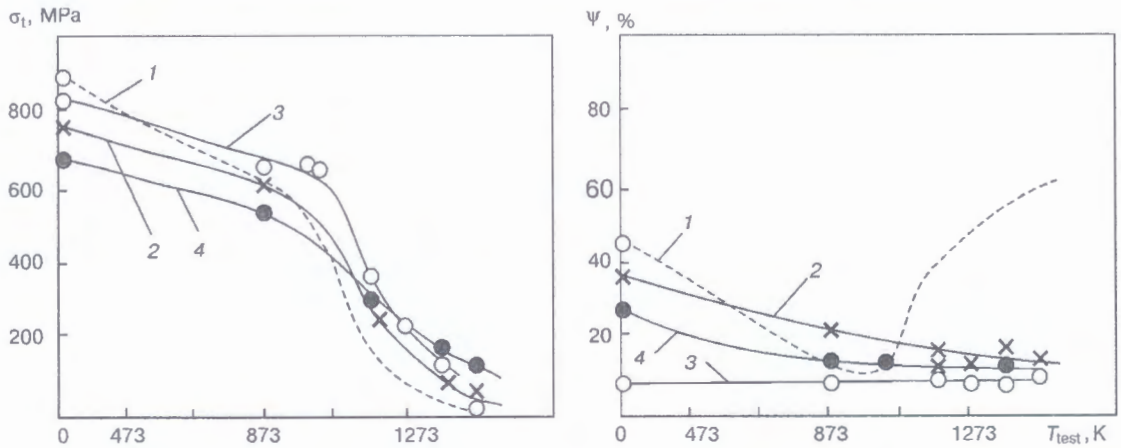

Figure 2. Temperature dependencies of ultimate tensile strength and reduction in area of KhN70Yu alloy: *1* — non-reinforced; *2* — with addition of 1.5 % TsM2A; *3* — with 26 % TsM2A; *4* — with 24 %W (by volume).

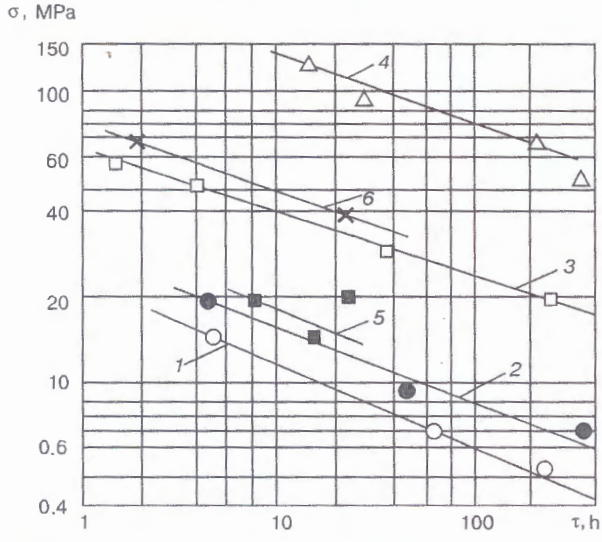

Figure 4. Long-term strength of composite materials at 1373 K: *1* — non-reinforced KhN70Yu alloy; *2* — KhN70Yu + 19 % TsM2A; *3* — KhN70Yu + 14 % W; *4* — KhN70Yu + 26 % W; *5* — KhN67MVTYu + 19 % TsM2A; *6* — KhN67MVTYu + 12 % W (by volume).

the need to use barrier coatings for the molybdenum alloy fibres. The physico-chemical interaction of the tungsten fibres with the matrix can be still further reduced by selection of the optimal composition of the matrix.

FCM heating in air results in oxidation of tungsten or molybdenum fibres located on the surface. If the fibres do not come to the surface, FCM high-temperature resistance is determined by the matrix high-temperature resistance.

In Ni–Al_2O_3 system, heating in air leads to formation of nickel oxide which interacts with the reinforcement, thus resulting in the formation of $NiAl_2O_4$ spinel on the fibre-matrix interface. In this case, the bond between the components is disturbed. In order to increase the adhesion strength, thin coatings of metals (tungsten, nickel, chromium) and ceramics (yttrium and thorium oxides) are deposited on the reinforcement. Since liquid nickel does not wet Al_2O_3, titanium, zirconium and chromium which improve the impregnation conditions, are added to the matrix.

Room temperature strength of FCM (nickel — filamentary crystals of Al_2O_3) produced by electroplating of nickel on the fibres, is essentially higher than the matrix strength (Table 1). At high temperature, a great scatter of the strength properties is found, because of an unsatisfac-

Table 1. Mechanical properties of nickel-base FCM reinforced with Al_2O_3 FC

V_f, %	σ_t, MPa		$\sigma_{t.el.}$, J g	
	at T_{test}, K			
	293	1273	293	1273
16	–	282	–	114
21	–	495	–	67
22	1230	–	163	–
29	–	759	–	108
39	1350	–	20	–
51	1050	–	168	–

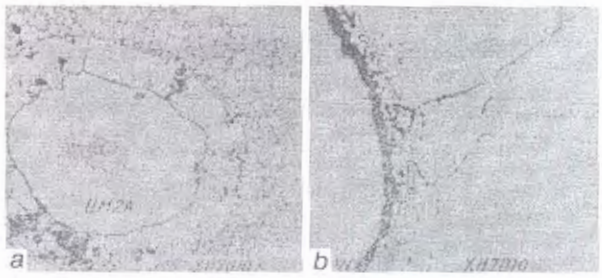

Figure 5. Microstructure of reinforced rods after annealing at 1273 K for 1000 h: *a* — (×100); *b* — (×300) (reduced by 0.52).

tory adhesion of the components. The softening factors are fragmentation of the fibres or coarsening of their structure, as well as a non-uniform reinforcement of the samples through their volume, which is due to the difficulty of arranging the fibres.

Nickel is practically insoluble in carbon. The volume fraction of carbon dissolved in molten nickel (T = = 1823 K), is equal to 12.5 %, and to 2.8 % in solid nickel. Moreover, Ni–C system forms a metastable Ni_3C carbide, stable at the temperatures above 1673 K and below 723 K. Having a high diffusion mobility, carbon saturates the nickel matrix in a short time. Therefore, the main softening factors in Ni–C FCM are dissolution of carbon fibres and their recrystallization as a result of nickel penetration into the fibre. Addition of carbide-forming elements to the nickel matrix, which are the usual components of nickel alloys (Cr, Al, Ti, Mo, W, Nb), enhances the matrix interaction with carbon fibres [6].

In order to increase the structural stability of Ni–C FCM, anti-diffusion barrier coatings from zirconium carbide and nitride, titanium carbide (for working temperatures up to 1273 K) are applied onto the carbon fibres.

The strength of nickel CM with Tornel-50 and Tornel-75 carbon fibres (V_f = 50 %) is equal to 800 and 830 MPa, and their modulus of elasticity to 240 and 310 GPa, respectively.

Powder metallurgy methods are used to produce FCM based on NASA type alloys [6]. The tungsten reinforcement is impregnated with slurry from fine powder of the matrix. Sintering is performed in hydrogen at 1088 K temperature for 1 h.

The final operation is isostatic hot pressing at the temperature of 1088 to 1363 K, pressure of 138 MPa and soaking time of 1 h.

The strength of nickel-base FCM is much higher than the matrix strength. The highest strength is found in FCM produced by the methods of plastic working and powder metallurgy.

Under the simultaneous impact of high temperatures and stresses, the fibre strength is lowered as a result of softening diffusion and recrystallization. Reinforcement with molybdenum does not allow development of the materials and structures stable at high temperatures. The highest values of long-term and specific long-term strength were derived for FCM with a matrix from NASA-3 alloy reinforced with wire of W–Hf–C alloy with 70 % volume fraction.

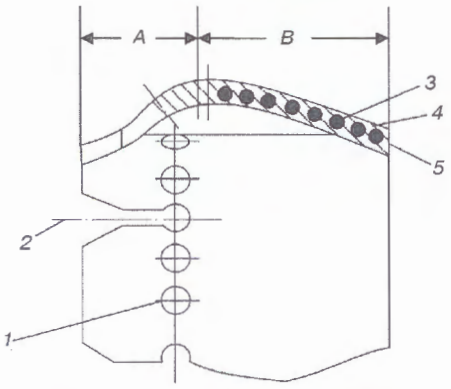

Figure 6. Longitudinal section of a reinforced shell of the combustion chamber flame tube (for designations see the text).

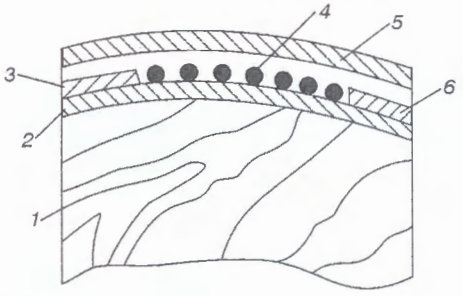

Figure 7. Schematics of a pack assembly prior to welding of the reinforced shell (for designations see the text).

Let us consider a practical example of application of nickel-base FCM.

Flame tubes of GTE combustion chambers operate under the conditions of intensive oxidation by the high-temperature gas flow and relatively low loads. Therefore, they are produced from low- strength KhN78T (EI 435), VZh 98, VZh 107 and other alloys highly resistant to scaling. However, the walls of the flame tubes of combustion chambers sometimes fail as a result of a non-uniform heating even with the steady-state mode of the engine operation. Besides variation of the flame temperature in the radial direction, the continuous non-uniform heating results from the presence of holes for supply of secondary air. In this case, the shell temperature varies in the axial direction of the combustion chamber so that the central part the farthest from the holes, is always overheated. Such non-uniform heating and local overheating of the flame tube shells leads to distortion and local buckling which causes burns-through and failure of the material. This is especially manifest when the combustion chamber walls are exposed to high (1273 – 1423 K) temperature in service. In this connection, as well as in view of the tendency for increasing the GTE working temperatures, improvement of the strength properties of the materials for the flame tubes, is an urgent task. However, increasing the high-temperature strength of alloys highly resistant to scaling by the traditional methods, leads to reduction of their resistance to scaling.

Technology [7, 8] of making flame tube shells was developed in which production of sheet CM and of the shell profile is combined. In this case, only the part of the shell exposed to maximal temperature in service, was subjected to reinforcement with VT10 tungsten wire of 0.4 mm diameter. The longitudinal section (sketch) of the shell is shown in Figure 6. It consists of zigzag part *A* with holes *1*, slots *2* and smooth spherical part *B* which is reinforced with tungsten wire *3* wound continuously in one layer located within the section of the smooth part of the ring with protective layers *4* of an alloy resistant to scaling from the surface and end face *5*.

In order to produce this shell, prefabricated spherical ring 2 of EI 435 alloy was put on the spherical detachable wooden mandrel *1* (Figure 7) and strips *3* and *5* from the same alloy were placed on the ring in the areas which were not to be reinforced, and fastened by resistance spot welding. Tungsten wire *4* was wound between strips *3* and *5* with a uniform pitch, which was achieved by prior winding of 0.1 mm nichrome wire on the tungsten wire. The wound nichrome wire prevented contact of the adjacent tungsten wires when they were closely wound and provided for their spacing of 0.15 mm on average. Winding of nichrome wire was performed in a lathe using a special device.

During winding on the drum the tungsten wire was fastened in some points by capacitor-type spot welding to ring *2*, which was followed by putting on the outer spherical billet of ring *6* from KhN78T alloy, preformed by expansion. The thus assembled pack consisting of sheets of scale-resistant alloy and tungsten wire, was welded by roller-spot welding over the entire contact surface. The welding direction was around the circumference of the circular pack. The welds were concentric circles with the next weld overlapping the width of the previous one by 25 to 30 %. The width of welding rollers was 12 mm.

Filling of the space between the tungsten wires with the matrix metal and melting of nichrome wire, leads to considerable thinning of the reinforced sheet (down to 1 mm), compared to the pre-assembled unwelded pack of 1.4 mm thickness.

In order to relieve welding stresses, the produced shell was annealed at the temperature of 1373 K for 2 h, was calibrated in the expanding machine in a profiled mandrel, the zigzag-shaped part of the ring was rolled out and the edges were cut to the required dimensions. Further machining of the ring and assembly of the component of the flame part of the chamber were performed by the regular technology.

The developed technology was used to produce the outer and inner shells of flame tubes of circular combustion chambers of engines.

The high thermal conductivity of the reinforced material lowers the probability of high local overheating, and its low coefficient of linear expansion, reduces the relative deformation of the more heated local zone (compared to the less heated ones) and thus also the thermal stresses

Full-scale rig testing of the outer and inner reinforced shells of the flame tube of the combustion chamber in AI-25 engine, was conducted for 435 h. The modes were selected to be equivalent to the life of 1500 h, thus corresponding to 1969 thermal cycles during launches and

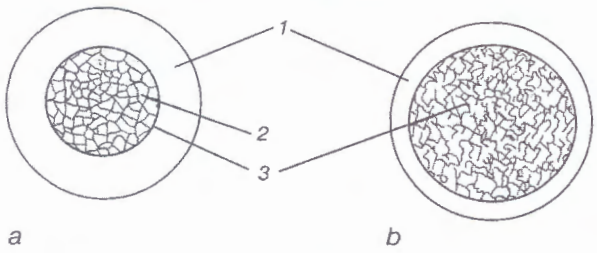

Figure 8. Schematics of structural changes in interaction of the tungsten fibre with nickel (*a*) and chromium (*b*) in the following zones: *1* — diffusion; *2* — nickel-initiated recrystallization; *3* — initial wrought structure of tungsten wire.

stops. No inner separation of the fibres from the matrix was found as a result of testing.

Use of such reinforced material allows development of combustion chambers with a higher thermal factor, thus permitting their dimensions and, consequently those of the entire engine, to be reduced.

Fibrous CM with a chromium matrix

When evaluating nickel-base FCM, it should be noted that ferro-aluminium high-resistance alloy and nickel-chromium-aluminium alloys with yttrium, reinforced by tungsten fibres from an alloy of W–Re–HfC system, whose high-temperature strength at 1360 K is three times higher than that of nickel superalloys, turned out to be the best materials in this group [1].

However, CM with an iron-, nickel-, cobalt-base matrix develop high thermal stresses as a result of a significant difference in the thermal expansion factors of these alloys and the tungsten fibre.

A different nature of structural changes is found in Cr–W system. The absence of intermetallics and a wide area of co-existence of the two solid solutions based on chromium and tungsten, up to the temperature of 1768 K, prevents an active interaction of the fibre and the matrix on whose interface a thin, thermally stable intermediate layer forms from the two solid solutions which are in equilibrium, Figure 8. In the initial state after CM fabrication, the width of the zone of interaction is 2 to 3 μm, and after 100 h testing at 200 MPa load at the temperature of 1373 and 1473 K it increases up to 10 and 20 to 25 μm (at maximum), respectively, whereas in Ni–W CM after heating at 1423 K for 1000 h, the width of the diffusion zone is 53 μm. Unlike Ni(Fe)–W CM, Cr–W CM has no zones of fibre recrystallization induced by the matrix material. In the range of 1473 to 1673 K, the tungsten fibre remains unrecrystallized in the chromium matrix.

The strength properties of Cr–W CM are determined by the tungsten fibre properties. Figure 9 gives the dependence of σ_t on Larson-Miller parameter $P = T(20 + \lg \tau)$ which can be used to calculate the material creep time up to its fracture.

The strongest are the alloys with hafnium carbides or nitrides, the alloys with HfC, however, differ by a greater stability of the high-temperature properties in contact with the chromium matrix, than the alloys with HfN. The content of HfC filler is limited both by the alloy adaptability to fabrication, and by the capability of equipment used for production of 0.3 mm diameter wire.

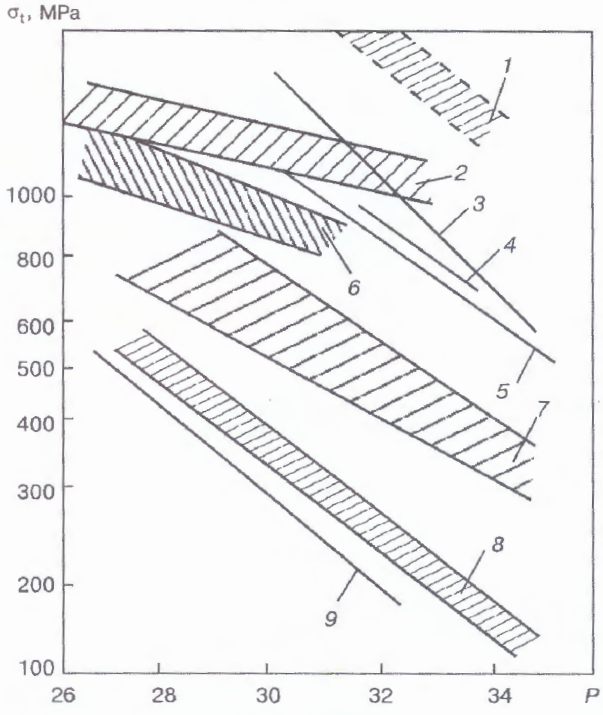

Figure 9. High-temperature strength of reinforcing fibres of tungsten alloys: *1* — W–Hf–N (0.3 mm dia.); *2* — VMRG (W–18Mo–27Re–HfC); *3* — W–Re–HfC; *4* — VMRK; *5* — W–HfC; *6* — W–HfC, HfO_2; *7* — VL; VT15; VT20; *8* — W–2ThO_2, VR27; *9* — TZm.

For fabrication of CM with a chromium matrix, wire from vacuum-melted VMRK alloy with the following properties was used:

$$\sigma_t^{1473} = 2150 \text{ MPa}; \sigma_{100}^{1473} = 750 - 800 \text{ MPa}.$$

The chromium matrix was 0.2 to 0.3 mm thick sheet from low-alloyed VKh2U alloy with the following properties:

$$\sigma_t^{293} = 370 - 510 \text{ MPa}; \delta^{293} = 21 - 35\ \%,$$
$$\sigma_t^{1473} = 35 \text{ MPa}, \delta^{1473} \geq 40\ \%.$$

The high ductile properties of the matrix allowed the method of diffusion bonding in a vacuum press and in the HIP machine at the temperatures of 1273 to 1473 K, to be used for production of sheet CM. The sheet blanks were assembled from several layers of monostrip with tungsten wire fibres fastened to the chromium substrate. Such a method allowed sheet blanks to be produced with a uniform distribution of the fibres with preservation of their integrity. In Cr–W CM the integrity of the fibres was not violated during the items fabrication due to the adequate ductility margin of both the matrix and the fibres. Models of a GTE vane with bending radius of the leading edge equal to 0.8 mm at 46° angle, were made from sheet blanks of this CM of 1.2 mm thickness (Figure 10).

With the volume fraction of fibres from VMRK alloy equal to 30 %, the CM density was approximately 10 g/cm^3, whereas the mechanical properties at the an-

Figure 10. Model of a GTE blade from chromium — tungsten fibre CM.

ticipated service temperature were up to $\sigma^{t}_{100} = 80 - 100$ MPa at 1573 K.

Complex-shaped items including doubly curved surfaces, cannot be formed from sheet blanks. The model of such an item (engine combustion chamber) was made from a bimetal wire, namely tungsten fibre of 0.35 mm diameter with a chromium coating of 0.17 mm thickness applied onto it by the method of gas-phase transport reactions. The wire was wound tightly (turn to turn) in several layers on a steel mandrel which had BKh2U alloy condensate deposited on it by ion-plasma method. After winding, the outer part of the steel capsule was put on the mandrel, the assembly was sealed and welding was performed in the HIP machine at the temperature of 1473 K. Figure 11 shows the appearance and microstructure of the item after removal of the mandrel. Its length was 80 mm with the diameter of 14 mm in the narrow and 40 mm in the expanded part, wall thickness being 1.8 mm. The flange is made from VKh2U alloy. The volume fraction of tungsten was about 25 %. The model of the combustion chamber was blown-through by a high-enthalpy plasma jet of air at the temperature of 2000 to 2800 K. The temperature of the chamber outer surface was up to 1900 K. The total duration of testing was 2490 s. The inner hotter surface did not undergo any visible changes. The temperature level of testing exceeded by almost 300 K the regular service temperature of such items from high-temperature nickel superalloys.

Plasma-arc welding process was used for fabrication of cobalt-base CM strengthened with boride particles [9]. Powders of molybdenum and MoB were mixed with a cobalt alloy (CoCrB-powder) which had 2.36 to 5% B, in order to improve the CM wear resistance. Investigations were performed on materials which had a cobalt matrix (B–Co), banded structure (Cr_7C_3, $Cr_{23}C_6$) and mostly crystals (CoMoB, $CoMo_2B_2$). The volume of boride fractions rose with the increase of boron additives amount.

Dispersion-strengthened CM

DSCM combine a matrix of pure metal or alloy and uniformly distributed in it with a predetermined spacing, finely-dispersed refractory particles of the strengthening phase of less than 0.1 μm size, artificially introduced into the material in one of the process stages [10]. The volume fraction of disperse inclusions in DSCM, is equal to 0.1 to 15 %. Disperse inclusions of oxides, carbides, nitrides, borides and other refractory compounds, as well as intermetallic compounds are used as the strengthening phase. The criterion for selection of the strengthening phases, is their thermodynamic stability in relation to the matrix metal.

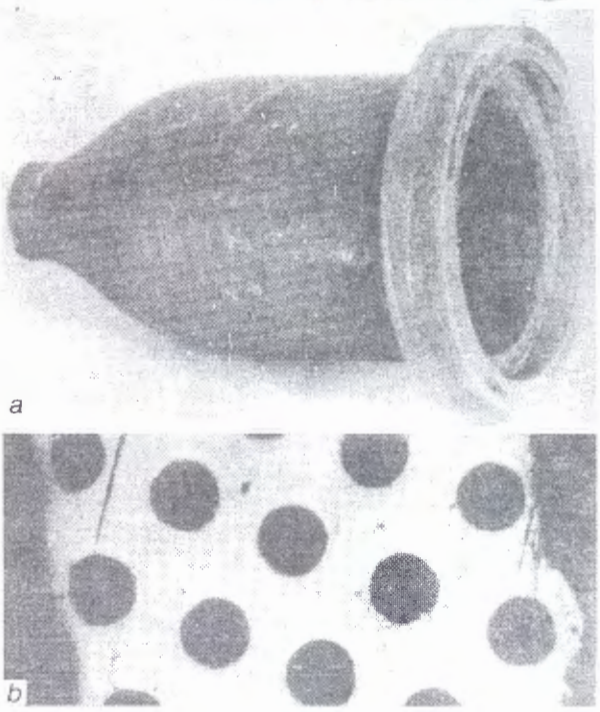

Figure 11. Model of a combustion chamber from chromium — tungsten fibre CM (*a*) and CM structure (*b*).

The process of production of semi-finished products of DSCM includes the following operations: preparation of the powder mixture, forming, sintering, plastic working and heat-treatment.

The aim of development of nickel DSCM, was an increase of high-temperature resistance and decrease of high-temperature creep of nickel and its alloys. Oxides [11] are used as the strengthening phase in nickel-base DSCM, as oxide stability in nickel at high temperatures is higher, than that of other refractory compounds. There is data on fabrication of DSCM with disperse TiC and TaC carbides.

Thorium oxide is the one the most widely used for nickel strengthening. The known VDU-1, TD-nickel and DS-nickel DSCM contain 2 % ThO_2. In addition to thorium oxide whose disadvantage is a higher toxicity, hafnium, yttrium, zirconium, aluminium oxides are also used. VDU-2 DSCM has 3 % HfO_2 in the nickel matrix. A higher strength level is achieved in DSCM on alloyed nickel base. Alloying with chromium is the most effective. VDU-3 (volume fraction of Ni — 76 %, Cr — 20 %, HfO_2 — 4 %), TD-nichrome (87 % Ni, 20 % Cr, 2 % ThO_2), DU-nichrome (78.2 % Ni, 20 % Cr, 1.8 % V_2O_3) DSCM have been developed. DSCM alloyed with molybdenum have the following composition, %: 81 Ni, 25 Mo, 4 ThO_2.

DSCM are produced by powder metallurgy methods. DSCM based on KhN56VMKYu complex alloy is produced by addition of strengthening disperse particles of

Table 2. Long-term strength of VDU-1 and VDU-2 DSCM

Kind of semi-finished product	T, K	σ_{10}, MPa		σ_{100}, MPa		σ_{1000}, MPa	
		VDU-1	VDU-2	VDU-1	VDU-2	VDU-1	VDU-2
Sheet	1173	–	–	115	95	105	85
	1273	–	78	95	75	85	65
	1373	78	62	75	55	65	45
	1473	67	42	50	35	40	25
Rod	1173	–	–	150	105	140	95
	1273	–	95	125	90	120	80
	1373	108	75	105	70	100	65
	1473	88	60	75	55	65	40

ZrO_2 (2 % volume fraction) during vacuum-arc remelting with the application of ultrasound.

Semi-finished products from DSCM are supplied in the form of rods, pipes, wire, sheets, strips and foil.

DSCM with an unalloyed matrix have close values of yield point and ultimate strength. In the cold-worked condition the room temperature ultimate strength is up to 800 to 900 MPa, in the asannealed state 450 to 600 MPa. The strength decreases monotonically with the increase of temperature, and is equal to 100 to 120 MPa at the temperature of 1373 K. The elasticity modulus at room temperature is equal to 145 to 155 GPa, and to 750 to 850 GPa at 1373 K. The impact toughness in the temperature range of 293 to 1473 K is preserved at the level of (150 to 180) × $\times 10^4$ J/m^2.

DSCM with an unalloyed matrix have a high long-term strength at the temperatures of 1173 to 1473 K (Table 2), their strength at the room and moderate temperatures and high-temperature strength being, however, not high enough. These properties are essentially improved by alloying the nickel matrix with chromium (Table 3).

In DSCM with a nickel-chromium matrix containing aluminium and in the case of complex-alloyed matrices, strengthening by disperse particles is combined with strengthening by intermetallic phases which precipitate from the solid solution in ageing. The level of their mechanical properties is very high.

In high temperature tests under the creep conditions, nickel-base DSCM are characterised by a low rate of softening in time and insignificant increase in softening intensity with the rise of temperature. Alloys with a nickel-molybdenum matrix have a high creep resistance. Nickel-base DSCM are superior to the commercial ageing nickel alloys in long-term strength and fatigue properties at the temperatures above 1273 K. The fatigue limit of TD-nickel sheets at 1373 and 1473 K is 80 and 40 MPa, respectively.

The physical properties of DSCM, in view of the small content of the strengthening phase and its inertia in relation to the matrix, are close to the properties of the matrix metals and alloys.

In the temperature range of 293 to 1573 K, the specific heat of DSCM with an unalloyed matrix is 580 to 650 J/(kg×K), the temperature coefficient of linear expansion is (14 – 18) × 10^{-6}, K^{-1}, the heat conductivity factor is 56 to 77 W/(m×K), the specific electrical resistance being (8 – 63) × 10^{-8} Ohm×m. The values of DSCM heat conductivity are higher than those of the commercial high-temperature nickel-base alloys.

Table 3. Mechanical properties of VDU-3 (sheets, 1 mm)

T, K	σ_t, MPa	δ, %	σ_{100}, MPa
293	750 – 850	8.0 – 12.0	–
873	400 – 450	5.0 – 7.0	–
1273	130 – 140	2.0 – 2.5	50
1373	90 – 100	2.0 – 2.5	35
1473	75 – 80	1.5 – 2.5	20

Nickel-base DSCM have a higher high-temperature resistance than the matrix material. Further increase in the high-temperature resistance can be achieved by applying chromium-aluminium protective coatings. DSCM are not prone to intercrystalline corrosion, the oxide film strongly adheres to the base metal. The thickness of the layer of TD-nichrome sheets affected by oxidation at the temperature of 1273 K in air, is characterised by the following values:

oxidation duration, h	1000	5000	10000	50000
thickness of oxidised layer, μm	2.5	20	60	100

High-temperature resistance is increased with addition of 2 to 5 % aluminium to the nichrome matrix.

DSCM with a pure nickel matrix have high adaptability to fabrication and excellent workability. The adaptability to fabrication of TD-nichrome is satisfactory. Making DSCM matrix composition more complicated, lowers their adaptability to fabrication.

Nickel-base DSCM are used in fabrication of engine parts exposed to the temperatures of up to 1573 K and low stresses. Such service conditions are characteristic for parts of the nozzle, combustion chambers and afterburners of aircraft engines. Making flame stabilisers of the afterburner from TD-nichrome, solves the problem of high-temperature cracking.

Joining parts from DSCM presents certain difficulties. The point is that in fusion welding, pores develop and agglomeration of strengthening particles takes place in the metal melting zone. Increase of the welding speed and reduction of the amount of metal being melted, allow a sound weld to be produced, but redistribution and agglomeration of the strengthening particles cannot be avoided completely. This results in the central zone of the weld being made up by the matrix metal practically free from the strengthening phase, whereas the peripheral zone contains a large number of coarser oxide particles and is more brittle.

The consequences of the strengthening particles agglomeration are manifested to a smaller degree in welding of materials with a complex-alloyed matrix. By the data of authors of Reference [11], tungsten-electrode arc welding, flash butt and resistance spot welding of IN-853 alloy, provided the joint strength of up to 90 % of the base metal strength at 1033 and 1313 K; the long-term strength of welded joints at these temperatures was high. The situation is similar also when filler materials are used in welding of TD-nickel, namely the high-temperature creep re-

sistance of the welds is determined by the appropriate properties of filler materials.

Joining of DSCM sheets is performed by the methods of diffusion bonding and brazing. Application of the regular methods of fusion welding is limited. Electric arc welding can be used for DSCM exposed to temperatures below 1373 K in service.

Solid-phase processes, for instance, diffusion bonding and brazing should be of great interest for joining parts from DSCM [12].

Moore and Holko [13] studied the process of diffusion bonding of rods of TD-nickel with a fine- grained structure. Butt and overlap joints were made by hot isostatic pressing under vacuum with soaking for 2 h at 1363 K under the pressure of 140 MPa. Despite such a stringent temperature- force mode of bonding, the joint strength at 1363 K was not higher than half of the base metal strength. Better results were derived in diffusion bonding under the same conditions using backing from various metals and alloys. In this case, however, the high-temperature creep resistance still remained low. So, use of gaskets of 0.1 to 0.3 mm thickness from cobalt alloy Co + 2.8 % Cr + + 25 % W + 0.9 % Ti + 0.4 % Zr + 2 % Re + 0.15 % C provided the strength of butt and overlap joints equal to 100 % and 91 to 97 % of the base metal strength, respectively, both at room temperature and at 1363 K. On the other hand, the 100 h ultimate strength at 1363 K was not higher than 15 % of the initial values of strength for the rods, this being attributable to high-temperature corrosion in the welding zone.

In particular, the complexity of making sound joints in diffusion bonding without fillers, is related to lower ductility of the dispersion-strengthened materials at high temperatures. In order to ensure a better contact of TD-nichrome alloy samples being welded, it was proposed to perform diffusion bonding of the sheets not subjected to recrystallization annealing and having an essentially higher ductility at 573 K than the recrystallized sheets.

Shear and creep testing at 1363 K of overlap joints produced by the above method, showed them to be equivalent to the base metal in strength.

The process of diffusion bonding of non-recrystallized sheets of TD-nichrome alloy was improved later on [14]. It was possible to intensify diffusion bonding by replacing the two-step mode by the single-step mode which included soaking at 140 MPa pressure for 1 h at 1033 K with subsequent annealing for 2 h at 1453 K. A similar mode differing only by a higher pressure (270 MPa) is recommended for welding recrystallized sheets. However, the joints in this case have a somewhat lower strength and are not as stable as in welding of non-recrystallized sheets. It should be noted that annealing after welding is an important operation.

For non-recrystallized sheets such annealing leads to complete disappearance of the joint boundary as a result of grain coarsening, and in recrystallized sheets the weld strength increases after annealing due to intensive diffusion.

Use of non-recrystallized material offers certain advantages also in spot welding [15]. On the other hand, high strength of the joints is achieved also in the commercial recrystallized material, especially when soft welding modes with minimal surface melting are used. For TD-nichrome sheets, the shear strength of spot welded joints, including their long-term strength at 1373 K, is not inferior to the base metal strength. Satisfactory results were also derived in fatigue tests at room temperature and asymmetrical tension with 0.2 cycle asymmetry factor, namely the breaking shear stress with 106 cycles, was not less than 25 MPa. Spot welding of dispersion-strengthened nickel materials has currently become accepted in industry.

REFERENCES

1. Bannykh, O. A., Povarova, K.V., Kutienkov, V.A. *et al.* (1991) High-temperature composite material with metal matrix. In: *Composite materials. Collection of scientific. papers*, 63 – 67. Kiev: E.O. Paton Electric Welding Institute.
2. Karpinos, D.M., Tuchinskii, L.I., Sapozhnikov, A.B. *et al.* (1985) *Composite materials in engineering*. Kiev: Tekhnika.
3. Pilipovskii, Yu.L., Grudina, T.V., Sapozhnikov A.B. *et al.* (1990) Ibid. Kiev: Tekhnika.
4. Portnoi, K.I., Babich, B.N., Svetlov, I.L. (1979) *Nickel-base composite materials*. Moscow: Metallurgia.
5. Nishida, M., Minakuchi, K., Ando, K. (1995) Fabrication of high-strength steel fibre reinforced metal matrix composites by explosive bonding and their tensile properties. *Welding International*, vol. 9, **3**, 179 – 184.
6. Potapov, I.N., Lebedev, V.N., Kobelev, A.G. *et al.* (1986) *Laminated metallic compositions*. Moscow: Metallurgia.
7. Omel'chenko, V.I., Natapov, B.S., Banas, F.P. *et al.* (1972) Technology of production and properties of high-temperature resistant reinforced sheet. *Aviats. Prom.*, **1**, 56 – 58.
8. Kladnitskii, E.I., Botvinov, V.E., Banas, F.P. *et al.* (1977) Reinforcement of shells of flame tubes of GTE combustion chambers. Ibid, **9**, 26 – 29.
9. Shigekawa, Yu., Nojiri, Ya., Nishida, M. *et al.* (1977) Ehime daigaku kogakubu kiyo. *Mem. Fac. Eng. Ehime Univ.*, **16**, 463 – 471.
10. Kivineva, E.I., Olsom, D.I., Matlock, D.K. (1995) Particulate reinforced metal matrix composite as a weld deposit. *Welding J.*, **3**, 83 – 92.
11. Portnoi, K.I., Babich, B.I. (1974) *Dispersion-strengthened materials*. Moscow: Metallurgia.
12. Kenyon, N., Hrubec, R.J. (1974) Brazing of a dispersion strengthened nickel base alloy made by mechanical alloying. *Welding J.*, vol. 53, **4**, 145 – 152.
13. Moore, T.J., Holko, K.H. (1970) Solid-state welding of TD-nickel bar. Ibid, vol. 49, **9**, 395 – 409.
14. Holko, K.H. (1973) An improved diffusion welding technique for TD–Ni–Cr sheet. Ibid, vol. 52, **11**, 515 – 523.
15. Moore, T.J. (1974) Solid state and fusion resistance spot welding of TD–Ni–Cr sheet. Ibid, vol. 53, **1**, 37 – 48.

PREHEATING AND POSTWELD HEATING IN WELDING HIGH-STRENGTH ALLOYED STEELS

L.I. MIKHODUJ and **S.B. KASATKIN**
The E.O. Paton Electric Welding Institute, NASU, Kyiv, Ukraine

ABSTRACT

The investigation showed that in welding of microalloyed steels it is necessary to limit the preheating temperature $T_{max} \approx 80 - 130$ °C and, when possible, to decrease the duration of effect of this temperature on welded joints. The postweld heating can be eliminated from the technological process.

Key words: high-strength steels, carbonitride strengthening, preheating and postweld heating, ageing, X-ray analysis, delayed fracture.

The preheating is widely used in domestic and foreign practice to increase the resistance of high-strength steel welded joints to cold cracking. Depending on the chemical composition of steels, their thickness, type of welded joints and conditions of manufacture of structures the preheating can occur within the wide range of temperatures: from 50 up to 250 °C [1,2]. With decrease in cooling rate within the region of temperatures of a martensitic transformation, the preheating T_{pr} contributes effectively to the reduction of diffusive hydrogen content in weld metal and heat-affected zone (HAZ). In welding alloyed steels the postweld heating T_{pw} or «rest» can also be used. The latter terminology was suggested in work [3] as applied to welding of heat-resistant steels. The recommended «rest» temperature is 100 – 200 °C and the duration of this operation may reach 10 h. The postweld heating within this interval of temperatures is also recommended in work [4] for general-purpose high-strength steels. Thus, taking into account the total time which is consumed for preheating, welding and postweld heating, the welded joints of high-strength steels are subjected to 200 – 250 °C temperature for a long time. This contributes to ageing of separate structural zones and welded joints as a whole. This process is especially active at content of a dissolved nitrogen above 0.003 % in metal and intensive cooling below the temperature A_{c1}. This can be associated with a precipitation of tetragonal nitrides of iron α–$Fe_{16}N_2$. From the observations of authors [5, 6] the ageing of these steels is also possible at a long heating at temperature 130 – 150 °C.

It is known that a large group of domestic high-strength steels with 600 – 800 MPa yield strength (14KhG2SAFD, 12GN2MFAYu, 14KhGN2MDAFB, 12GN3MFAYuDR, etc) contains 0.02 – 0.03 % of nitrogen, and also a considerable amount of carbide- and nitride-forming elements (aluminium, vanadium, niobium, etc.). As a rule, their total content in the mentioned steels is Σ Al, V, Nb = 0.01 – 0.04 %. Thus, the process of manufacture of welded structures from high-strength steels with a carbonitride strengthening contributes to proceeding of processes of HAZ metal ageing and, as a consequence, to the reduction not only in impact strength, but also in resistance of welded joints to a delayed fracture.

In this connection, an integrated investigation of effect of conditions of preheating and postweld heating on changing the structure, toughness and resistance to a delayed fracture of the mentioned grades of steels with a total content of carbide- and nitride-forming elements of 0.09, 0.18 and 0.27 %, respectively, and $\delta_{0.2} = 600 - 800$ MPa was carried out. Butt joints of these steels with X-shaped edge preparation and 12 mm thickness were welded with 1.2 mm diameter wire Sv08KhN2GMYu in mixture Ar + CO_2 at $Q_w = 14$ kJ/cm. Depending on test conditions the preheating of joints at temperature 20 – 250 °C and also the preheating in combination with a postweld heating were made (Table). Selection of temperatures T_{pr} and T_{pw} and their duration were specified both by known technological recommendations and also by an experience of manufacture of welded structures from high-strength steels under the shop conditions.

Sections for metallographic examination, as well as the specimens for impact tests and also the laboratory technological samples (LTS3) of 2×12×100 mm were manufactured from welded joints of these steels to evaluate the metal resistance to a delayed fracture [7]. Notches in specimens (Figure 1) were made to evaluate the effect of different conditions of preheating high-strength alloyed steels on the HAZ metal resistance to the action of impact loads, and also to the delayed fracture.

Metallographic examinations showed that HAZ of all the specimens is characterized by a dispersed bainitic structure (mixture of upper and lower bainite), and also acicular martensitic-bainitic structure, which are typical of these steels. The comparison of microstructures results in definite conclusions that HAZ of specimens in welding at fusion temperature ($T_{pr} \leq 130$ °C) and minimum time of staying at this temperature $\tau \leq 1.5$ h (see Table, specimens No. 4, 11 and 18) is optimum from the point of view of morphology and dispersity. Combination of preheating and postweld heating of welded joints of all steels led to changing the morphology of the initial martensitic-bainitic structure, namely: at fusion temperature ($T_f = 130$ °C) it lost mainly an acicular origin, and increase in T_f up to 250 °C and time of soaking at this temperature from 2 to

Effect of conditions of preheating and postweld heating on impact strength of HAZ metal of high-strength alloyed steels

Steel grade	Σ Al + V, Nb, %	№ of specimen	Preheating		Postweld heating		KCU_{+20}, kJ/cm²
			T_{pr}, °C	τ, h	T_{pw}, °C	τ, h	
13KhGMRB	0.09	1	20	–	–	–	232.0
		2	20	–	130	2.0	230.0
		3	20	–	130	16.0	218.4
		4	130	1.5	–	–	224.0
		5	130	1.5	130	2.0	218.0
		6	130	1.5	130	4.0	225.0
		7	250	1.0	–	–	228.0
		8	250	1.0	250	4.0	228.0
		9	250	1.0	250	16.0	220.0
12GN2MFAYu	0.18	10	20	–	–	–	108.4
		11	130	1.5	–	–	116.2
		12	130	1.5	130	2.0	118.4
		13	130	1.5	130	4.0	113.5
		14	250	1.0	–	–	112.3
		15	250	1.0	250	2.0	115.0
		16	250	1.0	250	4.0	109.9
14KhGN2MDAFB	0.27	17	20	–	–	–	185.0
		18	80	1.5	–	–	176.4
		19	130	1.5	–	–	180.0
		20	130	1.5	130	2.0	186.0
		21	130	1.5	130	4.0	186.0
		22	250	1.0	–	–	197.0
		23	250	1.0	250	2.0	209.0
		24	250	1.0	250	4.0	202.0

4 h promoted the complete loss of an acicular structure. The results obtained can make an assumption about a precipitation of the second carbonitride phase, i.e. about the proceeding of the ageing process. Due to a fine dispersity of the phase, as well as fine acicularity of the martensitic-bainitic microstructure of the welded joints the metallographic examinations do not lead to a single result and cannot characterize the process.

To check this assumption the X-ray analysis of samples from 12GN3MFAYuDR was made in DRON-2.0 unit at $U = 30$ kV and $I = 20$ mA using a cobalt radiation.

Starting from specimen No. 5 (see Table) a precipitation of the second phase is observed in HAZ of this steel, thus proving the presence of peaks in roentgenograms, shown in Figure 2 (see arrows). The X-ray analysis has established that the fine-dispersed second phase is a mixture of nitrides and carbonitrides of vanadium. Such changes in structure did not almost influence the toughness of HAZ metal in all examined steels.

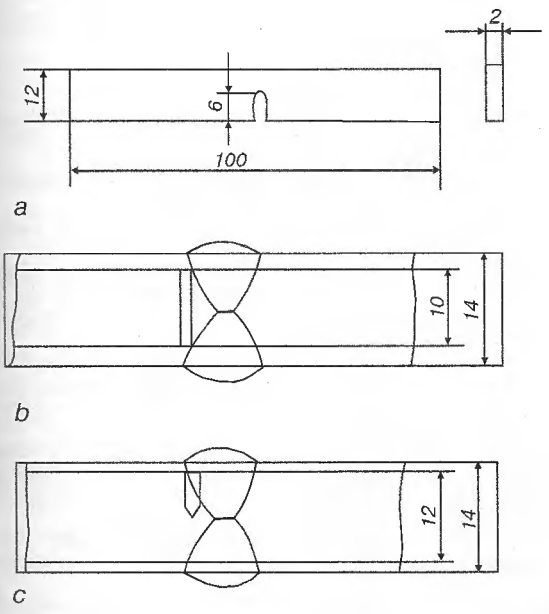

Figure 1. Schemes: *a* — general view of LTS3 specimen; *b* — cutting of specimens for impact strength test; *c* — cutting of LTS3 specimens [7].

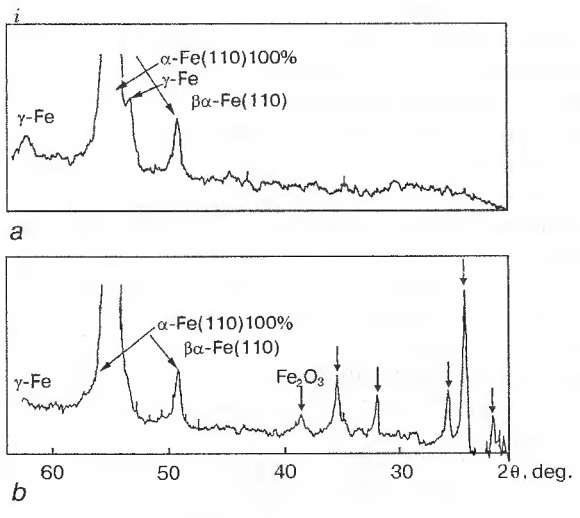

Figure 2. Roentgenograms of HAZ of 12GN3MFAYuDR steel joints welded with 250 °C preheating (*a*), and also with combination of preheating and postweld heating at 250 °C for 4 h (*b*).

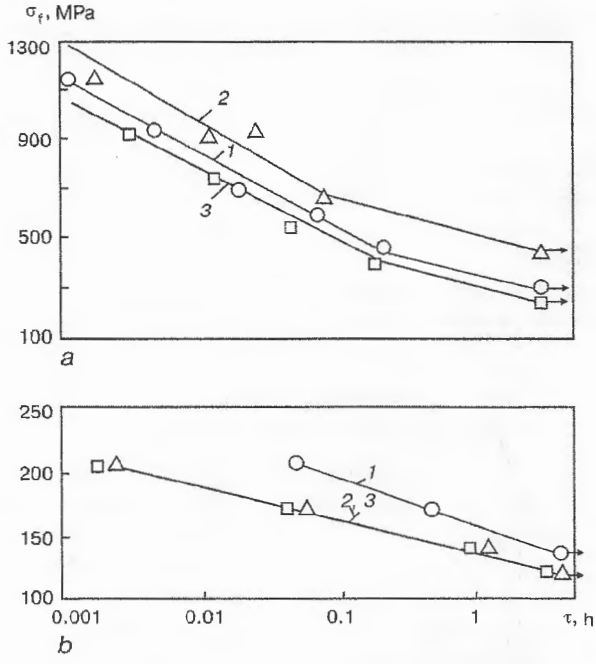

Figure 3. Resistance of steels 12GN3MFAYuDR (*a*) and 14KhGN2MDAFB (*b*) to a delayed fracture: *1* — without preheating; *2* — T_{pr} = 130 °C; *3* — T_{pr} = 250 °C.

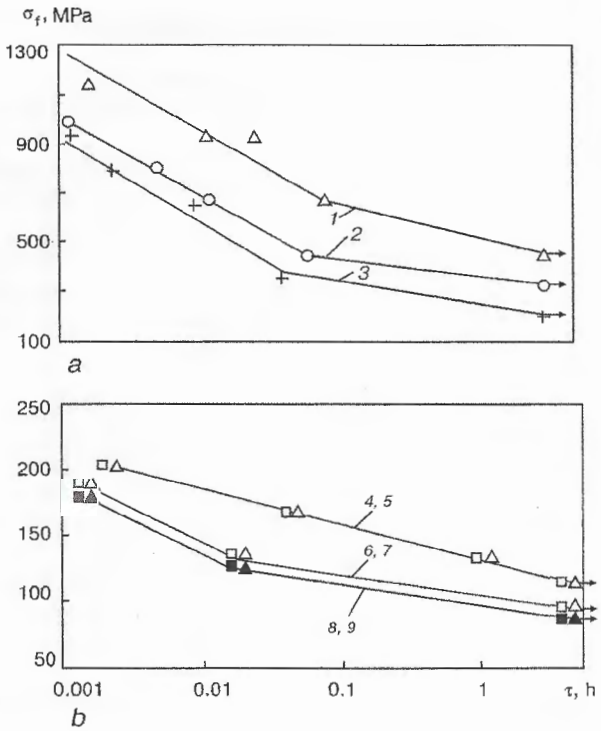

Figure 4. Resistance of steel 12GN3MFAYuDR welded joints to a delayed fracture: (*a*) *1* — T_{pr} = 130 °C without T_{pw}; *2* — T_{pr} = 130 °C, T_{pw} = 130 °C, τ = 2 h; *3* — T_{pr} = 130 °C; T_{pw} = 130 °C; τ = 4 h; 14KhGN2MDAFB (*b*): *1* — T_{pr} = 130 °C without T_{pw}; *2* — T_{pr} = 250 °C without T_{pw}; *3* — T_{pr} = 130 °C, T_{pw} = 130 °C; τ = 2 h; *4* — T_{pr} = 130 °C; T_{pw} = 130 °C; τ = 4 h; *5* — T_{pr} = 250 °C; T_{pw} = 250 °C; τ = 2 h; *6* — T_{pr} = 250 °C, T_{pw} = 250 °C, τ = 4 h

As to the resistance of HAZ metal to a delayed fracture, then the above-mentioned steels react to the conditions of preheating welded joints differently depending on Σ Al, V and Nb. During investigations the real specimens of welded joints were hydrogenized electrolytically up to 5.0 – 6.0 ml/100 g content of diffusible hydrogen, and then they were tested using a scheme of a three-point bend loading [8]. Approximately the same methodological approaches were used in works [9, 10] for evaluation of a delayed fracture of the welded joints.

In steels 12GN3MFAYuDR and 12GN2MFAYu (Σ Al, V, Nb ≤ 0.15 %) the preheating to 130 °C promoted the increase in σ_f of specimens LTS3, and, consequently, in the resistance of HAZ metal to the delayed fracture (Figure 3, *a*). The higher temperature of preheating (T_{pr} = 250 °C) for these steels is undesirable as it leads to a reverse result, i.e. to a decrease in resistance of the welded joints to a delayed fracture.

For steel 14KhGN2MDAFB (Σ Al, V, Nb = 0.27 %) the preheating at temperature 130 – 250 °C reduces the stress σ_f by more than 20 % as compared with welding without it (Figure 3, *b*). As the additional investigations for this steel showed the preheating should not exceed $T_{pr} \approx 90 - 100$ °C.

The postweld heating of welded joints contributed in all cases to the decrease in σ_f of the specimens LTS3 (Figure 4).

The investigations proved the necessity in limiting the preheating temperature ($T_{max} \approx 80 - 130$ °C) depending on the content of carbide - and nitride-forming elements in alloyed steels, and, when possible, in reduction of time of staying welded joints at this temperature. As to the postweld heating, then it is rational to eliminate such technological procedure from the process of manufacture of welded structures made from high-strength alloyed steels.

REFERENCES

1. Grishchenko, L.V., Kozlov, A.V., Fastovsky, V.M. (1981) Calculation of duration of preheating butt joint for welding. *Problemy sudostroyeniya. Welding*, **31**, 40 – 47.
2. Rak, I., Glina, Y. (1986) *A case of preheat cracking of HSLA steel*. IIW IX-1430–86.
3. Kozlov, R.A. (1969) *Hydrogen in welding hull steels*. Leningrad: Sudostroyeniye.
4. Musiyachenko, V.F. (1983) *Weldability and technology of high-strength steel welding*. Kiev: Naukova Dumka.
5. Babaskin, Yu.Z., Shpitsyn, Yu.Ya., Aftandilyants, E.G. (1987) *Sparsely-alloyed steels*. Kiev: Naukova Dumka.
6. Hrivnyak, I. (1984) *Weldability of steels*. Moscow: Mashinostroyeniye.
7. Makarov, E.L. (1981) *Cold cracks in welding alloyed steels*. Moscow: Mashinostroyeniye.
8. Kasatkin, S.B., Mikhoduj, L.I., Gordonny, V.G. (1996) Methodological approaches to an integrated study of delayed and brittle fracture of welded joints of high-strength low-alloyed steels. *Avtomaticheckaya Svarka*, **2**, 58 – 60.
9. Pokhodnya, I.K., Shvachko, V.I. (1997) Physical nature of hydrogen-induced cold cracks in structural steel welded joints. Ibid, **5**, 3 – 12.
10. Savage, W.F., Nippes, E.F., Tokunage, Y. (1987) Hydrogen induced cracking in HY-130 steel weldments. *Welding Journal*, **4**, 118 – 126.

ADHESION OF TITANIUM PARTS TO STEEL FIXTURE DURING DIFFUSION BONDING

S.N. FYODOROV[1], A.V. BONDAR[1], V.V. PESHKOV[2] and V.V. SHURUPOV[2]
[1]Mechanical Engineering Plant, Voronezh, Russia
[2]State Technical University, Voronezh, Russia

ABSTRACT

The influence of temperature and welding time on the strength of adhesion of steel 20 and 12Kh18N10T to VT6 titanium alloy is considered. Comparison of the results of static rupture tests with the topography of the fracture surface of the adhesion regions and their phase composition allows stating that in contact interaction of VT6 alloy with steel 20 the titanium surface is blocked by carbide-containing films, which prevents development of the adhesion process. Therefore, in diffusion bonding of titanium structures it is recommended that fixture should be made from low-carbon steels.

Key words: adhesion, steel fixture, thin-walled titanium structures, diffusion bonding, mechanical tests, fractography, intermetallic phases, carbides.

Diffusion bonding of titanium involves contact and interaction between workpieces being joined and the process fixture. At a bonding temperature $T_{bond} \approx 0.6\ T_{melt}$ this interaction can lead to an extremely undesirable phenomenon of adhesion, in which a workpiece sticks to the fixture.

The problem of adhesion is especially pressing in the manufacture of large-sized thin-walled honeycomb titanium structures, where the fixture elements are made of steel. Steel is the most affordable structural material and it meets all requirements (from the standpoint of mechanical properties) imposed on the fixture plates that transfer a compressive load to the workpieces joined [1]. For example, in bonding panels 1000×500 mm in size, if they stick to the technological plates with a strength of about 1 % of that of the base metal and over the area of 1 % of that of a workpiece, a force of 10^4 N will be required to separate the fixture. This can result both in general deformation of the thin-walled structure and in local fractures of the load-carrying skin (explosions), leading to a decrease in service characteristics of the structure.

The purpose of the work described was to evaluate the effect of a type of steel on the kinetics of its adhesion to titanium under conditions of diffusion bonding.

Experiments were conducted on samples of titanium alloy VT6, which is used for making load-carrying skins of the thin-walled structures, as well as steels 20 and 12Kh18N10T used to make the fixture plates. Development of the process of adhesion between titanium and steel was estimated from results of mechanical static tension tests of standard «Gagarin» specimens with a gauge length diameter of 8 mm, as well as from the data of fractography of the fracture surface supplemented by X-ray phase analysis. Samples 16 mm in diameter and 30 mm high were butt joined in vacuum of not less than 10^{-2} Pa within a temperature range of 850 – 975 °C and under a specific compressive load of 2 MPa, which is a typical load used for diffusion bonding of thin-walled structures [2].

Results of the mechanical tests indicate that a relative adhesion strength calculated from the commonly accepted expression $\sigma_t = P / F$ (where P is the fracture load and F is the nominal cross section area of the test specimen) for a combination of alloy VT6 and steel 12Kh18N10T within the bonding temperature range, although it remains low, exhibits a trend to increase with time (Figure 1, *a*).

Comparison of the adhesion strength σ_t with the size of a formed physical contact F_c suggests that there is no proportional dependence between F_c and σ_t. Moreover, analysis of the effect of the bonding temperature T_{bond} and bonding time τ on the actual adhesion strength calculated from the $\sigma_t = P / F_c$ relationship shows that metal in the adhesion regions (Figure 1, *b*) loses strength with an increase in the temperature and time, i.e. the adhesion strength can be different within the same area of the formed physical contact.

The $\sigma_t = F_1(t, \tau)$ and $\sigma_a = F_2(t, \tau)$ relationships are of a bit different character for the case of contact of alloy VT6 with steel 20 (Figure 2). After bonding at a temperature of 850 – 900 °C, the specimens fractured during machining because of a low strength of the bond. In this case, although the mechanical tests did fix the relative adhesion strength, σ_t, at 950 and 975 °C it remained lower than in the case of contact of alloy VT6 with steel 12Kh18N10T. The actual adhesion strength σ_a for bonding temperatures of 950 and 975 °C showed a trend to growth with an increase in time to more than 60 min.

Fractography of the mating surfaces of the titanium samples after their interaction with the steel samples reveals a fundamental effect of both type of steel and bonding conditions (t, τ) on the topography of the fracture surface.

In the case of alloy VT6 in contact with steel 12Kh18N10T, fracture of the adhesion regions formed at a temperature of 850 °C is of a quasi-tough character, showing the presence of the fine tear ridges (Figure 3, *a*, *b*). This character of fracture suggests that interaction of the mating surfaces ends with the formation of metallic bonds, and metal within the adhesion zone has some strength factor for ductility.

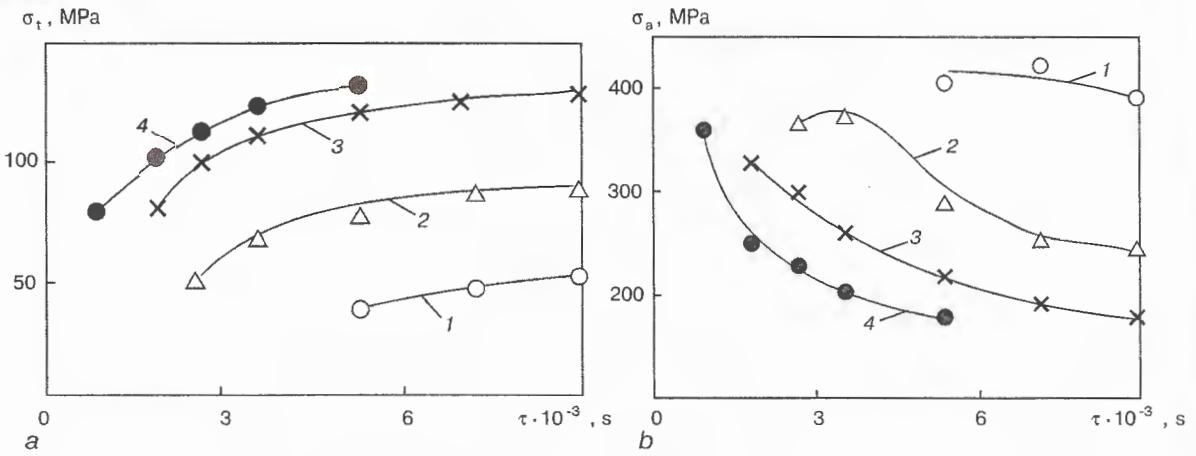

Figure 1. Effect of the bonding time on relative σ_t (*a*) and actual σ_a (*b*) strength of adhesion of alloy VT6 to steel 12Kh18N10T at temperatures, °C: *1* — 850, *2* — 900, *3* — 950, *4* — 975.

Results of X-ray phase analysis indicate that there are no intermetallic phases in fractures of the adhesion regions, although the diffusion zones are present. This fact is proved by an increase of up to 5100 MPa in microhardness of titanium within the contact zone (the base metal has hardness of 3900 MPa).

After bonding at a temperature of 900 °C for 90 min, fracture of the adhesion regions is similar to that considered above (Figure 4, *a*): the topography of the fracture surface is characterized by the presence of the tear ridges formed during the tensile tests. But further increase in the bonding time is accompanied by a qualitative change in the topography of the fracture surface (Figure 4, *b*). Indications of an inter-phase fracture can be seen in the fractograms. It can be assumed that this fracture is a brittle cleavage of the interface between the metal base of titanium alloy VT6 and the diffusion layers formed at its surface as a result of interaction with steel 12Kh18N10T and heterodiffusion of nickel, iron and chromium into titanium.

Cleavage of the interface is accompanied by the formation on the fracture surface of regions with a relief of the type of small pits. (Figure 4, *b*). The large number of very small pits 0.4 – 0.8 μm in size present on the fracture surface are indicative of a high rate of nucleation of local microfractures, which can be caused by a considerable

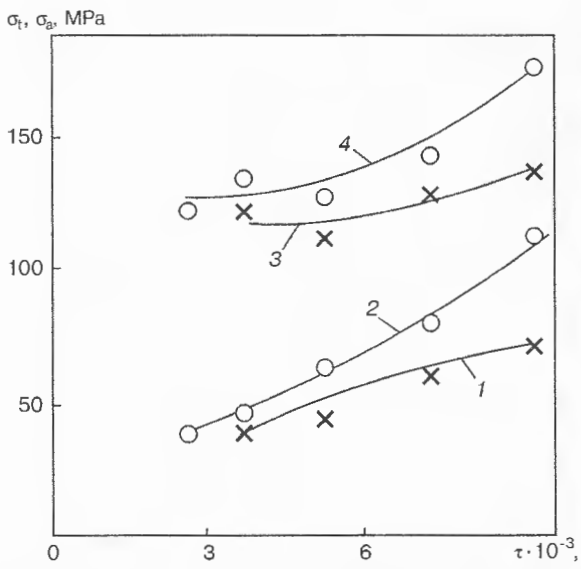

Figure 2. Effect of the bonding time on relative σ_t (*1*, *2*) and actual σ_a (*3*, *4*) strength of adhesion of alloy VT6 to steel 20 at temperatures, °C: *1*, *3* — 950, *2*, *4* — 975.

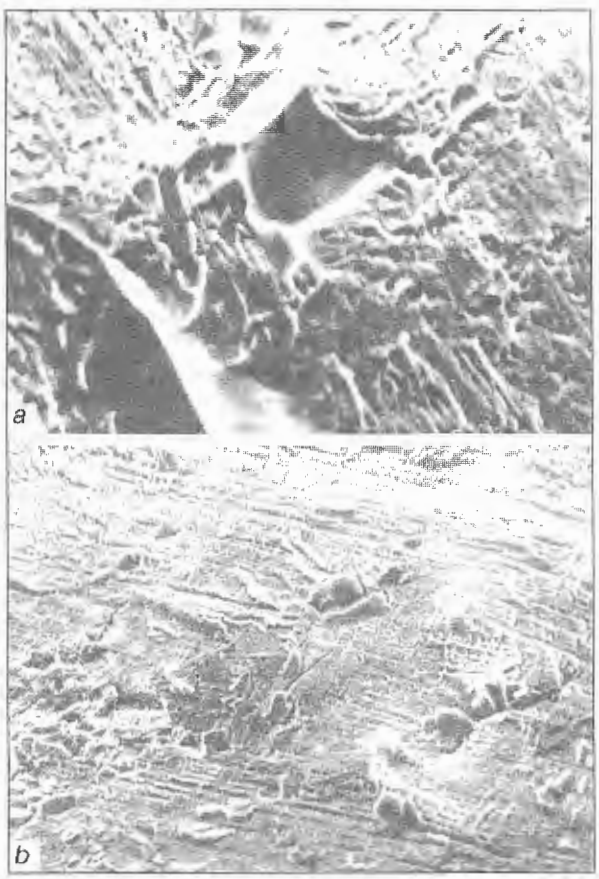

Figure 3. Topography of the fracture surface in regions of adhesion of alloy VT6 to steel 12Kh18N10T after bonding at 850 °C and at magnifications: *a* — (×1280), *b* — (×6000) (reduced by 0.67).

heterogeneity of material in the adhesion regions, as compared with the base metal.

The mechanism of fracture and the resulting topography of the fracture surface depend upon the energy generated at the interface, which is the place of occurrence of fracture [3]. The amount of this energy in the diffusion bonds between dissimilar metals may change considerably as a result of development of two competing thermally activated processes, such as the formation of metallic bonds (leading to a decrease in the interface energy) and change in chemical composition at the interface, e.g. as a result of heterodiffuion and segregation of metal impurities (leading to an increase in the interface energy). Apparently, it is the second process that with an increase in the bonding temperature and time determines properties of the interface, this showing up as the effect of bonding parameters on the topography of the fracture surface.

In tensile tests, cracks forming the fracture surface propagate within the bonding zone not only in the plane of contact between the pieces joined (or in the plane of location of the diffusion layers), but also in a direction normal to the mating surfaces. The diffusion layers in this case fracture by the cleavage mechanism to form «serrations» the thickness of which seems to depend upon the, size of the diffusion zone, its phase and chemical composition (Figure 4, *b*).

Increasing the bonding time to 150 min at 900 °C is accompanied by further development of the diffusion processes within the zone of contact and, therefore, by transition from the inter-phase fracture of the adhesion regions to the intra-phase brittle cleavage (Figure 4, *c*), while the fracture plane changes its orientation in transition from one region of the diffusion zone to the other. This is associated with a crack branching along different planes.

It is a known fact [3] that one of the causes of fracture by the cleavage mechanism is a low ductility of the material tested. Therefore, the character of fracture observed in our case should be related to embrittlement of the surface of titanium alloy as a result of formation of the diffusion zones and intermetallic phases.

Results of X-ray analysis are indicative of the presence of intermetallic phases TiFe and $TiFe_2$ in the fracture zones of the adhesion regions after bonding at 900 °C for 150 min.

Drastic decrease in the actual strength of adhesion of alloy VT6 to steel 12Kh18N10T under the above bonding conditions (see Figure 1, *b*) should be related particularly to the formation of intermetallic phases and embrittlement of metal in the adhesion regions. With an increase in the bonding temperature of up to 950 – 975 °C the effect of the bonding time on the topography of the fracture surface has the same trend as at 900 °C.

Characteristic fractograms of surfaces of alloy VT6 after its contact with steel 20 are shown in Figure 5. After bonding at 850 and 900 °C, the mating surfaces show no traces of fracture in the adhesion regions (Figure 5, *a*, *b*). The surfaces are covered with non-metallic films, which is proved by the presence on electron fractograms of the potential contrast [4] and cracking of the surface during its deformation. X-ray phase analysis shows that these films contain carbides that are likely to form as a result of interaction of titanium with carbon contained in steel.

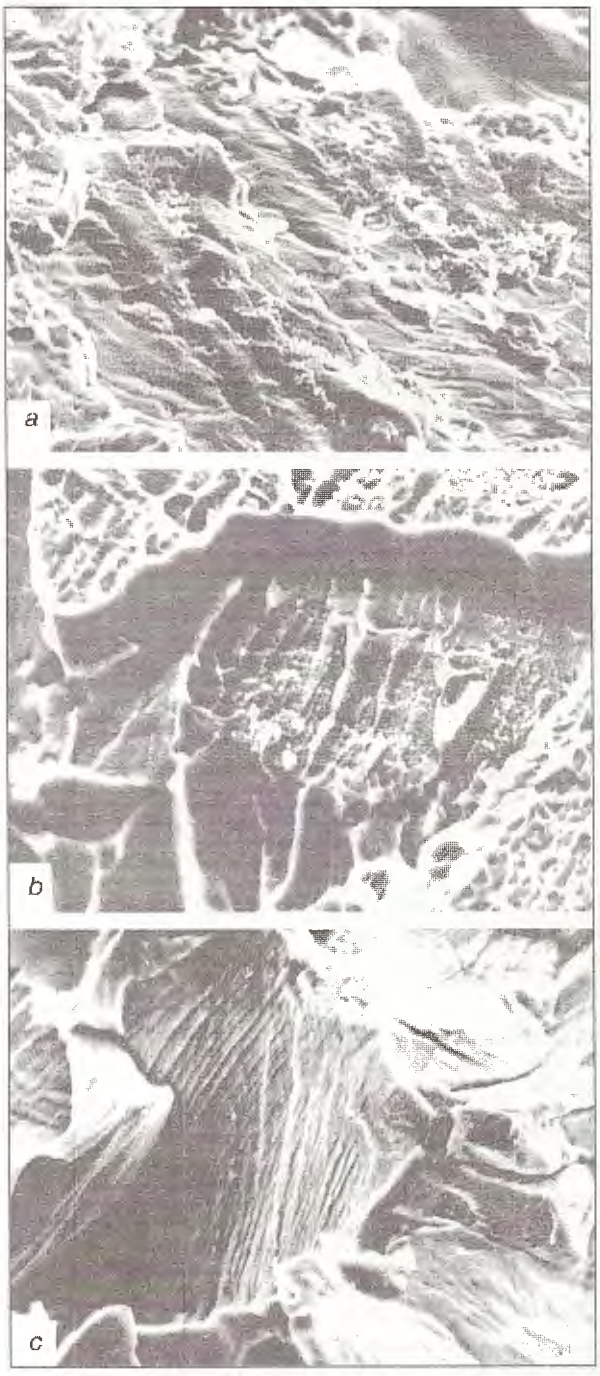

Figure 4. Effect of the bonding time on topography of the fracture surface in regions of adhesion of alloy VT6 to steel 12Kh18N10T after bonding at 900 °C and time, min: *a* — 30 (×5500), *b* — 90 (×5500), *c* — 150 (×10000) (reduced by 0.67).

Increasing the bonding temperature to 950 – 975 °C leads to the formation of centres of adhesion between the mating surfaces (Figure 5, *d*), which are characterized by a low value of stresses required for their fracture (see Figure 2). The observed character of fracture of the adhesion

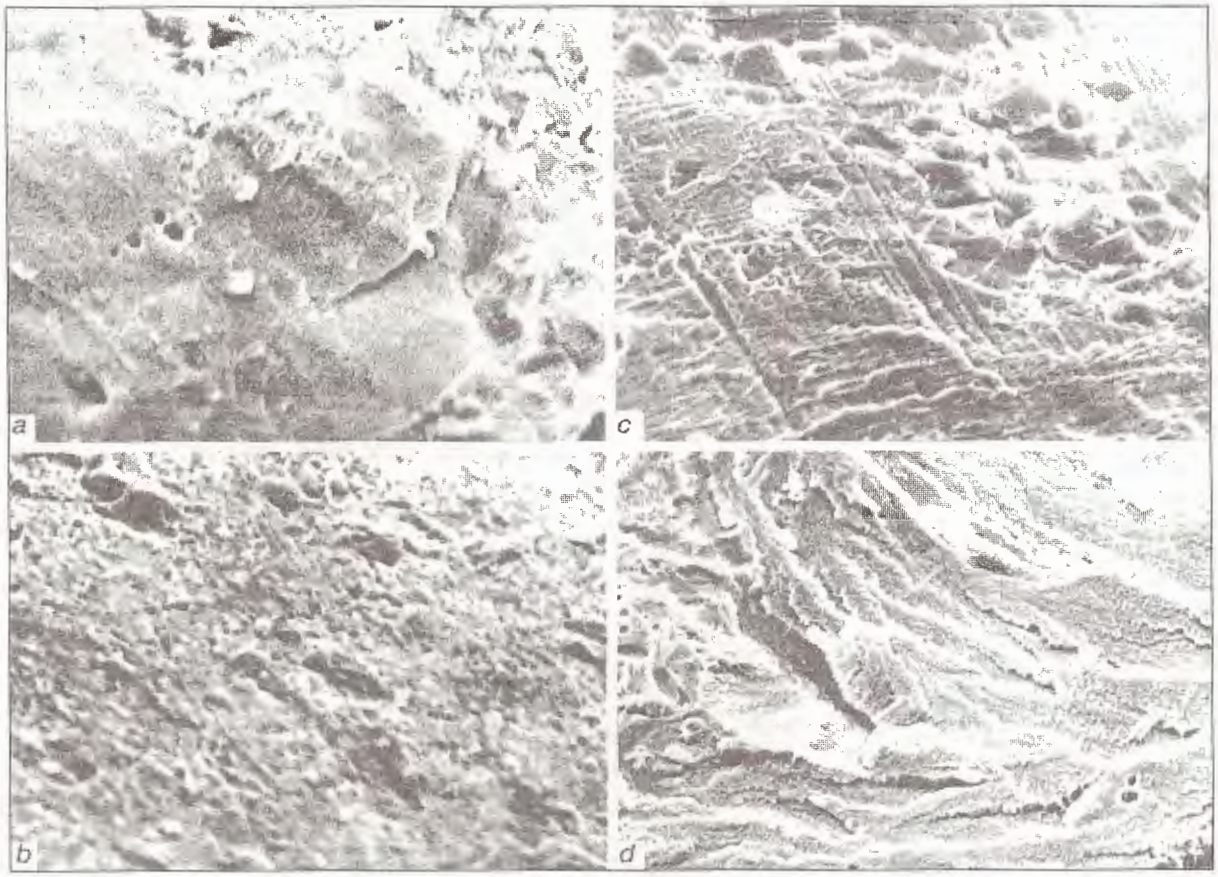

Figure 5. Effect of the bonding time on topography of the fracture surface in regions of adhesion of alloy VT6 to steel 20 after bonding at temperature, °C: *a* — 850 (×10000), *b* — 900 (×10000), *c* — 950 (×5000), *d* — 975 (×5000) (reduced by 0.67).

centres suggests that the process of interaction of titanium with steel 20 at $\tau \leq 60$ min is completed with the formation of weak chemical bonds.

CONCLUSIONS

1. In contact interaction of alloy VT6 and steel 12Kh18N10T the actual strength of the adhesion regions decreases with an increase in the bonding time, which is associated with embrittlement of titanium within the contact zone caused by diffusion into titanium of iron and alloying elements contained in steel 12Kh18N10T, as well as formation of intermetallic phases.

2. There is no adhesion in contact interaction of alloy VT6 and steel 20 at a temperature of 950 °C, as the titanium surface is blocked by the carbide-containing films. At $t \leq 950$ °C and $\tau > 60$ min the actual strength of adhesion tends to increase, which seems to be associated with development of mutual diffusion of the materials in contact.

3. From the standpoint of development of the adhesion process, it is recommended that the technological fixture for diffusion bonding of thin-walled titanium structures be made from low-carbon steels.

REFERENCES

1. Bondar, A.V., Peshkov, V.V., Kireev, L.S., Shurupov, V.V. (1998) *Diffusion bonding of titanium and its alloys.* Voronezh: The Voronezh State University.
2. Peshkov, V.V., Gusev, S.I. (1984) Technological parameters of the process of diffusion bonding of honeycomb structures from titanium alloys. *Svarochnoye Proizvodstvo*, **10**, 12 – 14.
3. Kolachev, B.A., Malkov, A.V. (1983) *Physical principles of fracture of titanium.* Moscow: Metallurgiya.
4. Milyutin, V.I., Peshkov, V.V., Kolachev, B.A., Rodionov, V.N. (1988) Detection of oxides on the surface of titanium by scanning electron microscopy. *Svarochnoye Proizvodstvo*, **11**, 37 – 39.

SOLDERS OF THE Sn–Ni–Ge SYSTEM FOR VACUUM SOLDERING

V.F. KHORUNOV, V.I. SHVETS, G.N. GORBAN and L.K. DOROSHENKO
The E.O. Paton Electric Welding Institute, NASU, Kyiv, Ukraine

ABSTRACT

Tin-rich alloys of the Sn–Ni–Ge system used as solders show promise for erection-assembly and repair operations conducted in the orbit. Results of investigations into microstructure, phase composition, melting temperature ranges, operational and strength properties of alloys, which served as the basis for selection of a range of optimal solder compositions, are presented. Examples of practical application of the solders for the fabrication of truss structures are given.

Key words: *vacuum soldering, solder, microstructure, phase composition, spread, space.*

For long-duration and especially long-distance space flights, it is necessary to have on board a spacecraft a set of means and devices intended for repair of the craft casing, equipment and instruments. The repair operations can be done on different metallic (based on iron, nickel, titanium, copper, aluminium, etc.) and non-metallic (different types of ceramics, carbon materials, intermetallic alloys, etc.) materials.

The most rational method for doing these operations is soldering. In this process the metal melts with a melting point below that of the base metal are used to repair or join pieces. An important advantage of the soldering process is that it is regulated by the surface tension forces that retain the molten metal on the mating surfaces and exclude the possibility of detachment of metal droplets, which may be dangerous for a crew. As far as welding is concerned, it involves various excitation factors (magnetic, electric), as well as molten metal transfer, which makes detachment of droplets not only probable, but also hard-to-control.

The process which is best elaborated for earth conditions in terms of consumables and technologies is high-temperature vacuum brazing, as it provides joints of a good quality (strength, corrosion resistance, etc.). However, this process is and will be hard to perform in orbit in the near future because of a high power consumption and the need to maintain the required thermal conditions within a very narrow high-temperature range.

Low-temperature vacuum soldering has not gained wide acceptance under earth conditions. Practical application of this process is complicated by the absence of thermal activation and by segregation on the surface of high-temperature compounds which hamper wetting [1].

So, the challenge was to develop a solder which could work under conditions of low-temperature vacuum soldering. The materials to be joined included aluminium and aluminium-base composites, as well as iron- and nickel-base alloys (e.g. 36NKhTYu alloy).

As proved by analysis, alloys with a contact angle of the tin type, belonging to the Sn–Ni–Ge system, show promise for the use as solders for low-temperature vacuum soldering.

As compared with other low-melting point metals, tin has a low value of vapour pressure (1.33×10^{-8} Pa at 582 °C [2]), it is characterized by ductility, high thermal and electrical conductivity and is capable of wetting the majority of metals. Germanium present in tin within a certain temperature-concentration range acts as a surface-active element [3] and is characterized by a high solubility in iron and nickel (up to 17 and 12 at. %, respectively), which are used as the base of many structural materials. It is this fact that is responsible for its active effect on structure and spread of alloys, and on interaction of solid and liquid phases during soldering.

According to the binary constitutional diagrams Sn-Ge and Sn–Ni, germanium and nickel are almost insoluble in tin. This offers the possibility of an additive hardening of a solder by precipitation of the redundant phases, i.e. germanium and nickel stannides [4]. The constitutional diagram of the Sn–Ni–Ge system has been studied only for the nickel-rich region at a germanium and nickel content of up to 50 at. % each [5].

The objective of the work described in this article was to investigate microstructure, phase composition, melting and solidification processes and operational properties of alloys of the Sn-Ni-Ge system in the tin-rich region.

Sections of the ternary constitutional diagram at a constant content* of 2 % Ni and 5 % Ge were studied. Alloys of group one were investigated within a range of concentration of Ge equal to 1 – 30 % and alloys of group two — within a range of concentration of Ni equal to 4 – 25 %.

The alloys were melted in an induction furnace in the argon atmosphere. Upon achieving a homogeneous liquid, the melt was pumped by means of a backing pump into a quartz tube and cooled in water.

Optical microscopes MIM-8 and «Neofot-2» were used for metallography. Microstructure was revealed as early as at the stage of polishing, owing to a substantial difference in hardness of the structural components. The effect of the cooling rate of the melt on the microstructure was determined by comparing the alloys in the as-quenched condition and after thermal analysis (the cooling rate was 80 °C/min). Electron probe X-ray analysis (EPXA) was done using the «Cameca» MS-46 microscope-microanalyser, differential thermal analysis (DTA)

*Here and below the contents of elements are given in wt.%.

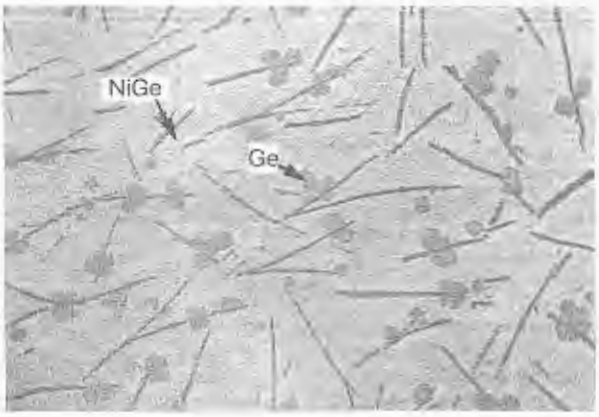

Figure 1. Microstructure of quenched alloy Sn–2Ni–2Ge (×200) (reduced by 0.67).

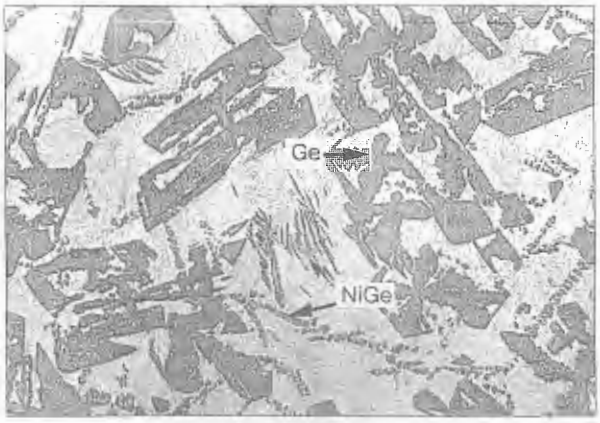

Figure 3. Microstructure of alloy Sn–2Ni–2Ge after thermal analysis (×200) (reduced by 0.67).

was conducted using the VDTA-8M unit and X-ray phase analysis — using the DRON-3M diffractometer. Identification of phases was done by comparing the experimental values of inter-planar distances with the tabular values taken from the ICPDS file.

Spread of the alloys was determined by measuring the trace surface area according to GOST 23904–79 [6]. The experiments were conducted in vacuum of 10^{-2} Pa at a temperature of 600 °C. Alloy 36NKhTYu with a nickel coating was used as the substrate. The soldered joints were tensile tested using the RMU–0.05 testing machine at a room temperature and a grip travel speed of 16 mm/min.

It was established that microstructure of the alloys of the Sn–2Ni–1 – 30Ge system was a solid solution of nickel and germanium in tin with the inclusions of the Ge- and NiGe-base phases* (Table 1).

In the quenched samples, the inclusions of germanium have a shape of equiaxed polyhedrons and those of NiGe — of filamentary crystalline grains (Figure 1). Volume fraction of the inclusions increases with an increase in the germanium content (Figure 2). Decrease in the cooling rate of the melt during solidification leads to coarsening of the structural components. In this case the germanium crystalline grains take the shape of a geometrical cut, while NiGe looks like a series of inclusions of a similar shape, duplicating in a linear direction (Figure 3).

Characteristic feature of the microstructure of the samples after thermal analysis, which was noted by analysis of the curves of distribution of elements in the alloy (Figure 4) was the presence of inclusions consisting of alternating Ge and NiGe layers. It is likely that in the concentration range of the system under consideration, the L ↔ Ge + NiGe eutectic transformation takes place, like in the Ni–Ge binary system.

Melting (solidification) of alloys of the Sn–2Ni–1 – 30Ge composition is a multi-stage process, according to the DTA results (Table 2, Figure 5). The low-temperature peak in the region of the melting point of tin corresponds to melting of the alloy matrix. The second peak, according to the results of the microstructural investigations, seems to be a thermal effect of the eutectic transformation to form the NiGe compound. Position of the third peak seen at a germanium content of more than 20 % depends upon the concentration of germanium in the alloy. As its content increases, the peak shifts to a region of higher tempera-

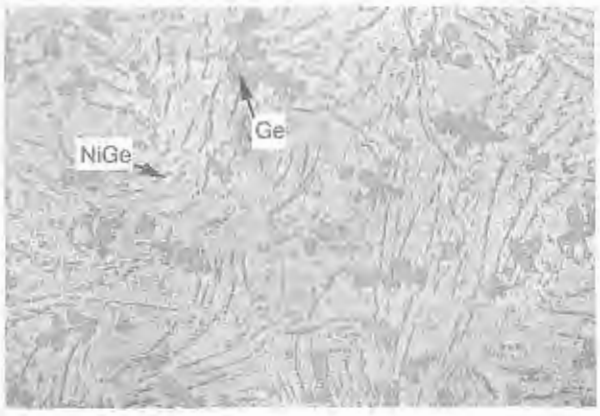

Figure 2. Microstructure of quenched alloy Sn–2Ni–10Ge (×200) (reduced by 0.67).

Table 1. Results of EPXA and X-ray phase analysis of Sn–2Ni–1 – 30Ge alloys

Structural component	*Content of elements, wt.%*			*Phase*
	Sn	*Ni*	*Ge*	
Matrix	Balance	0.10 0.12	0.20 – 0.55	Sn-base solid solution
Inclusions	5 – 10	–	90 – 95	Ge
	3 – 6	42 – 44	52 – 54	NiGe(55 % Ge)

Table 2. Results of DTA of Sn–2Ni–5 – 30Ge alloys

Chemical composition of alloys, %*		*Temperature, °C*		*Melting point, °C*
Ni	*Ge*	*Solidus*	*Liquidus*	
2	5	230	600	370
2	15	230	650	420
2	20	230	650	420
2	25	210	660	450
2	3	210	740	530

*Sn — balance.

*No reflections corresponding to the NiGe compound were seen in the diffraction patterns, because of its small volume fraction in the alloy. Identification of the phase was done on the basis of the EPXA results.

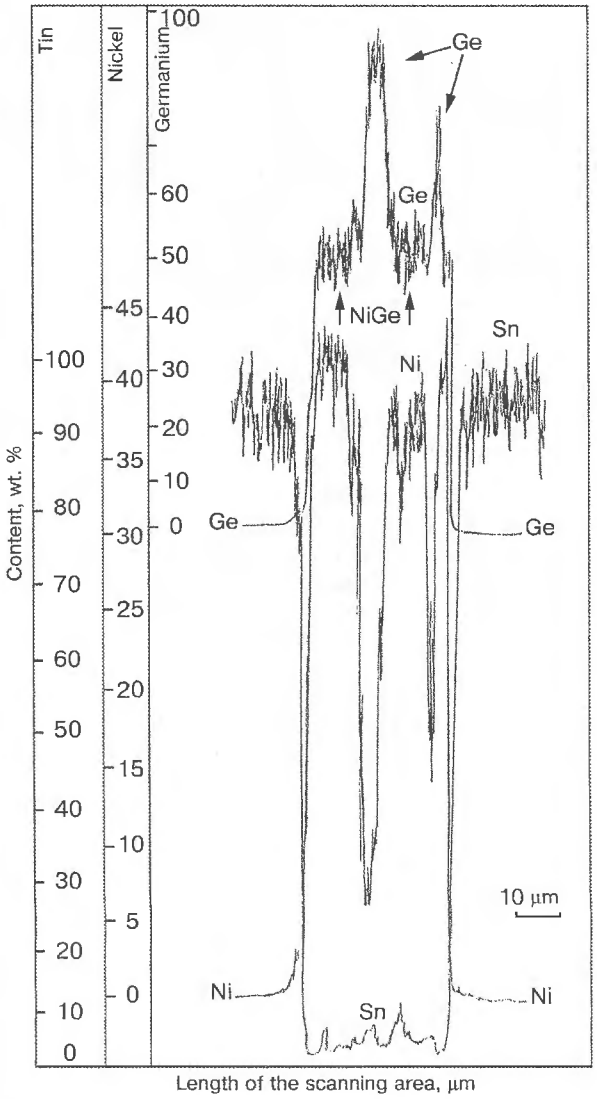

Figure 4. Distribution of elements in a crystalline grain. Alloy Sn–2Ni–10Ge after thermal analysis.

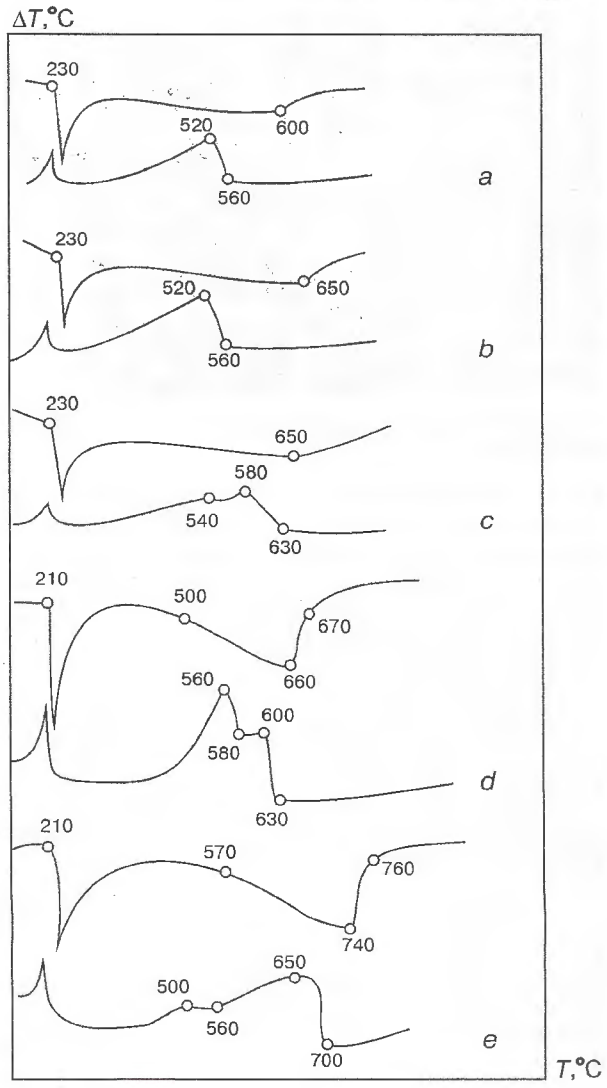

Figure 5. Thermogram of alloys of the Sn–2Ni–...Ge system with Ge content, wt. %: *a* — 5; *b* — 15; *c* — 20; *d* — 25; *e* — 30.

tures and seems to characterize solidification of primary germanium.

Microstructure of alloys of the Sn–4 – 20Ni–5Ge composition, like that of alloys of the Sn–2Ni–1 – 30Ge composition, is a solid solution of germanium and nickel in tin, containing some inclusions. However, the inclusions in this case are formed from phases based on nickel stannides, i.e. NiSn and Ni_3Sn_4 (Table 3). An increase in the nickel content of the alloys is accompanied by an increase in the intensity of reflections corresponding to the NiSn and Ni_3Sn_4 compounds in the diffraction patterns, i.e. growth of the volume fraction of the inclusions.

In the microstructure of the quenched samples, the NiSn-base phase is seen in the form of branched dendrites, while the Ni_3Sn_4-base phase has the form of acicular crystalline grains, the volume fraction of the latter being comparatively small (Figure 6).

According to the distribution of elements in the alloy (Figure 7), as well as results of chemical analysis of microvolumes (Table 3), germanium is dissolved in the alloy structural components. Germanium is present in the insignificant amounts in the tin-base solution. In the NiSn- and Ni_3Sn_4-base phases its concentration is 8 – 9 and 5 – 7 %, respectively.

Microstructure of the alloys after thermal analysis is characterized by some essential changes, in addition to coarsening of inclusions (Figure 8). The inclusions comprise two phases: the NiSn-base phase is present in bulk of the Ni_3Sn_4-base phase. The peritectic reaction of NiSn + L ↔ Ni_3Sn_4 is likely to occur in the concentration

Table 3. Results of EPXA and X-ray phase analysis of Sn–4–20Ni–5Ge alloys

Structural component	*Content of elements, wt. %*			*Phase*
	Sn	*Ni*	*Ge*	
Matrix	Balance	0.10 – 0.12	0.20 – 0.55	Sn-base solid solution
Inclusions	43 – 50	39 – 41	8 – 9	NiSn (66.91 % Sn)
	62 – 64	28 – 30	5 – 7	Ni_3Sn_4 (72.95 % Sn)

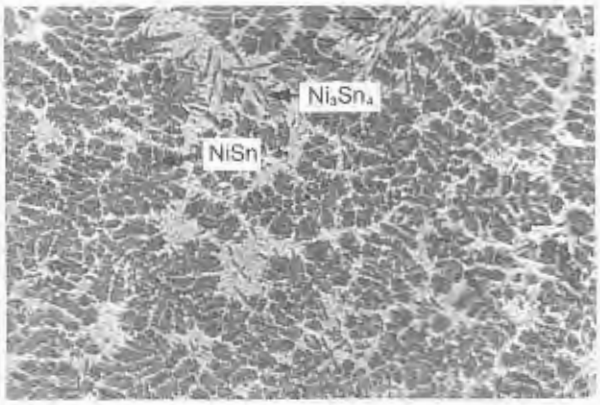

Figure 6. Microstructure of quenched alloy Sn–15Ni–5Ge (×200) (reduced by 0.67).

Figure 8. Microstructure of alloy Sn–15Ni–5Ge after thermal analysis (×80) (reduced by 0.67).

range under consideration. The peritectic transformation process occurs either through dissolution of primary crystalline grains NiSn and precipitation of Ni_3Sn_4 from the liquid (the quenched samples) or through precipitation of Ni_3Sn_4 at the primary crystalline grains of NiSn and subsequent growth both towards the liquid phase and towards NiSn (the samples after thermal analysis).

According to the DTA data (Table 4, Figure 9), the process of melting (solidification) of alloys of the Sn–4 – –20Ni–5Ge composition is multi-stage, i.e. three peaks are seen in the thermograms.

Position of a low-temperature peak is identical to that seen in the thermograms of alloys of the Sn–2Ni–1 – 30Ge composition and corresponds to melting of the matrix.

The highest-temperature peak seems to be caused by a thermal effect of formation of the primary NiSn phase, whereas the second peak is caused by the peritectic transformation leading to the formation of the Ni_3Sn_4 phase. It should be noted that both high-temperature peaks shift to a higher temperature range with an increase in the nickel content of the alloys.

Therefore, the Sn–Ni–Ge system alloys with a contact angle of the tin type comprise the tin matrix reinforced by inclusions of the redundant phases of the binary systems that limit the given ternary system (Ge, NiGe, NiSn, Ni_3Sn_4). The alloys have a wide melting range. The soli-

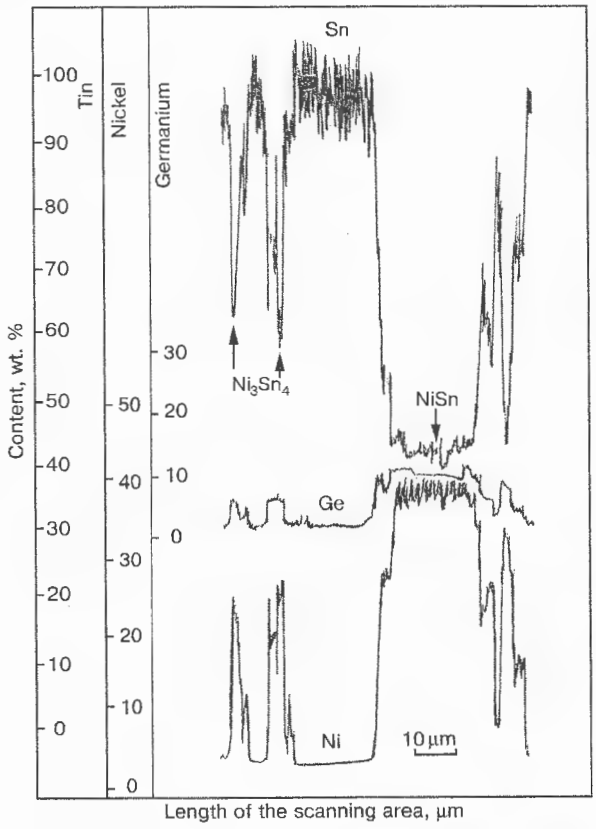

Figure 7. Distribution of elements in quenched alloy Sn–15Ni–5Ge.

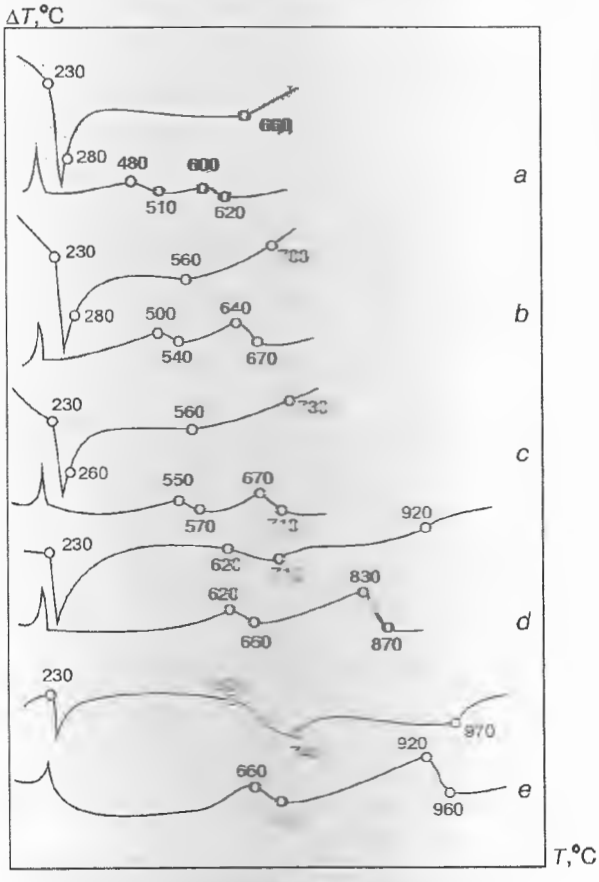

Figure 9. Thermogram of alloy [illegible] the Sn–5Ge–...Ni system with Ni content, wt. %: *a* — 4; *b* — [illegible] — 15; *e* — 20.

Table 4. Results of DTA of Sn–4 – 20Ni–5Ge alloys

Chemical composition of alloys*, %		Temperature, °C		Melting range, °C
Ni	Ge	Solidus	Liquidus	
4	5	230	660	430
8	5	230	700	470
10	5	230	730	500
15	5	230	920	690
20	5	230	970	740

*Sn — balance.

Table 5. Spread of solders and tensile strength of soldered joints

Solder	S, mm^2	σ, MPa
Sn–0.2Ni–1.5Ge	116	42
Sn–0.9Ni–1.9Ge	115	49
Sn–5.0Ni–2.0Ge	136	55
Sn–2.5Ni–5.2Ge	137	56
Sn–3.1Ni–3.0Ge	140	58
Sn–2.4Ni–12.1Ge	102	55
Sn–3.0Ni–12.0Ge	75	32

dus temperature of all the alloys corresponds to the melting point of tin, and the liquidus temperature depends upon the nickel and germanium contents.

Spread of the Sn–Ni–Ge system alloys with a contact angle of the tin type is characterized by a clearly defined dependence upon the composition (Figure 10). Analysis of the curves of the concentration dependence shows that an improvement in spread of the Sn–2Ni alloy is seen in adding up to 5.5 % germanium (instead of tin). Further increase in the germanium content leads to a decrease in spread, and at a concentration of 20 % the trace surface area is about 10 mm^2.

Spread of the Sn–5Ge alloy is improved in a similar way in adding up to 2.5 % nickel (instead of tin). It should be noted that deterioration in spread with an increase in the nickel content to more than 2.5 % is more pronounced.

Knowing the metallography and DTA results, it is possible to explain the course of the curves of the concentration dependence of spread.

An increase in the content of nickel and germanium leads to elevation of the liquidus temperature. When the liquidus temperature is higher than the spread temperature, a droplet spreading is a heterogeneous system. This system consists of liquid tin containing germanium and nickel within their solubility limits and crystalline grains of the redundant phases.

In this case, spread is determined by the liquid phase volume, which decreases with further increase in the concentration of nickel and germanium. In the Sn–...Ni–5Ge alloys, tin is part of the composition of the redundant phases (nickel stannides). Thus, in this case, spread decreases more intensively with an increase in the nickel content, as compared with an increase in the germanium content of the Sn–2Ni–...Ge alloy.

For capillary soldering using the Sn–Ni–Ge system solders, it is advisable to apply overheating to a temperature above the solidus temperature. For non-capillary soldering, a more practicable approach is to use a solder in the heterogeneous condition. For this, it is best to apply the solder in the form of a foil or a tinning layer. The foil should be made from quenched ingots with a refined structure.

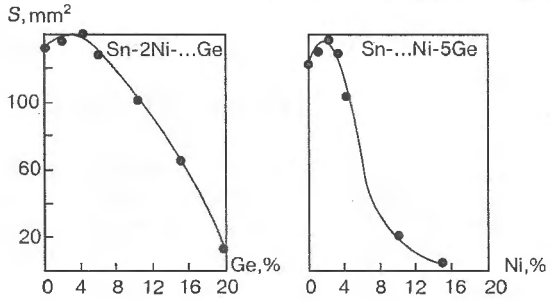

Figure 10. Spread of alloys of the Sn–Ni–Ge system.

The experiments with vacuum soldering showed that the Sn–Ni–Ge system alloys provided good formation and high quality of the soldered joints. Results of tensile tests of the overlapped nickel joints, produced at a soldering temperature of 600 °C using solders with a satisfactory spread are given in Table 5.

The investigations conducted made it possible to define the range of the optimal compositions of soldering alloys, characterized by a good match of maximum values of strength and spread characteristics [7].

For erection-assembly operations to be done under the EVA conditions, the E.O. Paton Electric Welding Institute developed a technology for electron-beam soldering of connections of tubular truss structures made of elastic open-section profiles (36NKhTYu alloy) [8] and a technology for electron-beam non-capillary soldering of connections of truss structures made of AMg5 alloy [9]. These technologies were tested to advantage under laboratory conditions. The Sn–2Ni–4Ge system alloy was employed as the solder.

The experiment on soldering connections of the truss structure elements in space conducted by cosmonauts V.A. Soloviev and A.D. Kizim on board the «Salyut-7» space station yielded positive results and confirmed applicability of the technologies and promising future of the Sn–Ni–Ge system solders for their use under the high vacuum conditions.

REFERENCES

1. Kpansky, E., Erjavec, B., Ros, Z., Golob, V. (1982) Some problems of vacuum soldering. In: *Proc. of the Intern. Confer.: Doc. I-714–82 IIW*. Ljublana (Yugoslavia).
2. Gladkov, A.S., Podvigina, O.G., Chernov, O.V. (1967) *Soldering of electric vacuum device parts*. Moscow: Energiya.
3. Edided byNaidich, Yu.V. (1991) *Surface properties of melts and solids and their utilization in materials science*. Kyiv: Naukova Dumka.
4. Barabash, O.I., Koval, Yu.N. (1986) *Crystalline structure of metals and alloys*. Kyiv: Naukova Dumka.
5. Wang, K., Nashikata, A., Mishima, Y., Suzuki, T. (1990) The Ni–Ge–Sn phase diagram. *Z. Metal*, vol. 81, **12**, 905 – 911.
6. GOST 23904–79. Soldering. *Method for determination of wetting of materials with solders*.
7. Khorunov, V.F., Shvets, V.I., Lapchinsky, V.F., Bulatsev, A.R., Skorobogatov, S.A. (1988) A.c. **1606295** USSR, Int.Cl B23k 35/26. *Solder for nickel soldering*, published 15.10.88, bul. **38**.
8. Zagrebelny, A.A., Gavrish, S.S., Bulatsev, A.R., Khorunov, V.F. *et al.* (1986) Analysis of permanent joints between tubular elements made by welding-soldering and brazing using the VHT hardware. *Advances in Space Metal Technology*, 13 – 22. Kyiv: E.O. Paton Electric Welding Institute.
9. Khorunov, V.F., Lapchinsky, V.F., Shvets, V.I., Shulym, V.F. (1992) Technology for low-temperature vacuum soldering of connections of truss structure elements made of aluminium alloys. *Avtomaticheskaya Svarka*, **2**, 52 – 53.

ABILITY TO RESTORE COATINGS UNDER THE ACTUAL CONDITIONS OF SPACE

B.E. PATON[1], E.S. MIKHAILOVSKAYA[1], V.F. SHULYM[1], A.A. ZAGREBELNII[1], V.P. NIKITSKII[2], I.V. CHYRILO[2] and L.O. NEZNAMOVA[2]
[1]The E.O. Paton Electric Welding Institute, NASU, Kyiv, Ukraine
[2]RSC «Energia», Moscow, Russia

ABSTRACT

To increase the service life of expensive space vehicles it is worthy while to pay attention to testing the equipment and technology for deposition of coatings under the conditions of the object service. The application of the electron beam technology as most feasible under the space conditions is considered. The quality of coatings and methods of technology realization are evaluated.

Key words: coatings, electron beam technology, degradation, near-earth orbit, versatile hardware, coating properties, repair-restoration operations.

The problem of extending the service life of coatings used in the structures of flying vehicles (FV) is still urgent, despite the fact that the current ground technologies are being continuously improved. The aerospace industry is using in its production coatings of the most diverse functional purposes, namely reflective and absorbing temperature control, corrosion-resistant, protective, etc. Also, protective coatings which prevent the degradation of the FV structural materials under their different operational conditions, can be singled out from this list, in particular, in the near-earth orbits (NEO) where such factors of outside influence as atomic oxygen [1–3], micrometeorites and dust [4–6], moisture [7], thermo-chemical and mechanical processes occurring on the materials surfaces acquire the decisive role, and lead to their significant oxidation and erosion. The density of atomic oxygen (O) in NEO is small (approximately 10^9 at./cm^3), this corresponding to the gas density at the residual pressure of 10^{-5} Pa. However, the intensity of O flows bombarding the FV surface, is significant, in view of the high orbital speed ($\geq$ 8 km/s) and is approximately 10^6 at./cm^2 [8]. Under these conditions the impact of the environment on the FV surface is comparable with its bombardment with high-energy (~ 5 eV) O atoms. As a result, metallic materials are characterised by a pronounced oxidation, and the non-metallic ones by erosion and weight loss. According to calculations [1], the degree of degradation of graphito-epoxy composite material for FV with a long functioning period, will be about 0.3 mm during the 11 years cycle of the activity of the sun, and about 0.9 mm during 30 years. Considering, that the design thickness of structural elements of this material is approximately 1.0 to 2.0 mm, in three decades it can be reduced by more than half, this being inadmissible.

Numerous life tests of different materials were conducted by Russian and Ukrainian experts both on the ground and in the orbital stations «Salyut-6», «Salyut-7» and orbital complex «Mir».

The objects of flight studies were all kinds of materials and coatings, namely temperature control coatings, polymer and structural materials, solar battery (SB) elements, optical coatings. Analysis of the change of the tested materials performance was conducted both directly under the flight conditions, and in the ground test laboratories. Physical parameters determining the material performance as a whole, were taken as the criteria of the degree of materials degradation in each concrete case.

For instance, more than 25 types of ceramic and more than 20 lacquer-paint temperature control coatings have been tested. Exposure to raw space environment was from 3 months to 3 to 6 years.

As a rule, during long-term exposure the coatings and materials lost their initial characteristics, changed their properties, and in some cases a significant degradation of the working surfaces was found.

Analysis of the tested polymer materials (fluoroplastic and polyemide films) also points to their properties degradation during long-term service in space environment.

During the flight period of three orbital stations, more than 200 different structural materials were tested. Many of them were tested by NDT methods directly under the flight conditions. Their performance during a service life of up to 10 years was confirmed (for instance, stability of thermal radiation properties of the coatings of radiators of temperature control systems was preserved). However, deterioration of some properties should also be noted, in particular, degradation of the carbon fibre reinforced plastic surface, as well as deterioration of some physical properties of non-metallic structural materials. A graph of the change of dielectric properties of model polymer matrices based on ED-16 epoxy is given as an example (Figure 1). As can be seen from the graph, all the samples demonstrated a smooth lowering of the capacity and conductivity during the entire period of exposure (9 years), which is indicative of the decrease of their strength properties.

Since chemical reactions, and not the mechanical action of microparticles prevail in the mechanism of polymer erosion in NEO [9], thin protective coatings can be applied to prevent destructive surface processes [10, 11], which, as was mentioned above, are rather widely used now in practice. For instance, flexible SB substrates and

outer temperature control surfaces of FV from capton are protected from erosion by Al_2O_3, SiO_2 and other coatings [12], and coatings of magnesium fluoride, silicon nitride, indium oxide alloyed with tin, etc. are applied onto the metallic (silver, aluminium) reflective surfaces of mirrors of the solar-energy power systems for their protection from oxidation [13–15]. Considering that in current FV projects the service life should be about 30 years [16], obvious is the need for periodical restoration of the functional properties of coatings, as well as performance of scheduled repair of their structural elements. These operations can be performed on the Earth, taking FV to orbit in the modern transportation means. However, in view of the high cost of carrier rocket launches, it is more rational to perform the restoration and repair work directly under the conditions of their service.

This paper analyses the possibility of using electron beam technology of material evaporation for coatings deposition in orbit, also with the aim of their protection from degradation, as well as performance of repair-restoration work under these conditions.

Development of electron beam technology of coatings application under microgravity conditions was based on the results of numerous ground and flight experiments which had been conducted by the staff of E.O. Paton Electric Welding Institute and Russian Space Corporation together with other organisations for many years. During these experiments such process tasks as selection of the evaporation method, containment of molten material in the crucible and others, were solved, and the properties of the produced coatings were studied. So, it is shown [17] that the speed of production of coatings of pure silver (model material) at $g = 1\times10^{-5}$ g_0, where g_0 is gravity on the Earth surface, and at the pressure of residual atmosphere of $10^{-4} - 10^{-5}$ Pa, is several times higher than of their ground analogs. Stresses of the 1st kind which arise in Ag-coatings of 350 to 500 nm thickness, deposited on a substrate of D16 alloy on the ground, are –30 – +90 MPa; in similar coatings of 600 to 800 nm thickness produced in NEO, stresses of the 1st kind are practically absent. The difference in the level of macrostresses of the above coatings is illustrated in Figure 2. It can be seen that the cracks initiating from a cut made with a «guillotine» type cutter, have the form of cleavage in the coatings produced on the Earth (Figure 2, *a*) and the form of ductile fracture in the coatings produced in orbit (Figure 2, *b*).

Submicroporosity of Ag-coatings produced under microgravity conditions is smaller than of their ground analogs [18]. Distribution of submicropores by sizes in the samples produced under microgravity, is more uniform than in the samples produced on the ground. Similar results were also derived for Au- and Cu-coatings [19].

The influence of microgravity conditions on the process of evaporation of binary Ag–Cu alloys [20] is manifest in that the mass transfer mechanism in the molten material is in this case determined by diffusion, and not by convection, as on the Earth. Therefore, production of coatings of binary alloys without separation of their components, is really possible, as the parameters of the process can be selected so that the evaporation rate of the less volatile component of the alloy and the rate of its diffusion to the evaporation surface, become equal. Therefore, the coatings produced directly in orbit, can have a long service life before loss of their service properties, and before the operation for their restoration becomes necessary. The process of coating production under microgravity conditions will be more effective at the expense of lower porosity, and, hence an electrical conductivity which is higher and more uniformly distributed over the area, total purity and structural perfection, and, therefore, better ductility properties and lower internal stresses. One should also take into account the fact that under the NEO conditions, the rate of material evaporation increases by several times, and when the evaporation process proceeds from the molten state, it is possible to produce coatings from binary alloys with preservation of their stoichiometry.

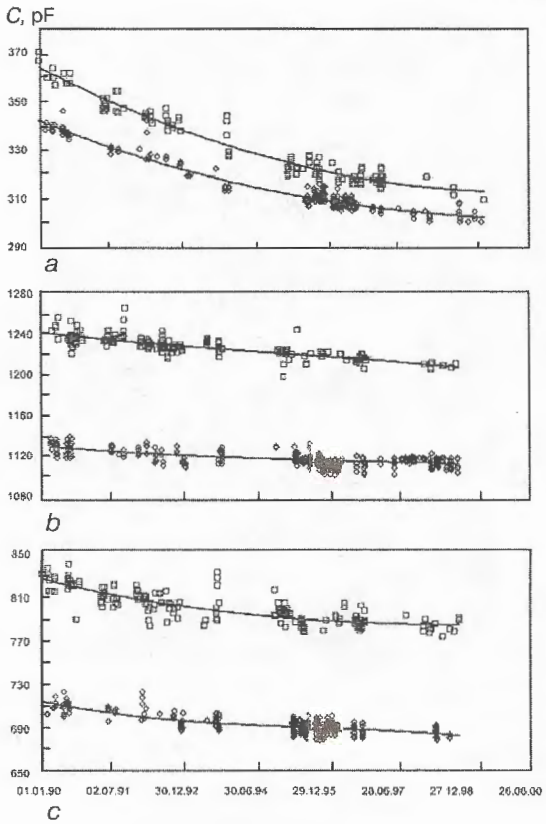

Figure 1. Dependence of capacitance on time for three types of samples: *a* — sample of PCM with ED-DADFM binder and glass cloth; *b* — sample of ED-DADFM; *c* — sample of ED-GMDA.

Analysis of the results of the performed studies confirmed the effectiveness of using the electron beam technology of coatings production directly in orbit and allowed development and manufacture on its base, of the appropriate equipment which was designed taking into account the problems related to work performance in the terrestrial orbit, namely containment of molten metal in the crucible, energy deficit (~ 500 W), absence of additional cooling, ensuring the operator safety, etc. An optimal combination of all the above factors has been achieved in the design whose block-diagram is shown in

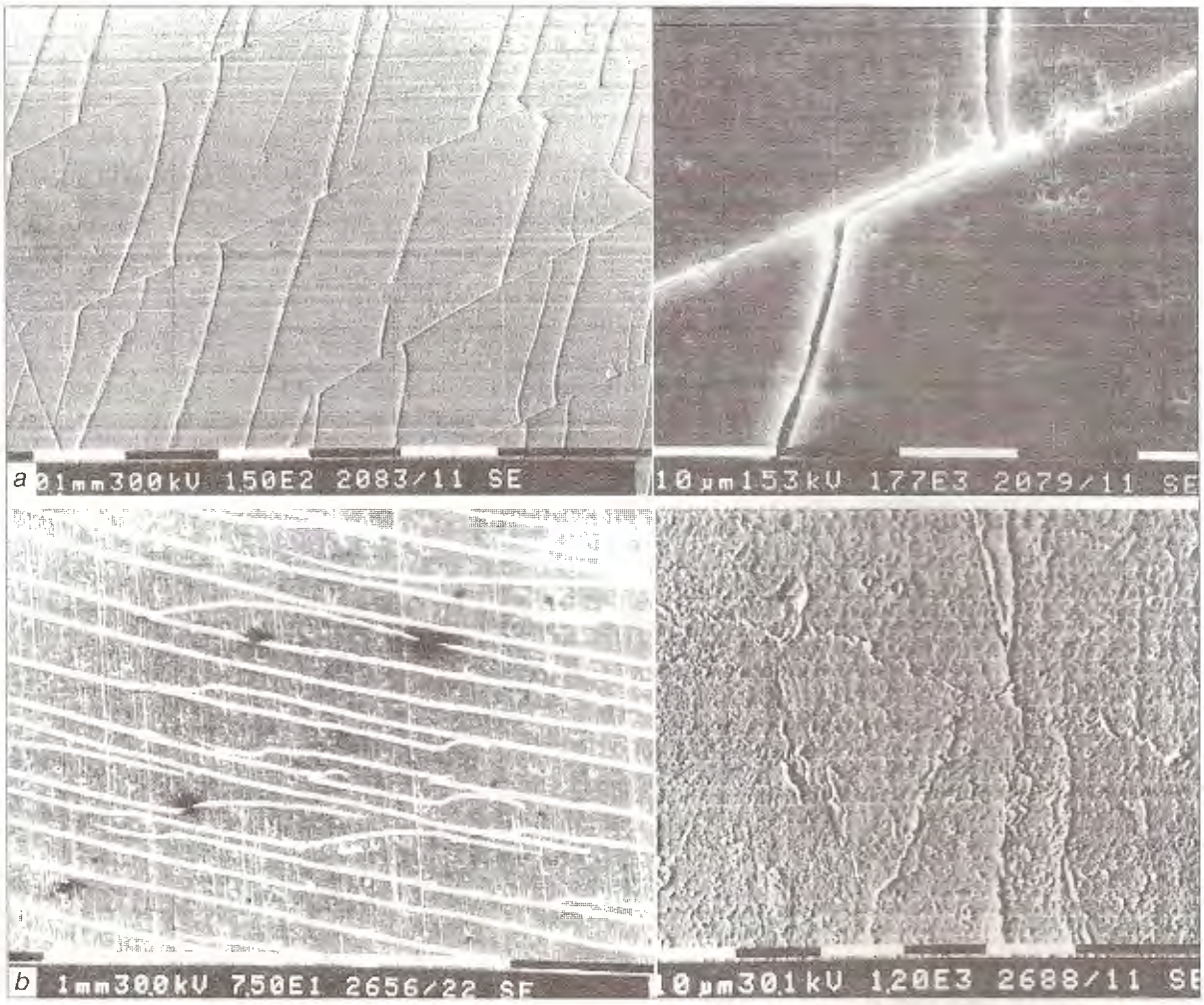

Figure 2. Nature of cracking in silver coatings produced: *a* — on the Earth; *b* — in NEO.

Figure 3. The hardware operation is based on indirect heating of the evaporation material by the electron beam. Extensive laboratory investigations led to creation of a highly effective device which allows heating of the materials being evaporated up to the temperature of 1500 °C. It was used as a basis for design and manufacture of stationary units for production of coatings under microgravity, namely «Isparitel'» and «Isparitel'-M» [21, 22]. A modification of one of them is shown in Figure 4. During 1979 to 1984 the units were tested with success in the «Salyut-6» and «Salyut-7» orbital stations. Testing of hardware for coating application was carried on in 1988 on board the orbital station «Mir» in «Yantar'» unit which permitted production of coatings on a polymer strip continuously moving with a speed of 20 to 40 m/h, which naturally, does not exclude the possibility, in principle, of the evaporation unit proper moving at the same speed. Successful flight tests showed that such hardware can be used as stationary equipment as part of the standard set of FV for periodical restoration of the service properties of reflective and other surfaces. In July 1984 the electron beam hand tool («VHT») was tested in raw space. It was used for performance of different process operations [23], including also coating application. As stated by cosmonauts S.E. Savitskaya and V.A. Dzhanibekov, the tool is extremely simple and convenient in operation.

In order to perform the concrete process tasks arising during FV service, especially in emergencies or in difficult-of-access places, PWI developed and manufactured the «Universal» hardware based on the electron beam hand tool. Two of the four tools which make it up, are designed for coating application. One of them is equipped with a detachable rotary attachment with four crucibles, which allows coatings from different materials to be deposited alternatively, or if required the stock of one material to be increased, if the surfaces being treated have considerable dimensions. The second tool allows evaporation of material fed in the form of wire, into the open crucible heated by the electron beam. Operational schematic and appearance of the tool are shown in Figure 5. Evaporation material in the form of 0.8 to 1.0 mm diameter wire is fed into the tungsten-cobalt crucible with the speed of up to 5 mm/s. Laboratory testing, as well as performance of manual operations by the operator in the space simulation test chamber showed that such tools allowed deposition of silver coatings under vacuum. Now, for aluminium evaporation, whose vapour pressure is by

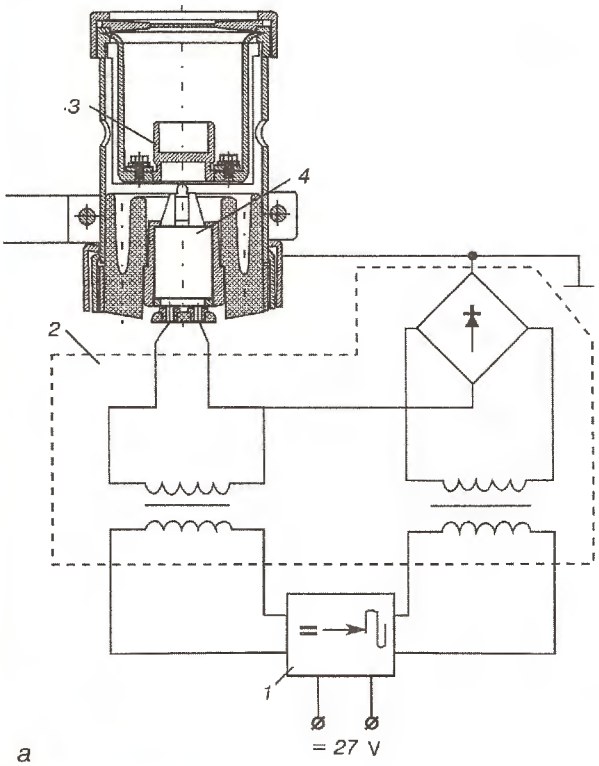

a

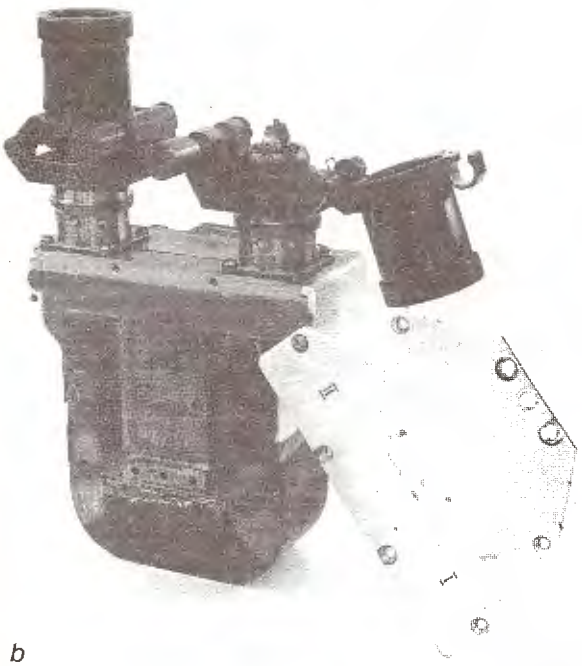

b

Figure 3. Schematics of heating of evaporation material and appearance of the device: *1* — secondary power source; *2* — high-voltage power source; *3* — evaporator; *4* — electron beam gun.

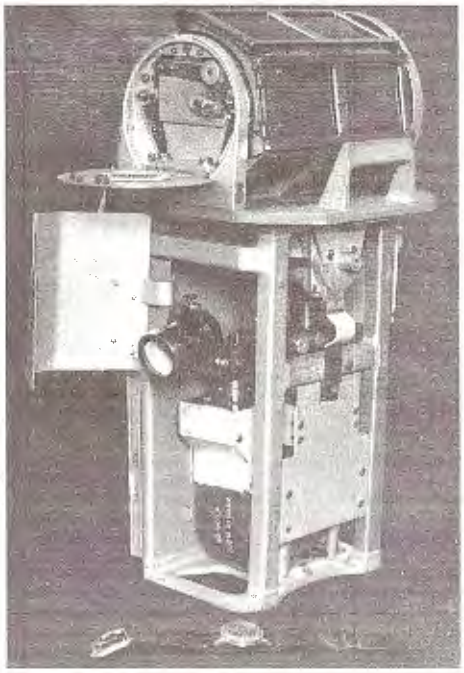

Figure 4. Stationary units for coating application under microgravity.

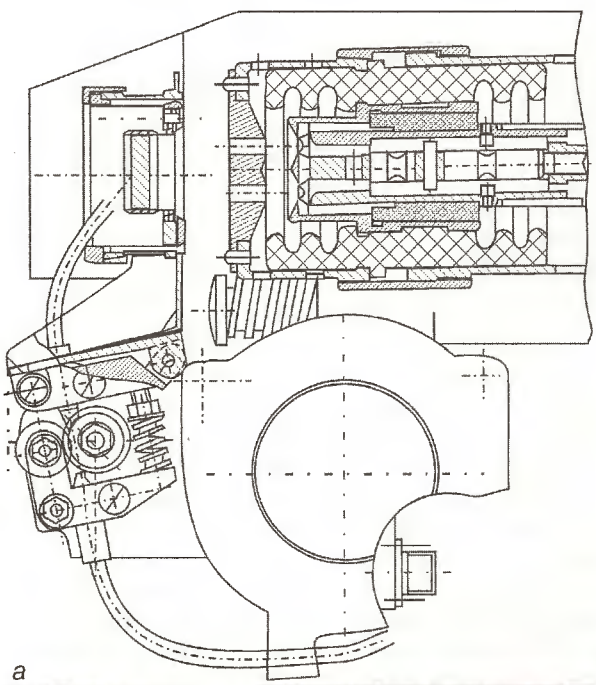

a

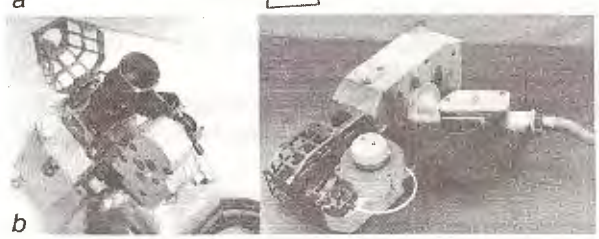

b

Figure 5. Diagram of the evaporator and appearance of the tool with evaporation material feed.

Specification	*«Isparitel»*		*«Isparitel-M»*		*«Yantar'»*		*VHT*		*«Universal»*	
Voltage, V	23 – 24		23 – 24		23 – 24		23 – 24		23 – 24	
Maximal current consumed, A	20		20		20		20		50	
Accelerating voltage, V	2		5		5		5		8	
Maximal electron beam current, mA	150		65		65		65		Up 120	
Number of EB guns for evaporation	2		2		2		1		1×2 tools	
Maximal continuous operation time of each gun, min	5		5		5		5		5	
Evaporation materials	Silver, copper, gold, copper-silver		Copper, copper-silver, antimony-bismuth		Copper, copper-silver, copper-manganese, magnesium fluoride		Silver		Silver, gold	
Kind of substrate	Flat		Flat		Polymer film		Flat		Flat	
Number of substrates in the set	12		12		10 m		2		Depending on modification	
Substrate dimensions, mm	80×60		80×60		70 mm width		240×170		Depending on modification	
Substrates preheating, °C	–		150 – 250		–		–		–	
Control	Manual		Program. from progam. panel		Program. from memory device		Manual		Manual	
Unit module	Work block	Contr. panel	Work block	Contr. panel	Work block	Contr. panel	Tech. block	Tool	Tech. block	Tool
Overall dimensions, mm	250× 250× 530	2900× 350× 400	2400× 260× 550	2950× 355× 405	240× 260× 530	295× 355× 405	500× 140× 220	300× 450× 300	470× 420× 372	330× 150× 300
Weight, kg	13.6	13.4	14.6	17.4	13.8	17.8	22.0	5.0	37.0	8.0

an order of magnitude lower than that of silver, it is necessary to significantly lower the wire feed rate or complement the tool with the device providing its dosed (impulse) feed. In case of aluminium evaporation, also because of its aggressiveness towards other materials, the crucible material much be carefully selected.

Solving these issues will allow the above tool to be used for aluminium coating deposition, this being a very urgent but yet unsolved problem in conducting the package of repair-welding operations.

Process characteristics of the hardware for coating deposition developed and tested in orbit, are given in the Table.

The versatility of the created hardware enables the following technologies to be implemented in orbit:

- scheduled maintenance to maintain the service properties of the reflective and other surfaces of FV using hardware which is part of the standard set of FV and which functions in the automatic mode;
- deposition of reflective coatings on large areas of solar-energy power systems using manipulators and remotely controlled robots;
- cleaning of the surface prior to coating deposition, not eliminating the possibility of the use [24] of other cleaning methods, namely ion-chemical or magnetic-abrasion;
- besides coating application, such processing operations as welding, brazing, cutting, heat-treatment, etc.;
- repair-restoration work during the operator's extra-vehicular activity (EVA), especially in difficult-of-access places.

CONCLUSIONS

1. Electron beam technology of materials evaporation under microgravity conditions has been developed, based on numerous laboratory and flight experiments on study of coating properties.

2. Correctness of the main design decisions in the hardware developed on the base of this technology, was confirmed by flight tests of the hardware for coating deposition in the «Salyut-6», «Salyut-7» and «Mir» orbital stations.

3. Results of analysis of coatings produced in flight experiments give rise to the conclusion that they can be applied with a quality not inferior to the ground conditions, during FV service in microgravity environment.

4. Prospects were shown for the use of the manufactured versatile equipment as stationary units in the set of standard equipment of FV for performance of the operations of restoration of coatings which had lost their service properties.

5. A manual modification device is envisaged in the versatile equipment, for performance of repair-restoration work in orbit in difficult-of-access places during the operator's EVA.

6. Different modifications of the developed versatile hardware can be used in the future for production of reflective surfaces in erection of mirrors of the solar-energy power systems and in construction of various settlements on the Moon or other planets.

REFERENCES

1. Lege, L.Zh., Veinsentein, J.T. (1987) Protection of space flying vehicles from the impact of atomic oxygen. *Aerospace engineering*, **2**, 7 – 11.
2. Atomic oxygen erosion on LDEF (1990) *Dep. Daily*, vol. 166, **30**.
3. Moag, C.R., Easbeek, van M., Deshapande, S. P., Stevenson, T. J. (1997) The contamination environment at the Mir Space Station as measured during the EUROMIR'95 mission. In: *7th Jut. Syst. Mater. Space Environ.* Toulouse, 16 – 20 June, 301 – 308. Noordwijk.
4. McKay, D.S., Barrett, R.A., Bernhard, R.P. (1987) Impact damage to solar Maximum satellite caused by micrometeorites and microparticle orbitae debris. *Meteoritics*, vol. 22, **4**, 453 – 456.
5. Nahra, H.K. (1988) Assessment of the effects of space debris and meteoroids environment on the space station solar array assembly. In: 20th IEEE Photovoltaic Spec. Conf. Las Vegas. Nev. Sept. 26 – 30. *Proc. Rec.*, vol. 2, **5**, 868 – 873. New York (N. Y.).
6. Coombs, C.K., Atkinson, D.R., Wagner, J.D., Allbrooks, M. (1992) Damage areals on LDEF aluminium panels: Preliminary results. In: *Lunar and Planet. Sci.* Vol. 23, Abstr. Pap. 23rd Conf., March 16 – 20. Pt. 1, **3**, 245 – 246. Houston (Tex) .
7. Morganti, F., Marchetti, M., Reibaldi, G. (1983) Effects of moisture and thermal ageing on structural stability of sandwich panels. *Acta astronaut*, 7, **11**, 489 – 508.
8. Zimcik, D.G., Maar, K.R. (1989) Consequences of atomic oxygen reactions with materials being on board the Space Shuttle in STS-41G mission. *Aerospace engineering*, **5**, 111 – 119.
9. McLean, P.D., Wiebe, W., Garton, A., Zimcik, D.G. (1985) Exposure of epoxy-amine plastics to the space environment. *Can. Aeronat. And Space J.*, vol. 31, **2**, 125 – 130. Translation in El *Astronautics and Rocket Dynamics*, **39**, 1986, 45 – 48.
10. Murad, E. (1989) Spacecraft interactions as influenced by thermochemical considerations. *J. Spacecraft and Rockets*, vol. 26, **3**, 145 – 150.
11. Sykes, G.F., Funk, J.G., Clemp, W.S. (1986) Assessment of space environment induced microdamage in toughened composite materials. In: *18th Int. SAMPE Techn. Conf.*, Seattle, Wash. Oct. 7 – 9, **18**, 520 – 534. Covina, Calif.
12. Banks, B.A., Mirtich, M.J., Rutledge, S.K., Nahra, H.K. (1985) Protection of solar array blankets from attack by low earth orbital atomic oxygen. In: *18th IEEE Photovoltaic Spec.*, Conf., Las Vegas, New., Oct.21 – 25, 381 – 386. New York, N.Y.
13. De Rooy, A. (1985) The degradation of metal surfaces by atomic oxygen. In: *3rd Eur. Symp. Spaceen.* Mater. Environ., Noordwijk, 1 – 4 Oct., 99 – 108. Paris.
14. Gulino, D.A., Egger, R.A., Banholzer, W.F. (1987) Oxidation — resistant reflective surfaces for solar dynamic power generation in near earth orbit. *J. Vac. Sci. and Technol*, vol. 4, **5**, 2737 – 2741.
15. Gulino, D.A. Space station solar concentrator materials research. *Adv. Mater. and Manuf. Process.*, 1988, vol. 3, **2**, 261 – 277.
16. Zimcik, D.G., Kavanagh, J. (1990) Material requirements for the space station mobile servicing system. *Can. Aeron. And Space.*, vol. 36, **1**, 11 – 17.
17. Paton, B.E., Lapchinskii, V.F., Mikhailovskaya, E.S., Gordonnaya, A.A., Sladkova, V.N., Shulym, V.F., Neznamova, L.O. (1997) Some features of formation of silver coatings under different gravity conditions. *Space Science and Technology*, vol. 3, **3/4**, 71 – 75.
18. Cheremskoi, P.G., Toptygin, A.L., Neznamova, L.O. (1990) Diagnostics of volumetric microinhomogeneities of coatings deposited under the conditions of orbital station flight. In: *Fundamental and applied problems of cosmonautics*: Abs. of Paper in Vth Royal Readings II Republ. Conf., 50 – 51. Kiev.
19. Palatnik, L.S., Toptygin, A.L., Cheremskoi, P.G., Savitskii, B.A., Arinkin, A.V., Nikitskii, V.P., Zhukov, G.V., Lapchinskii, V.F., Shulym, V.F. (1985) Comparative analysis of the structure of films of pure metals, deposited under the space and ground conditions. In: *Problems of space technology of metals*, 88 – 93. Kiev: Naukova Dumka.
20. Lukash, E.S., Shulym, V.F., Grigorenko, G.M., Smiyan, O.D., Neznamova, L.O. (1986) Investigation of the influence of gravity on composition of coatings from binary Ag–Cu alloys. In: *Problems of space technology of materials*, 22 – 28. Kiev: E.O. Paton Electric Welding Institute.
21. Zagrebelnii, A.A., Lapchinskii, V.F., Stesin, V.V., Shulym, V.F. *et al.* (1987) «Isparitel'». Author's Certificate **1485668**. Priority of October 12, 1987.
22. Zagrebelnii, A.A., Lukash, E.S., Nikitskii, V.P. *et al.* Development of the technique of deposition of thin-film coatings under flight conditions (1988) In: *Trans. of XXII Readings devoted to development of scientific inheritance and ideas of K.E. Tsiolkovskii.* Moscow, IMET AN SSSR, 134 – 138.
23. Nikitskii, V.P., Lapchinskii, V.F., Zagrebelnii, A.A. *et al.* (1985) Testing of manual electron beam tool in raw space. In: *Problems of Space Technology of Metals*, 7 – 15. Kiev: Naukova Dumka.
24. Grinkevich, A.D., Babaenko, P.L., Prisnyakov, V.F. (1986) Ionchemical cleaning of the portholes of a space vehicle. Idid, 28 – 33.

IMPROVEMENT OF ARC WELDING USING ELECTROMAGNETIC METHODS

S.V. PUSTOVOIT and G.I. LESKOV
The E.O. Paton Electric Welding Institute, NASU, Kyiv, Ukraine

ABSTRACT

It is established that the electromagnetic force, which acts to the front part of the pool, is sufficient for displacement of pool metal to a tail part and greatly influences the penetration depth.

Key words: *arc welding, demagnetization of billets, electromagnetic control.*

The wide application of arc methods in the manufacture of welded structures is a result of many-year investigations and improvement of all the operations and phenomena in this complicated technology [1].

The edge preparation, their fixation, arc guidance along the butts to be welded, welding conditions, pool maintenance in different spatial positions, weld formation, guarantee of its continuity and strength characteristics, elimination of electrode metal losses, increase in process efficiency due to increase in area of butts to be welded per unit of time continue to be the objects of investigations and improvements.

Forces, acting in the zone of welding under the earth conditions and defining many processes of formation of welds, as a rule are comparable with forces of an electromagnetic origin in high-current welding circuits. Therefore, a prime attention is paid to their study, control and rational use [2]. Demagnetization of edges to induction $B = (1-4)\times10^{-3}$ T [3] is the first requirement for the electromagnetic conditions of welding. Methods and equipment have been developed for its realization [4, 5], thus allowing the ferromagnetic billets of large sizes to be demagnetized for a short time.

The application of automatic demagnetizing in welding is challenging. Here, the executive device is located at the automatic welding machine nozzle [6].

Arc is the most flexible and low-inertia element of the welding circuit, therefore, its position even at the demagnetized edges greatly depends on the action of magnetic fields of the welding circuit. With changing the current supply with respect to the workpiece being welded [7] the arc position can vary both along and across the butt. Transverse arc shiftings which occur at non-symmetric «lateral» current supply are most unfavourable [8].

In routine of welding there are no systems of tracking of the arc itself and only the tracking of edges of the current-supplying nozzle is used. In axisymmetrical electromagnetic systems the natural magnetic fields maintain the arc column in axis and the used tracking is sufficient to perform the process of butt welding.

As the real electromagnetic systems in welding are not axisymmetric the arc deviations from the nozzle axis is inevitable. To eliminate them the transverse magnetic fields can be used [9] whose direction and induction depend on the deviation, length and value of the arc current. However, till now the systems of the automatic control of arc position at the edges welded have not yet been developed due to the lack of sensors, in spite of a well-developed theory and design of an executive element.

During welding the electromagnetic forces act on the easily-deforming liquid and gaseous areas of the circuit by changing their geometric shapes and motion in space and determine the depth of penetration and, consequently, the efficiency of welding and losses (spattering) of metal which forms the weld.

To analyze the ponderomotive forces, generated by natural magnetic fields and arc currents, the Figure 1 (t is the thickness of liquid metal interlayer) shows the elementary currents and electromagnetic forces df_1, df_2, df_3, acting on them. Their direction indicates the existence of radial and axial constituents. The integration of equations which determine these forces at some simplifying assumptions was carried out by some independent authors

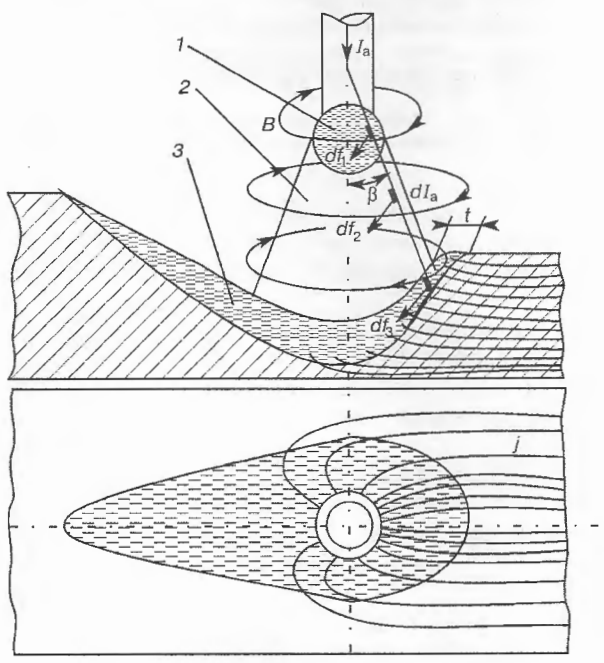

Figure 1. Zone of arc welding and its elements deformed by the magnetic field: *1* — drop of electrode metal; *2* — arc column; *3* — layer of liquid metal.

[10 – 13]. Similar results were obtained differing only by a negligible difference in numerical coefficients.

The axial force F_{10}, which detaches drop from the electrode, has a form

$$F_{10} = \frac{\mu_0 I_a^2}{4\pi} \ln \frac{r_c}{r_e}, \quad (1)$$

where r_c and r_e are the radii of column, adjacent to drop, and electrode; μ_0 is the magnetic constant.

Force F_{20}, which generates a gas-dynamic pressure against the pool, has a form

$$F_{20} = \frac{\mu_0 I_a^2}{4\pi} \ln \left[1 + \frac{l_a}{r_e} \operatorname{tg} \beta \right], \quad (2)$$

where l_a and β are the arc length and angle at the apex of its cone.

Force F_{30}, which acts on metal under the arc at axial symmetry, has a form

$$F_{30} = \frac{\mu_0 I_a^2}{4\pi} \ln \left(\frac{2.117\, b_w}{2 r_e} \right), \quad (3)$$

where b_w is the weld width.

Forces proportional to the square of arc current strength act on all three deforming areas, that was proved experimentally many times. Thus, in welding with electrode Sv-08A (d = 1.6 mm) the drop from electrode can be detached by an electromagnetic force which exceeds the force of the surface tension, i.e. at

$$F_s = \sigma 2\pi r_e \le F_{10},$$

where σ is the surface tension of steel.

At σ = 1.84 N/m and $\ln \frac{r_c}{r_e} = 0.6$, where $\frac{r_c}{r_e} = 1.4$, the current I_a = 530 A is required to detach the drop without allowance for the gravity force. Therefore, to control the drop transfer to the pool, even in an overhead position, a pulsed-arc consumable electrode welding, firstly developed at the Paton Institute in 1963, is used.

According to formula (2) the force which causes the shifting of column plasma to the side of pool and its deepening, is also proportional to the square of current strength, however, it greatly depends on the angle β at the apex of a conical column (Figure 1). With decrease in electrode diameter the column conicity is increased. Therefore, such arcs cause the deeper penetration of workpieces to be welded.

At pulsed currents with frequencies used for control of the electrode metal transfer (hundreds of cycles), the changes in penetration depth due to a significant heat and mechanical inertia of the pool is improbable.

During welding the electromagnetic processes in a head part of the pool are most far from the axial symmetry, therefore their analysis was made taking into account the data about current I distribution in it [8], (Figure 1, top view) . In this part of the pool up to 70 % of arc current is passing. Let us assume its distribution across the thickness of metal being welded and width, occupied by a column base on the pool, to be uniform. Thickness t of a molten part of the pool ahead of the arc column will be evaluated from coloured photos of the welding zone, given in work [14] using a quartz glass. At the rates of open-arc welding (v_w = 10 m/h) in shielded gases 80 % Ar + 20 % CO the thickness t is approx. 6.5 mm, while at v_w = 30 m/h it is decreased to 2.5 mm. Force, acting to this part of the pool, has a form

$$F_{30} = \mu_0 H I t \sin (H, l) .$$

In the upper part of this zone sin (H, l) is close to 1, while in the lower part (at 10 mm metal thickness) it can be assumed close to 0.7 (Figure 1). From evaluating the force acting to the molten part of the pool ahead of the arc by an average value sin (H, l) = 0.85 at arc current I_a = 300 A, we shall obtain

$$F_{30} = 0{,}1\, \mu_0 \frac{I_a^2}{r} t,$$

where r is the distance from the column axis to the middle of a liquid layer; $H = I_a / 2\pi r$ and $l = 0.71_a$.

At current 300 A, t = 0.25 and r = 0.4 cm we shall obtain $F_{30} = 6.85 \times 10^{-3}$ H, that generates the following pressure to the pool of an area S = 7.5×10^{-6} m^2:

$$p = \frac{F_{30}}{S} = \frac{6.85 \times 10^{-3}}{7.5 \times 10^{-6}} \approx 0.9 \times 10^3 \text{ Pa}.$$

At density of a liquid steel $\rho = 7.6 \times 10^3$ kg/m^3 the pressure in the field of a pool gravity can be equalized by its height in a tail part, equal to 1.2 cm.

The given estimated calculation shows that the electromagnetic force acting to the front part of the pool under the real conditions of welding, is sufficient for metal displacement to a tail part and it should be regarded as a basic force which causes such movement. These calculations are correlated with experimental data [15], thus indicating the intensive motion of the metal and increase in a penetration depth during welding with a pulsed current of 0.5 Hz frequency.

In imposition of external controllable magnetic fields on the zone of welding the additional forces are occurred in it which influence many processes. The fields, whose basic constituent of induction coincides with an arc axis (longitudinal magnetic fields — LMFs), have different effects on liquid and gaseous parts of the welding circuit. When a radial constituent of the current strength is available in a drop, the electromagnetic forces in it cause its rotation around the electrode axis, flattening under the action of centrifugal forces, increase in heat flow from a column into an electrode and rate of its melting [16, 17] by 40 %. However, these same forces cause the spattering of drops. Therefore, the effect of these forces is rational only in submerged arc welding.

The action of LMF on the column greatly depends on its induction B and arc current value I_a: at $B \le 25 \times 10^{-3}$ T and current value from 100 to 300 A the arc column, not almost changing its shape, is rotated around the electrode, leaving a trace of a deionizing plasma [18]; at $B \ge 30 \times 10^{-3}$ T the

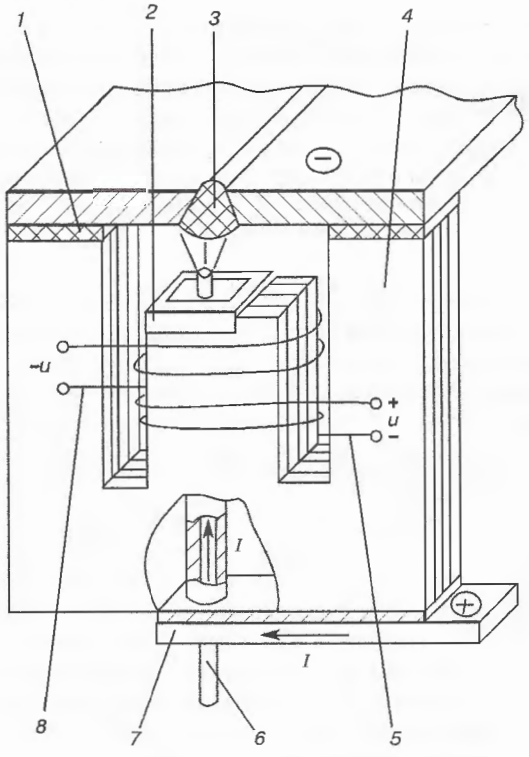

Figure 2. Electrical system for control of overhead welding (designations in text).

column acquires a symmetric conical shape with an apex in a cathode spot [19]. The pressure inside the cone becomes lower than the atmospheric pressure [20]. This arc feature in LMF is used in welding of thin workpieces without any backings.

By decreasing two-polar diffusion of charged particles of the column to its periphery, the LMFs constrict the arc, thus leading to the increase in its penetrability in welding of non-ferromagnetic materials approximately by 2 times [21]. In welding of ferromagnetic materials this effect is not observed, as LMFs do not penetrate the arc, being shunted outside it with hard particles of these materials.

Constant LMF acting on pool with a non-symmetric passing of current in it, generates the forces which move the liquid metal to one of edges of the workpieces being welded and cause an undercut in another edge. Therefore, in works for improvement of conditions of pool stirring and its solidification without formation of large dendrites the alternating LMFs are used [18].

The transverse magnetic fields (TMFs) can be used not only as executive elements of the butt arc tracking systems but also for arc rotation with a preset eccentricity around the electrode axis. For this purpose the rotating TMFs should be used in systems which are similar to asynchronous three-phase electric motors. This a rather low-powerful «arc motor» can create the same conditions of motion, stirring and solidification of the pool, as in rotation of the arc nozzle with an electrode using a special mechanical device [22].

Combined external magnetic fields in combination with welding currents create electromagnetic forces which allow one of the most important problems of the technology of welding, i. e. the overhead welding, to be solved.

Sketch of one of the devices to maintain the pool in an overhead position and to provide the electrode metal drop transfer to it is given in Figure 2 [23]. The magnetic field in the zone of welding *3* is generated by windings *8* and *5* at the middle core of Ш-shaped magnetic conduit *4*. It is isolated galvanically from the workpiece to be welded with gaskets *1*. The filler metal enters the edge groove during melting of the wire electrode *6*.

Winding *8* is supplied with an alternating current of 500 Hz frequency, while the winding *5* is supplied with a direct current. The favourable conditions of weld formation are provided in creation of a gradient of inductance of the alternating magnetic field in the pool zone which is attained with the help of a shading coil *2*. The constant constituent of LMF, which is generated by winding *5*, rotates the column plasma, thus increasing its kinetic energy and arc stability in the space.

The interaction of the column magnetic field with the current in the workpiece, the main part of which is passing ahead of the arc, generates a force directed to its depth. In the described device this effect is intensified in the whole length of the pool by an action of a transverse constituent of a direct magnetic field $B = (30 - 36) \times 10^{-3}$ T, thus keeping it in an overhead position.

The alternating magnetic field induces currents in the pool and drop, which are opposite to the current in winding *8*. Therefore, the forces appear between them which detach the drop from the electrode and maintain the pool. This effect is observed at an amplitude of the magnetic induction $B_{max} = 150 \times 10^{-3}$ T.

CONCLUSIONS

In the zone of welding with high-current arcs using time-constant or pulsed conditions the forces are generated under the action of natural or external controllable magnetic fields. These forces cause the motion of parts which are deformed by them: drop, plasma of column and pool. In the majority of cases they are proportional to a square of the arc current value.

Rational formation of these forces and their control can decrease to minimum the metal spattering, increase the depth of penetration of workpieces and, consequently, the efficiency of the welding process, perform welding in any spatial position, improve the pool stirring, distribution of alloying elements in it, gas evolution and metal solidification.

Many solutions were tested in experiments and some of them were implemented in industry. However, to use widely the electromagnetic methods for improving the arc welding, it is necessary to study the effect of rotating transverse magnetic fields on arc and pool, pulsed action of electromagnetic forces on the pool taking into account its mass and frequency of free oscillations, to create unified devices for formation of external magnetic fields,

sources for arc supply with pulses of low-frequency (0.5 – 5.0 Hz) current, sensors of pool oscillation and control of processes of its solidification, microprocessing systems for the welding technology control.

REFERENCES

1. Paton, B.E. (1999) Problems of welding at the transition of centuries. *Avtomaticheskaja Svarka*, **1**, 4 – 14.
2. Paton, B.E., Lebedev, V.K. (1964) Magnetohydrodynamic phenomena in electric welding and their use. In: *New problems of welding engineering*, 332 – 336. Kiev: Tekhnika.
3. Volokhov, S.A., Dobrodeev, L.N., Bezlyudko, G.Ya. *et al.* (1998) Technology of demagnetizing large-diameter pipes of main pipelines. *Welder*, **2**, 5 – 6.
4. Bessonov, L.A. (1967) *Theoretical fundamentals of electrical engineering*. Moscow:Vysshaya shkola.
5. Leskov, G.I., Protosej, N.E., Novikov, D.Yu. (1987) Conditions of demagnetizing of workpieces before welding and methods of their assurance. *Avtomaticheskaja Svarka*, **7**, 40 – 45.
6. Shchukin, V.A. (1978) Automated elimination of magnetic arc blow. *Tekhnologiya Sudostroyeniya*, **3**, 21 – 23.
7. Khrenov, K.K. (1949) *Electrical welding arc*. Moscow: Mashgiz.
8. Raichuk, Yu.I. (1967) Distribution of current in plate during arc welding. *Avtomaticheskaja Svarka*, **4**, 19 – 22.
9. Kovalyov, I.M. (1965) Deviation of welding arc in transverse magnetic field. *Svarochnoye Proizvodstvo*, **10**, 4 – 6.
10. Zalessky, A.M. (1974) *Fundamentals of theory of electric devices*. Moscow: Vysshaya Shkola.
11. Paton, B.E., Potapievsky, A.G., Podola, N.V. (1964) Pulsed-arc consumable electrode welding with a programmed control of the process. *Avtomaticheskaja Svarka*, **1**, 1 – 7.
12. Leskov, G.I. (1970) *Electric welding arc*. Moscow: Mashinostroyeniye.
13. Lebedev, V.K., Pentegov, I.V. (1981) Forced action of welding arc. *Avtomaticheskaja Svarka*, **1**, 7 – 15.
14. Zemlevsky, L.A, Leskov, G.I. (1978) Study of process of metal fusion in immersed arc welding. Ibid, **3**, 16 – 17.
15. Caloun, K., Varga, T. (1990) On pulsed submerged arc (SA) welding (Montreal, 2 – 12 July,1990). *IIW commis. XII-Montreal*, **4**, 439 – 449.
16. Zernov, A.V. (1972) Study of effect of induced magnetic fields on the process of electric submerged arc welding. In: *Abstract from thesis*. Lvov.
17. Boldyrev, A.M.,Birzhev, V.A., Chernykh, A.V. (1991) Peculiarities of electrode metal melting during welding in external longitudinal magnetic field. *Svarochnoye Proizvodstvo*, **5**, 28 – 30.
18. Shelenkov, G.M., Chernysh, V.P., Gurevich, S.M. *et al.* (1977) Peculiarities of weld formation in arc welding Ti using EMF. Ibid, **3**, 24 – 25.
19. Gvozdetsky, V.S., Mechev, V.S. (1963) Study of magnetically impelled dc welding arc (flat and conical). *Avtomaticheskaja Svarka*, **12**, 1 – 6.
20. Levakov, V.S., Lyubavsky, K.V. (1965) Effect of longitudinal magnetic field on electric welding arc, *Svarochnoye Proizvodstvo*, **10**, 9 – 12.
21. Birzhev, V.A. (1997) Theoretical and technological bases of improving efficiency of arc welding and surfacing in external axial magnetic field. In: *Abstract of thesis*. Lipetsk.
22. Gordonny, V.G., Gaivoronsky, A.A., Sarzhevsky, V.A. *et al.* (1993) Effect of high-speed rotation of electrode on structure and properties of high-strength steel welded joints. *Avtomaticheskaja Svarka*, **5**, 28 – 31.
23. Nesmashny, V.A. (1973) Formation of overhead welds with the help of magnetic fields in arc welding. *Svarochnoye Proizvodstvo*, **6**, 23 – 24.

TECHNOLOGICAL CAPABILITIES OF THE PROCESS OF DOUBEL-SIDED WELDING OF ALUMINIUM ALLOYS

A.Ya. ISHCHENKO, N.M. VOROPAI, V.P. BUDNIK and **V.A. MISHENKOV**
The E.O. Paton Electric Welding Institute, NASU, Kyiv, Ukraine

ABSTRACT

Features of TIG-welding of aluminium alloys by arcs facing each other were studied. Compared to the regular processes which envisage weld formation from one side, an essential increase of metal penetration has been achieved with the weld width comparable with the base metal thickness and a favourable appearance of the weld from both sides of the joint.

Key words: *arc welding, nonconsumable electrode, aluminium alloys, opposite arcs, penetrability.*

Nonconsumable electrode AC argon-arc welding became the most widely accepted process in fabrication of metal structures from aluminium alloys. This process, providing a high quality of welded joints, is characterised by a comparatively low penetrability of the arc. Improvement of the weld metal quality and deeper penetration can be achieved using asymmetrical current with prevalence of the straight polarity component [1]. An even greater effect is achieved in DCSP welding in helium [2]. These processes allow the penetration depth to be increased by 1.5 to 2.5 times compared to the regular AC argon-arc welding [3, 4].

Further expansion of the technological capabilities of arc welding can be achieved by applying the process schematic which envisages the arcs position opposite each other [5]. AC plasma arc was used by the authors of the above work as one of the heat sources. Realisation of this process involves certain technical and technological difficulties.

In order to study the process capability of double-sided welding, we developed a laboratory facility whose schematic is shown in Figure 1. The facility consists of mobile table *2* which carries the plate to be welded, drive *1* of table displacement, rotary cantilever *3* with upper torch *4*. Lower torch *5* is fastened on extendible rod *6* which is mounted on support *7* mobile in three directions normal to each other. Coaxiality of the electrodes and the required arc gap are achieved by adjustment of the position of support *7*.

Investigations were conducted by connecting the torches to different poles of a DC source (Figure 2). In this case the welding circuit was opened through a sample electrically insulated from the current source. AMg5 aluminium-magnesium alloy plates of 10 mm thickness were used as the latter. With this connection diagram, one of the arcs ran in the straight polarity mode and the other in the reverse polarity mode. A 4 mm diameter electrode from tungsten of EVI-1 grade with yttrium was used in the first case (with helium or argon shielding) and in the second case 10 mm electrode from tungsten of EVCh grade (with argon shielding). The speed of the sample displacement was 10 m/h. Welding was performed without filler wire.

In order to study the effect of the appropriate polarity on weld formation, the electrodes were connected by different schematics. First welding with the straight polarity arc located on top of the sample was tested using helium as the shielding gas. The reverse polarity arc was placed in the overhead position. Complete penetration of a 10 mm thick plate was achieved with the welding current of 120 A (Figure 3, *a*). The total arc voltage here was equal to 21 to 22 V. It should be noted that the reverse

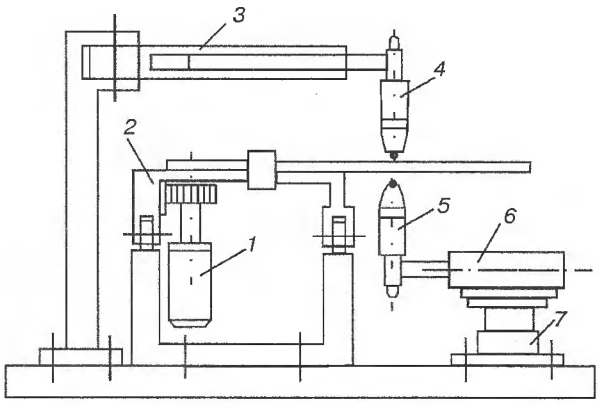

Figure 1. Schematic of a set up for double-sided welding (for designations see the text).

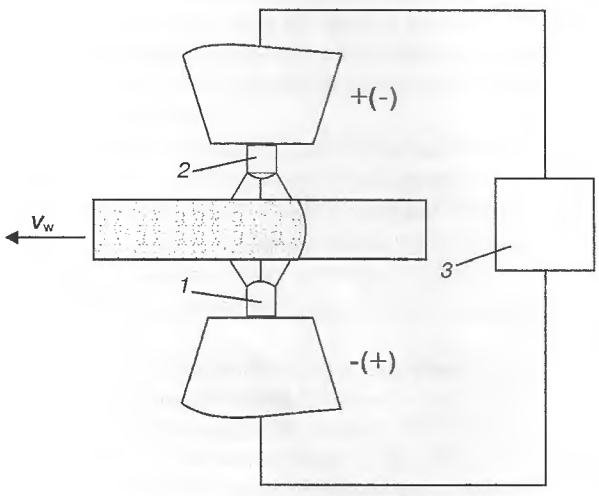

Figure 2. Schematic of connection of the torches: *1*, *2* — lower and upper electrode, respectively; *3* — power source.

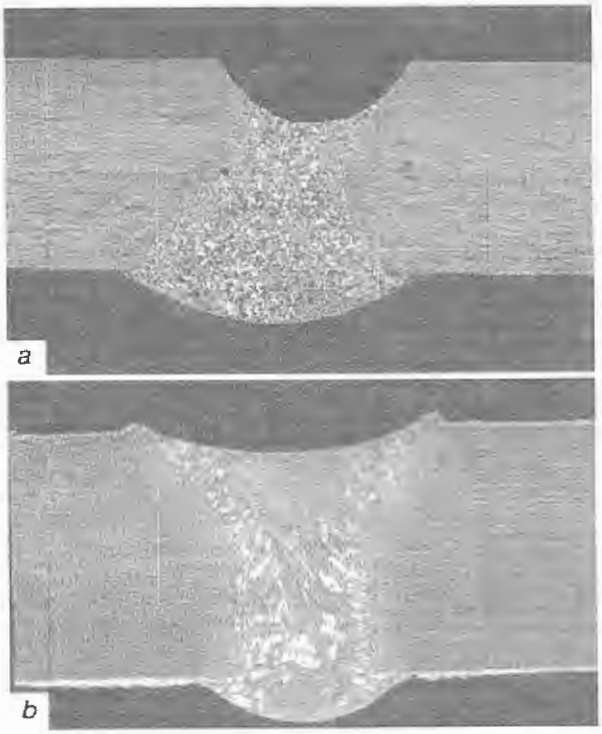

Figure 3. Transverse macrosections of the weld (×4) (reduced by 0.75): *a* — straight polarity arc located on top, reverse polarity arc located below; *b* — straight polarity arc located below, reverse polarity arc located on top.

polarity arc, compared to the straight polarity arc (at equal currents) promotes formation of a much larger volume of the molten metal, this in its turn resulting in excessive sagging of the weld pool. Nonetheless, in this case, the total cross-sectional area of the weld is smaller than in welding of metal of the same thickness in one pass at alternating or even at straight polarity direct current.

In order to eliminate excessive sagging of the weld metal under the impact of the reverse polarity arc located in the overhead position, an experiment with this arc location on top of the plate was conducted in the next stage. Such an arrangement of the arcs provided the optimal ratio of heat input by the arcs from both sides of the base metal and led to a more favourable weld shape (Figure 3, *b*). Stable penetration of the metal was achieved at the welding current of 160 A and total arc voltage of 23 to 24 V.

The appearance of the welds in the lower and upper part of the joint in welding at both the straight and reverse polarity, is characterised by uniform formation and absence of external defects. An example of the weld appearance from the lower side of the sample is shown in Figure 4. The appearance of the weld from the upper side is similar. When complete penetration was achieved, the weld width was by 1.5 to 2 times smaller than the thickness of the metal being welded. Cleaning of the surface from oxides is ensured from both sides of the joint. In the reverse polarity arc surface cleaning is provided by intensive cathode sputtering, and in the straight polarity arc due to high-temperature disintegration.

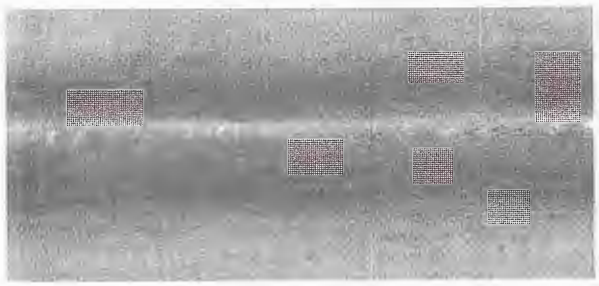

Figure 4. Weld appearance in overhead welding from the side of the straight polarity arc.

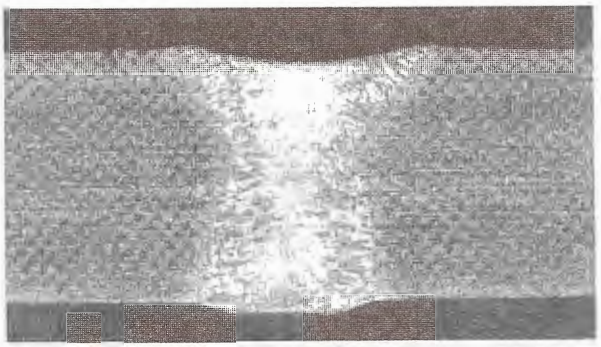

Figure 5. Transverse macrosection of the weld with straight polarity arc located below and reverse polarity arc located on top, shielding gas is argon (×4) (reduced by 0.80).

Welding with argon used for shielding the straight and the reverse polarity arcs was tried out. The straight polarity arc was located below the sample. This experiment showed that for common pool formation and achievement of complete penetration, the welding current should be set at 140 A. In this case, a favourable shape of penetration is found with a small ratio of the weld width to the base metal thickness (Figure 5). The weld metal does not contain defects of the type of pores or oxide inclusions. The main disadvantage of such a process schematic, is poor cleaning of the weld surface from oxides from the side of the straight polarity arc. This is related to relatively low energy parameters of the arc when argon is used as the shielding gas.

It is of interest to study the separate influence of the straight and the reverse polarity arcs on the shape of base metal penetration. For this purpose plates melting through was performed alternatively by straight polarity arc from below and by reverse polarity arc from top. Welding was conducted at welding current close in value to those used

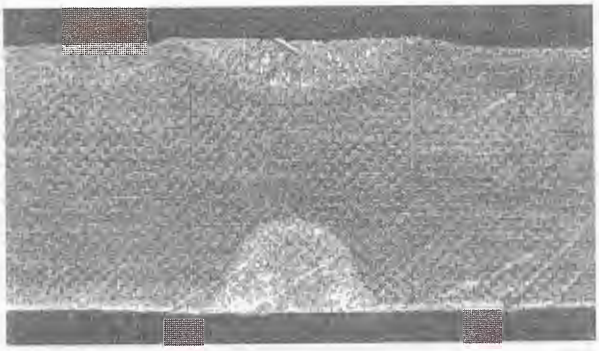

Figure 6. Transverse macrosection of weld in welding by independent arcs (×4) (reduced by 0.80): top — by reverse polarity current; below — by straight polarity current; welding current of 180 A.

earlier. After making the weld by the reverse polarity upper arc, welding was performed by straight polarity arc from below. The welding current was equal to 180 A, accordingly. The derived results are shown in Figure 6. One can see in the macrosection that welding with independent arcs cannot provide complete penetration in such modes. Note that in single-arc welding of 10 mm thick metal at the same speed by alternating current in argon the welding current is 415 A, and in straight polarity welding in helium 325 A.

Thus, compared to the conventional processes of nonconsumable-electrode arc welding, double- sided welding allows reduction by 2 to 3 times of the welding current required for complete penetration of the base metal. In this case, a favourable weld shape is achieved with a small ratio of its with to the penetration depth. The welding heat input is essentially reduced and the heat-affected zone becomes smaller, accordingly, and improvement of welded joint mechanical properties is also possible. Further investigation of the described double-sided welding should be conducted towards the use of alternating current for powering the arcs, including asymmetrical current, provision of filler wire feed into the melting zone, and use of metal electrode in combination with the nonconsumable electrode. It is rational to expand the range and thicknesses of the metals and alloys being welded, as well as study the technological capabilities of this process in terms of all-position welding of the joints.

REFERENCTS

1. Rabkin, D.M., Voropai, N.M., Mishenkov, V.A. (1978) Energy characteristics of the process of welding at asymmetrical current of different polarity. *Avtomaticheskaya Svarka*, **4**, 5 – 10.
2. Rabkin, D.M., Saenko, M.I., Steblovskii B.A. (1976) Properties of welded joints of 1201 alloy made at direct and alternating current. Ibid, **9**, 21 – 24.
3. Budnik, V.P., Steblovskii, B.A., Buts'ko, M.G., Krylov, V.G. (1982) Penetrability of direct and alternating current arc. Ibid, **8**, 68 – 70.
4. Ishchenko, A.Ya., Poklyatskii, A.G., Yavorskaya, M.R. (1990) Influence of square-wave asymmetrical current of different polarity on weld parameters in argon-arc welding of AMg6 alloy. Ibid, **1**, 26 – 28.
5. Zhnag, Y.M., Zhang, S.B. (1998) Double-sided arc welding increases weld joint penetration. *Welding J.*, **6**, 57 – 61.

PLASMA SURGICAL SYSTEM «PLASMAMED»

B.E. PATON[1], V.S. GVOZDETSKY[1], V.I. DRANOVSKY[2], V.L. DZHEPPA[2], Yu.S. FURMANOV[3] and A.A. LYASHENKO[3]
[1]The E.O. Paton Electric Welding Institute, NASU, Kyiv, Ukraine
[2]State Design Bureau «Yuzhnoye», Dneptropetrovsk, Ukraine
[3]Institute for Experimental and Clinical Surgery, MASU, Kyiv, Ukraine

ABSTRACT

Decribed are the basic results of the development made by the State Design Bureau «Yuzhnoye» in collaboration with the E.O. Paton Electric Welding Institute and the Institute for Experimental and Clinical Surgery. The development included the plasma surgical system «Plasmamed» intended for surgical operations, such as dissection of biological tissues (destruction) and arrest of bleeding on injured surfaces (coagulation).

Key words: plasma surgery, plasmatron, hemostasis, destruction, coagulaton.

In modern surgery the effect of a high-temperature (approximately 10000 °C) plasma jet on biological tissues is used for their dissection, arrest of bleeding (hemostasis) and removal of tumors (neoplasms, abscesses, etc.). Fields of application of plasma surgical devices are very wide, they include general surgery, gynecology, oncology, urology, neurosurgery, orthopedics, traumatology and veterinary.

The basic positive properties of plasma surgery include bacterial action, insignificant injury to biological tissues and reliable hemostasis, especially in operations on parenchymal organs. Depending upon the plasma jet parameters, the operations may be done either for dissection of tissues or for coagulation of the injured surfaces.

Plasma surgery has been developed and applied for about three decades. In the 1960s — early in the 1970s the attempts were made in the USA to develop a plasma scalpel of the «Mark» type. However, the plasmatron designed for using a mixture of helium and argon for the operations turned out to be unreliable. Besides, the plasma jet with a thermal power of up to 70 W and temperature of about 6700 °C was unstable and of low intensity.

Several plasma surgical systems were developed and found application in practical medicine in the former Soviet Union. These were the SUPR-M system (helium, manufactured by the Smolensk Aircraft Engineering Plant) and the «Fakel-01» system (argon, developed by the N.E. Bauman Technical University in Moscow and manufactured by the Design Bureau «Fakel» in the Kaliningrad district). In these systems the plasma temperature amounted to 10000 °C. Then followed the «Fakel-11» (argon) and «Gemoplaz-VP» (air) systems intended for field applications. Also known is the UMPR-20 plasma system developed by the Leningrad Polytechnical Institute in collaboration with the Military Medical Academy. The latter is available in limited amounts, as it has never been produced commercially.

As it is said in promotional brochures, the plasma surgical tool «Plasmsurge-101» manufactured by the «Nikval International AB» (Sweden) is currently put through tests, showing itself to advantage, in Russia. This tool was developed with participation of specialists from the N.E. Bauman Technical University in Moscow.

Despite the certain success, until now the plasmadynamic method has not yet found the everyday use in medical practice, and it is our opinion that this is attributable to an insufficient perfection of the existing systems in service, their relatively high costs (retail price is $ 25000) and the absence of a systematic approach in practical application of the plasma method.

The State Design Bureau «Yuzhnoye» in collaboration with the E.O. Paton Electric Welding Institute and the Institute for Experimental and Clinical Surgery developed under the conversion project the plasma surgical system (PSS) called «Plasmamed», which was approved by the Scientific-and-Technical Centre in Ukraine.

The system (Figure 1) consists of a service unit with two manipulators, a power cable and a remote foot pedal. The service unit houses a storage and feed system for the plasma gas (argon), module for water cooling of plasmatrons, as well as a transformation and control unit. The latter includes a control and indication block, transformation and ignition block, control panel and a cable system.

Argon can be fed either from two built-in bottles with a capacity of 5 l each or from an external source. The water cooling module is made as a circular loop with radiators to remove heat and release it into the surrounding atmosphere. Plasmatrons can be turned on from the panel or from the remote food pedal. «Plasmamed» is equipped with the plasmatron service life register.

In the case of malfunction, the plasmatron is turned off and one of the following messages is delivered to the control and indication panel: «No Water» in the destruction plasmatron, «No Water» in the coagulation plasmatron, «No Gas», «Short Circuit» in the electric power circuit of the plasmatrons or «No Earth» at break in the earth wire circuit.

The characteristic feature of «Plasmamed» is that its transformation and control unit can provide operation of both three-electrode plasmatron (with an intermediate starting electrode) and that made with two-electrodes, and switching from one mode to the other is done automatically by connecting this or that type of the plasmatron. Release of the heat removed from the plasmatrons into the atmosphere exclude any limitation on duty cycle of the plasmatrons, which can be caused by overheating of the cooling liquid.

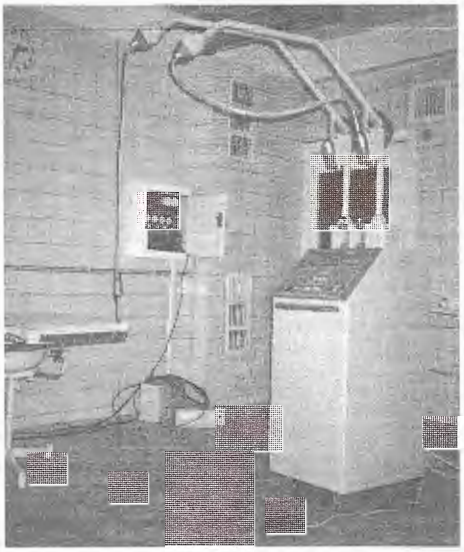

Figure 1. Appearance of the PSS «Plasmamed».

Specifications of the PSS «Plasmamed»

Plasma gas	argon
Quantity of plasmatrons	2
Thermal power of the plasma jet, W	70 – 350
Arc discharge current, A	6 – 25
Arc discharge voltage, V	25 – 40
Number of power modes of plasmatrons	3
Current	single-phase alternating
Voltage, V	220±22
Frequency, Hz	50 – 60
Power consumption, kW	1.6
Mass, kg	132
Dimensions, mm	460×560×2100

During the period from September 2 till October 12, 1999, «Plasmamed» was being subjected to medical-biological tests at the Department of Experimental Surgery of the Institute for Experimental and Clinical Surgery of the Medical Academy of Sciences of Ukraine (Figure 2). The tests were done on animals (2 white rats, 15 rabbits and 2 pigs). The tests included the use of «Plasmamed» for such surgical operations as dissection of aponeurosis in medium laparotomy (dissection of abdominal wall),

Figure 2. Medical-biological tests of the PSS «Plasmamed» at the Institute for Experimental and Clinical Surgery of the Medical Academy of Sciences of Ukraine.

partial resection of spleen with resection of mesentery in its upper pole, as well as liver. All the operations were done with anesthesia under sterile conditions. Euthanasia of the animals was done 3, 7, 10 and 21 days after the operation by overdosing narkotic materials. Preparations were described and photographed, samples of the tissues were taken to check histology and a video film was made.

After the operations all the animals easily recovered, and no deviations in their behaviour or in general health condition were registered. Histology of the tissues taken from the zones treated by the plasma jet showed that after 21 days no coagulation crust was seen and that the necrotized tissues were surrounded by a capsule formed by the granular tissues. The low glycogen content of hepatocytes was noted only around the capsule. Parenchyma with some indications of slight inflammatory changes (moderate lymphocytic infiltration of stroma) was registered in the other zones. In all the cases no neutrophilic infiltration was seen.

During the tests, «Plasmamed» caused no problems, except for the need to replace a fuse, which was done quickly in course of the operation. Comments of the medical staff as to possible improvements in the system design will be taken into account in further upgrading work.

ADVANCED MEANS OF TRAPPING AND NEUTRALIZING TOXIC GASEOUS SUBSTANCES IN WELDING PRODUCTION

A.A. ENNAN and T.L. RAKITSKAYA
Physical-Chemical Institute for Environment and Human Protection of the Ministry of Education and NASU, Odessa, Ukraine

ABSTRACT

The feasibility of trapping welding aerosol (WA) to prevent the respiratory organs of welders is considered conceptually. The peculiarities of neutralizing different types of WA are analyzed. The information about the new multicomponent catalysts for neutralizing WA and technology of their production are given.

Key words: *welding, welding aerosols, gas constituent, air purification, sorbents, ionites, catalysts, respirators, filter-ventilation equipment.*

The interests of the present ecology are spread not only to the field of environment protection, but also of the internal medium of human being. In this respect, the welding production is an object of comprehensive investigations whose results are valuable in practice if to interrelate ecological, sanitary-hygienic, physical-chemical, sanitary-technical, ergonomic and economic aspects of the problem.

The main harmful factors of the welding production are an emission of a welding aerosol (WA), ultraviolet and infrared radiation, arc noise and electromagnetic fields.

In spite of achievements attained during the recent years the developments directed to the sanitation of the labour conditions of welders are still actual. Among them, the creation of effective systems for ventilation of industrial premises, means for individual protection of respiratory organs from WA, a main factor of a professional disease of welders, is most important [1].

The present work is the first attempt of a conceptual description of feasibility of physico-chemical support of developments which are aimed at the protection of respiratory organs of workers and environment in welding industry from effect of toxic gaseous compounds, i.e. a gaseous constituent of WA (GCWA).

Welding processes are, in principle, proceeding in open-type reactors, where the effects of high temperatures and infrared radiation cause components of coatings, fluxes and metals to intensively evaporate. Having been oxidized and condensed outside the welding arc, they form sub-micron aerodispersed particles, being accompanied by thermochemical transformations of fluorides and silicon fluorides, reduction of carbon dioxide or incomplete oxidation of organic binders in coverings and plasticizers to form HF, SiF_4 and CO. There occurs oxidation of nitrogen ($N_2 + O_2 + h\nu \rightleftarrows 2NO$). Air oxygen is transformed into ozone ($O_2 + h\nu \rightleftarrows O^{\bullet} + O^{\bullet}$; $O_2 + O^{\bullet} \rightleftarrows O_3$). Operations associated with a use of calcium carbide, which as a rule is contaminated with calcium phosphide, result in the formation of phosphine (PH_3). In the case of welding (cutting) of parts, units, structures, materials coated with preservatives, paint or (and) contaminations of a technological origin, hydrogen chloride (HCl), chlorine (Cl_2), phosgene ($COCl_2$), carbon tetrachloride (CCl_4), trichloroethylene ($CCl_2 = CHCl$), sulphorous and sulphuric anhydrides (SO_2, SO_3), hydzogen sulphide (H_2S), phosphorous (P_4), phosphorous pentoxide (P_2O_5), phosphine (PH_3) and other toxic compounds can be evolved into a gas phase.

Morphology, composition of aerodispersed particles and gas phase depend on the composition of used welding consumables and metal to be welded, type of welding, while their number depends on types and conditions of welding.

The processes of heat-mass exchange and formation of a flame are intensified by the plasma flows due to ejection and inflowing air streams.

As was noted, the welding processes are accompanied by evolution of various components of GCWA into the gas phase. Nevertheless, in spite of variety and difference in physical and chemical processes and, coming from general-theoretical conceptions, they can be divided by the following main features:

I) inorganic compounds of an acidic nature (HF, SiF_4, NO_2, HCL, Cl_2, SO_2, SO_3, ...);

II) organic compounds (CCl_4, $CCl_2 = CHCl$, $COCl_2$ ...);

III) inorganic compounds with high oxidation (O_3) and reduction (CO, PH_3) properties, and also compounds having oxidizing or reducing properties depending on the reaction medium conditions (NO, NO_2, SO_2).

It is evident that the suggested classification of GCWA is only an instruction for intelligent actions in selection of a method of trapping or (and) neutralizing of toxic substances, because a final decision is taken with allowance made for all above-mentioned requirements.

According to the definition, compounds I interact with water to form acids. Therefore, compounds of a different nature can be used to trap and neutralize them.

The use of solutions or suspensions of inorganic compounds such as alkalis (NaOH, KOH), carbonates of alkali metals (Na_2CO_3), hydroxides of alkali-earth metals ($Ca(OH)_2$, $Mg(OH)_2$), results in occurrence of chemical reactions of the acid-base and exchange interaction to form corresponding salts, water and carbon dioxide.

The class of organic compounds is diverse: compounds in the solid and liquid aggregate states, containing various ionogen groups (anionites, cationites, amholytes), can serve as the potential sorbents [2]. According to the data in [3], anionites and cationites with R and R′ matrices, respectively, can participate in reactions of neutralization, solvation, formation of acid salt compounds, splitting of salt compounds of slightly ionized ionites and oxidation-reduction:

$$ROH + HF + n\,H_2O \rightarrow RF + (n+1)H_2O\,, \quad (1)$$

$$4ROH + 3SiF_4 + (n-2)H_2O \rightarrow 2R_2SiF_6 + SiO_2 \cdot n\,H_2O\,, \quad (2)$$

$$RF + m\,HF + n\,H_2O \rightarrow RF \cdot mHF + nH_2O, \quad \text{where } m = 1-4, \quad (3)$$

$$R_2SO_4 + SO_3 + n\,H_2O \rightarrow 2RHSO_4 + (n-1)\,H_2O\,, \quad (4)$$

$$R'Na + SO_2 + n\,H_2O \rightarrow R'H + NaHSO_3 + (n-1)H_2O\,, \quad (5)$$

$$R'Na + HF + n\,H_2O \rightarrow R'H + NaF + n\,H_2O\,, \quad (6)$$

$$2ROH + 3NO_2 + n\,H_2O \rightarrow 2RNO_3 + NO + (n+1)H_2O\,. \quad (7)$$

It follows from reactions (1) to (7) that water is not only an active reagent, but also a reaction medium where the mass-exchange and chemosorption processes take place. Sorption susceptible to association of HF, due to intermolecular H-combining, causes the formation of polyhydrofluorides (3) on anionites. This results in an increased (2.5 – 3 times) sorption capacity of an anionite with regard to HF, as compared with equimolecular capacity.

Anionites containing amine groups have found the widest practical application in gas purification. Depending on the basicity (mobility of an undivided electron pair near the nitrogen atom) of primary, secondary and tertiary function of the nitrogen atom of the anionite, the acid-base interaction reactions occur with a complete or partial transition of proton. In the latter case, a less strong compound is formed and regeneration of the sorbent can occur under softer conditions. It should be noted at this point that both gel, granular and fibrous ionites are commercially produced within the required ranges. At the same time advances in fine purification during recent 10 – 20 years are justifiably related to the ion-exchange fibrous materials, as they are characterized by a large specific surface (approx. 30 – 40 m^2/g) and sorption capacity (3 – 7 mg eq/g). Aerodynamic resistance of the filter cells 10 mm thick at an air stream velocity of 10 cm/s does not exceed 2 – 3 mm H_2O and is by an order of magnitude lower than that of the granular filter operating under similar conditions.

The problem of trapping the organic compounds II is solved relatively simply: at present we can recommend to use for these purposes the activated carbon materials in the form of granules, woven and non-woven cloth [4, 5].

The situation is most difficult with compounds III, since to transform them into non-toxic or low-toxic compounds it is necessary to use decomposition (O_3) or oxidation (CO and PH_3) catalysts [6 – 9]. In our opinion, prospects for using catalysts in the welding industry depend on the content of noble metals in them, as well as on the requirements for reliable and effective operation at a temperature of the surrounding medium, atmospheric pressure, increased content of water vapours in the air and low input concentration of toxic substances (threshold limit value is 15 – 30), i.e. economy requirements and also service conditions of means of individual protection of respiratory organs (MIPRO) and devices for sanitary purification of air.

Analysis [6, 7] of the known metal, oxide and oxide-metal catalysts of dissociation of ozone and oxidation of carbon monoxide and phosphine showed that the majority of them do not meet the above requirements as they contain noble metals (silver, platinum,palladium) and silver oxide (Ag_2O) added to them in the amount of 1 to 10 wt. % [9] to increase their activity in the presence of water vapours, as well as chemosorbents introduced to absorb contact poisons [10]. This restricts the possibilities of varying their activity and complicates not only the composition of a catalyst but also the technology of its manufacture. The lack of appropriate technologies and industrial capacities in Ukraine limits evidently the feasibility of using catalysts of an ecological purpose.

We have developed efficient metal-complex catalysts (MCCs). Theoretical grounding of the possibility of purposeful controlling the activity of these catalysts is based on the concepts of intraspherical mechanisms of oxidation-reduction reactions that involve metal complexes and gaseous molecules of ozone, carbon monoxide and phosphine [6].

Also, we offered [11, 12] a relatively simple technology for the manufacture of the MCCs based on carriers of different origin (oxide, carbon). The technology allows the composition of a catalyst and, hence, its activity and stability to be varied through varying percentage of the components deposited, adding co-catalysts and activators. The synergic role of a carrier in this case effects not only the thermodynamic properties of surface complexes, but also the properties of the adsorbed water. The latter should be taken into consideration when developing the MCCs. If this phenomenon is ignored, instead of expected stabilization or increase in the catalyst activity, this may result in a negative effect due to poisoning the catalyst with the water vapours. A fundamental advantage of the MCCs is a small amount of scarce Pd (II) contained in the oxidation catalyst CO and its absence in the ozone dissociation catalysts.

Comparative characteristics of the catalysts of oxidation of carbon monoxide based on palladium chloride is given in work [13].

Mechanisms of a catalytic action of MCCs in reactions

$$2CO + O_2 = CO_2, \quad (8)$$

$$PH_3 + 2O_2 = H_3PO_4, \quad (9)$$

$$2O_3 = 3O_2 \quad (10)$$

are described in detail in [7, 12]. The basic stages of reactions (8) to (10) are the formation of surface complex, intraspherical redox-transformation of toxic molecules A = CO, PH_3, O_3 and regeneration of the catalyst.

Stage of formation of the surface complex

Depending on properties of a carrier, e.g. oxide, the surface complexes can be formed by the following reactions:

$$EOH + Me\,X_j \rightleftarrows \begin{cases} EO - Me\,X_{j-1} + HX, & (11) \\ EOH - Me\,X_j, & (12) \\ EOH(H_2O)Me\,X_j, & (13) \end{cases}$$

where EOH is the functional group of the oxide carrier ≡ Si – OH, = Al – OH, etc.; Me X_j is the metal complex and X is the ligand; the charges of the complexes are omitted.

Surface complexes according to reaction (11) are formed as a result of ion exchange. The case of a carrier with slightly pronounced ion exchange properties is characterized by the formation of complexes of composition (12), which being hydrated as a result of adsorption of the water vapours, are transformed into those with structure (13). For the latter, the possibility exists in varying the composition and regulating the catalytic activity of the MCCs within the wide ranges through changing the thermodynamic activity of ligands X and adsorbed water owing to the establishment of equilibrium:

$$EOH\,(H_2O)_xMe^{n+} + jX^- \rightleftarrows EOH\,(H_2O)_{x-j}MeX_j^{n-j} + jH_2O\,.$$

Stage of intraspherical transformation

Coordination of molecules A is accompanied by intraspherical redox-transformations which occur according to the following diagram:

$$EOH(H_2O) - \underset{\displaystyle X}{\overset{\displaystyle X}{Me^{n+}}} - A \rightarrow EOH(H_2O)\underset{\displaystyle X}{\overset{\displaystyle X}{Me^{m+}}} + B\,,$$

where B are the products of single-electron transformation of toxic materials. Depending on the nature of A, the central Me atom changes the oxidation degree (for A = = CO and PH_3 $n > m$; for O3 $n < m$). Ligand X participates in the transfer of an electron between the central atom and the coordinated molecule A. Therefore, by changing its nature it is possible to substantially change the MCCs activity at a constant Me.

Stage of regeneration of the catalyst

Regeneration of a metal complex in reactions (8) and (9) is provided by air oxygen, and in the case of reaction (10) — by intermediate products of decomposition of ozone, such as $HO_2^{\bullet}$ and H_2O_2, which are characterized by reduction properties and, for the Me^{n+}/Me^{m+} pairs, by a high redox-potential and water molecules.

To achieve a high efficiency and stability of the catalysts in purification of air from CO and PH_3, the copper co-catalyst (II) is added to their composition along with palladium chloride (II). The Cu (II) — Hg (II) catalyst can be used in the case of microconcentrations of phosphine and the Cu (II) catalyst — in the case of ozone.

It should be noted at this point that the development of ion-exchange fibrous materials and catalysts deposited on the fibrous materials simplified much the solution of design problems, as it provided a practical possibility for developing a large phase contact surface per unit volume and combining dust-trapping, gas-absorbing and catalytic elements.

The definite examples of a successful application of inorganic compounds as a sorbent of acid gases are mercerized wood $(C_6H_{10}O_5)n \cdot 3n$ NaOH [14, 15] and soda deposited on the polymeric fibrous carriers (PFC) [16], while in organic bases the urotropine in the form of aqueous solutions [17] and deposited on the PFC [16], anion- and cation-exchanging materials [18 – 21] are used and in catalysts for sanitary purification of air — from CO (Pd (II) — Cu (II) — TZK — M) [13] and PH_3(Hg (II) — Cu (II) — TZK-M) [6].

At present the theoretical base has been worked out for practical realization of deep purification of waste in welding industry. At the same time, to solve a specific problem it is necessary to take into account not only physical-chemical properties of compounds formed, but also conditions and peculiarities of operation of the MIPRO and gas-purification equipment as well as the associated technical requirements for physical-chemical and physical-mechanical characteristics of sorbents and catalysts. In practice, one has to do with MIPRO, purification devices and systems in which, in order to prevent screening of the phase contact interface of sorbents and catalysts and chemical destruction of the latter, a successive trapping of GCWA, acid components of GCWA and only then the catalytic additional purification of gases are performed.

These unique ideas are protected by numerous author's certificates of the former USSR and patents. Having no opportunity to give a full their list, we, nevertheless, considered it rational to name the most interesting design solutions in which the sorbents and catalysts developed by the authors are used. Among them, the «Snezhok» type respirators and the integrated MIRPO [7, 22 – 27], as well as devices for sanitary purification of air from welding aerosols using electrical and gas-dynamic air draught inducers with a capacity of 50 – 1500 m^3/h [26 – 28].

REFERENCES

1. Paton, B.E., Mazur, A.A., Metlitsky, V.A. *et al.* (1995) Ecological and economical aspects of fusion welding. *Avtomaticheskaya Svarka*, **5**, 40 – 44.
2. Ennan, A.A. (1975) Coordination compounds of silicon tetrafluoride and hydrofluorides of nitrogen-containing bases. In: *Thesis for Dr. Sci. (Chem.) Degree*. Odessa.
3. Vulikh, A.I., Alovyainikov, A.A., Nikandrov, G.A. (1981) New sphere of application of ionites — gas purification. *Ion Exchange*, 214 – 229. Moscow: Nauka.
4. Tarkovskaya, I.A. (1981) *Oxidized coal*. Kyiv: Naukova Dumka.

5. Ermolenko, I.N., Lyubliner, I.P., Gulko, N.V. (1992) *Element-containing carbon fibrous materials*. Minsk: Nauka i Tekhnika.
6. Rakitskaya, T.L., Ennan, A.A., Paina, V.Ya. (1991) *Catalysts of low-temperature oxidation of carbon monoxide*. Moscow: TsINTI Khimneftemash.
7. Rakitskaya, T.L. Ennan, A.A. (1992) *Physical-chemical principles of purification of gases from phosphine and phosphorus*. Moscow: TsINTIKhimneftemash.
8. Rakitskaya, T.L., Bandurko, A.Yu., Ennan, A.A., Litvinskaya, V.V. (1994) Kinetics of low-temperature dissociation of ozone by carbon fibrous materials. *Kinetika i kataliz*, vol. 35, **4**, 703 – 705.
9. Dhandapani, B., Oyama, S.T. (1997) Gas phase ozone decomposition catalysts. *Appl. Cat. B.: Environmental*, **11**, 126 – 166.
10. Irgel, L., Ehlenz, P. *Korniges Filtermittel zur Entfernung von Schadstoffen aus der Luft*. BRD Patent Application **3400764**, Int. Cl. B 01 1 20/28, 20/02. Published 25.07.85.
11. Rakitskaya, T.L., Ennan, A.A., Redko, T.D., Abramova, N.N. (1998) Technological peculiarities of production of catalysts of low-temperature oxidation of phosphine. *Ekotekhnologii i Resursosberezheniye*, **6**, 16 – 19.
12. Rakitskaya T.L., Paina V.Ya., Ennan A.A. (1998) Physical-chemical bases of silica gels choice for use as supports of metallocomplex catalysts for carbon monoxide oxidation. In: *Silica'98: Intern. Conf. (Mulhous, France), 1 – 4 Sept. 1998*, pp. 657 – 660. Mulhous.
13. Ennan, A.A., Rakitskaya, T.L., Paina, V.Ya. (1997) Catalysts of low-temperature oxidation of carbon monoxide for purification of welding aerosol. *Avtomaticheskaya Svarka*, **2**, 42 – 44.
14. Ennan, A.A., Kats, B.M., Gansh, A.I. *et al. Method for purification of gases from acid components*. USSR author's certificate **498020**, Int.Cl. B 01 D 53/04. Published 05.01.76.
15. Ennan, A.A., Rakitskaya, T.L., Baimuratov, V.I. *et al. Method for purification of gases*. USSR author's certificate **710601**, Int. Cl. B 01 D 63/10. Published 25.01.80.
16. Ennan, A.A., Rogovin, Z.A., Lishevskaya, M.O. *et al. Method for producing filter material for respirators*. USSR author's certificate **1051760**, Int. Cl. B 01 J 20/22. Published 12.10.83.
17. Ennan, A.A., Anikeev, **V.A.**, Kats, B.M. *et al. Method for extraction of hydrogen fluoride from abgases*. USSR author's certificate **287661**, Int. Cl. **B 01 D 53/14, C 01** B 87/22. Published 30.03.70.
18. Ennan, A.A., Ermolenko, I.N., Kats, B.M. *et al. Method for extraction of sulphorous gas from abgases*. USSR author's certificate **303284**, Int. Cl. **C 01 B 17/60. Published** 13.05.71.
19. Ennan, A.A., Rogovin, Z.A., Kats, B.M. *et al. Method for extraction of silicon tetrafluoride from abgases*. USSR author's certificate **330682**, Int. Cl. **B 01 D 53/14, C 01** B 7/22. Published 25.05.71.
20. Ennan, A.A., Kats, B.M., Lazarev, M.Yu. *et al. Filter material*. USSR author's certificate **581973**. Int. Cl. B 01 D 39/00, B 01 D 53/02. Published 30.11.77.
21. Ennan, A.A., Asaulova, T.A., Zheltobryukhov, V.F. *et al. Nonwoven filter material for purification of gases from acid impurities*. USSR author's certificate **1614228**, Int. Cl. B 01 D 39/08, 53/02. Published 05.01.87.
22. Ennan, A.A., Blinder, V.I., Kovalev, O.A. *et al. Respirator*. USSR author's certificate **786088**. Int. Cl. A 62 B 7/10. Published 10.06.80.
23. Ennan, A.A., Shneider, V.G., Baidenko, V.I. *Device for individual protection of humans*. USSR author's certificate **1580621**, Int. Cl. A 62 B 7/10. Published 23.07.90.
24. Ennan, A.A., Schneider, V.G. Baidenko, V.I. (1995) Versatile mask for protection of a welder. *Avtomaticheskaya Svarka*, **3**, 57 – 58.
25. Rakitskaya, T.L., Ennan, A.A., Bandurko, A.Yu. (1995) Carbon fibrous materials for respirator «Snezhok GP-Ozon». Ibid, **7**, 62 – 64.
26. Ennan, A.A., Kuusk, V.N., Butvin, A.N. *Filter*. USSR author's certificate **1119202**, Int. Cl. **B 01 D 46/02, 53/04**. Published 23.10.84.
27. Butvin, A.N., Kuusk, V.N., Ennan, A.A. *et al. Ventilation filter-absorbing plant*. USSR author's certificate **1359953**, Int. Cl. B 01 D 46/00. Published15.08.87.
28. Ennan, A.A., Butvin, A.N., Solodov, V.M. *et al.* Filter. USSR author's certificate **1041143**, Int. Cl. **B 01 D 53/04**. Published 15.09.83.

FOAM ALUMINIUM AS A NEW SUPER LIGHT-WEIGHT MATERIAL. PROSPECTS FOR ITS USE IN WELDED STRUCTURES

A.A. BONDAREV[1], N.G. TRETYAK[1], Andr. A. BONDAREV[1], V.P. BUDNIK[1] and L.A. ARBUZOVA[2]
[1]The E.O. Paton Electric Welding Institute, NASU, Kyiv, Ukraine
[2]OAO «VILS», Moscow, Russia

ABSTRACT

The properties of a new material, namely foam aluminium are given. The areas of its rational use are determined. Concrete examples are cited to show the possibility, in principle, of application of foam aluminium in welded structures, when various welding procedures are used.

Key words: *arc welding, electron beam welding, braze-welding, foam aluminium, foam materials, sheets, plates, properties of joints, sound-proofness, heat stability.*

Inorganic-base foam materials are finding ever wider application in various industries. This is primarily attributable to a combination of such unique properties as low heat conductivity and sound-proofness, as well as heat stability. More over, their density usually is less than 1 g/cm^3. Metal-base composites, for instance, foam aluminium (FA), have a special place. It features high specific strength, corrosion resistance, stops sound effectively, is a non-combustible, non-polluting material. Its application is promising in engine, ship and aircraft construction, as well as in development of high-temperature resistant or shock-absorbing devices.

VILS developed the technology of FA production based on powder metallurgy method [1]. Its essence consists in the following. Powders of alloys of Al–Mg, Al–Si, Al–Cu systems, having a wide enough solidification range, are used as the base. Powders of the so-called porofores, i.e. materials which decompose in heating and evolve a large amount of gases, are added to the powders of the above alloys. The most accessible porofores are chalk and titanium hydride evolving CO_2 and H_2, respectively. The temperature of porofores decomposition is in the range of 600 to 700 °C, i.e. it coincides with the temperature at which the aluminium alloys do not have a strength margin and the evolving gases can easily form pores in the solid-liquid aluminium alloy, leading to its foaming. The dimensions of the thus produced semi-finished products are 1000×7000 mm for 4 to 10 mm thick sheets, and 1000×2000 mm for 10 to 100 mm plates.

Foam aluminium is characterized by a unique combination of such properties which are not found to-day in any of the structural materials, namely non-combustibility, non-toxicity, low sound, heat and electrical conductivity, low hygroscopicity, low weight, good workability and appearance, which is also preserved after painting, adhesion bonding or welding.

Table 1. Properties of foam aluminium and other porous materials

Parameter	*Foam aluminium**	*AD31 aluminium*	*Wood chip boards*	*Oak boards*	*Foam concrete boards*
Density, ρ, g/cm^3	0.3 – 2.0	2.7	0.25 – 1.10	0.69	0.3 – 1.2
Hygroscopicity, wt. %	1 – 3	No data	4 – 6	12	28 – 40
Ultimate strength, MPa	45.0	250.0	0.4 – 3.5	5.0 – 123.0	0.8 – 80.0
Specific strength, σ_t/ρ, km	5.6	5.5 – 9.5	1.6 – 3.2	7.0 – 175.0	2.7 – 66.0
Young's modulus, MPa	45000	70000	0.4 – 35.0	107.7	1700 – 7500
Heat conductivity, W/(m·K)	4 – 5, poor conductor	140.0	0.046 – 0.018	0.35 (L)**, 0.17 (T)**, thermal insulator	No data
Electrical conductivity, MS/m	0.2, same	30.0, conductor	Insulators	3×10^{-6}	»
Sound conductivity, dB/cm	11.0	50.0	No data	2.4	»
Relative elongation, %	0.3 – 1.0	10.0 – 15.0	»	No data	»
Specific properties	Non-combustible non-polluting, poor heat conductor	Good conductor of heat and electricity	Difficult combustion, evolve phenols when burning	Combusible, evolve carbon gas in burning	Non-combustible high hygroscopicity

*At ρ = 0.7 – 0.8 g/cm^3.
**(L) — longitudinal texture, (T) — transverse texture.

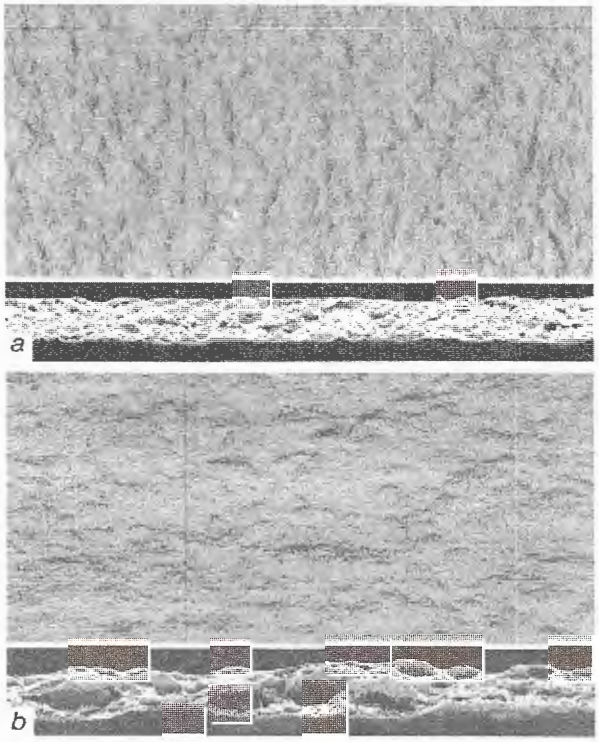

Figure 1. Appearance and cross-section of blanks from foam aluminium of different density: *a* — 0.7 g/cm^3, *b* — 0.3 g/cm^3.

The FA physico-mechanical properties, in comparison with those of other porous materials, are given in Table 1. At the density of 0.8 g/cm^3 FA heat conductivity factor is by 30 to 35 times lower than that of the aluminium wrought alloys AD1, AD31. It should specially noted that the sound conductivity coefficient in FA is lower than that of wood, by 2 or more times, and is just 1.1 dB/cm in the frequency range of 1 to 100000 Hz. For AD1 and AD31 alloys, this value is 52 dB/cm, i.e. FA can be used in different structures as a sound, electrically and thermally insulating material. FA appearance is shown in Figure 1.

Table 2. Influence of material density on the structure weight (with the same rigidity)

Material	*Density, g·cm^3*	*Sheet thickness, mm*	*Weight m_j, 1 m^2, kg*	*m_j : m PAL-3*
Steel	7.8	0.8	6.24	6.24
Titanium	4.5	1.1	4.95	4.95
Aluminium	2.7	1.2	3.24	3.24
Magnesium	1.7	1.5	2.55	2.55
Plastic reinforced with C-fibres	1.6 – 0.9	1.8 – 1.0	2.88 – 0.90	2.88 – 0.90
Oak	0.7	2.0	1.40	1.40
PAL-1	0.7	2.0	1.40	1.40
PAL-2	0.3	5.0	0.15	0.15
PAL-3	0.1	10.0	1.00	1.00

Note: Here m is weight of 1 m of a structure from PAL-3 at a specified sheet thickness; m_j is the same for the other materials.

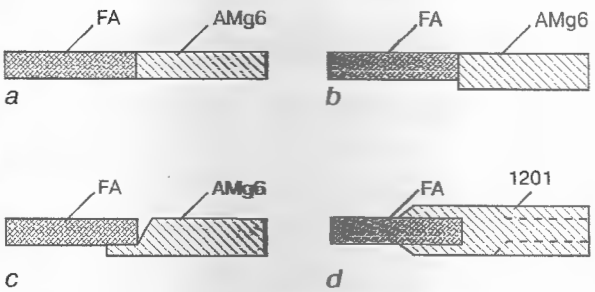

Figure 2. Schematics of edge preparation in arc welding (*a – c*) and electron beam welding (*d*) of foam aluminium to series-produced aluminium alloys.

FA looks especially attractive compared to other materials as to weight at the same rigidity (Table 2). So, a structure of a steel sheet of 0.8 mm thickness will be 6.24 times heavier, than that of PAL 3 foam aluminium (ρ = 0.1 g/cm^3), and that of titanium, aluminium and magnesium by 4.95, 3.24, 2.55 times, respectively.

FA fabrication has been so far mastered mostly in the form of sheets or plates of up to 10 to 20 mm thickness, respectively. After foaming, their thickness reaches 3 to 50 and 30 to 100 mm. The density is controlled by subsequent rolling and can be within 0.3 up to 2.0 g/cm^3.

Investigations using various fusion welding processes were conducted with the aim of widening the area of FA application and creation of a broad range of products from it. Production of joints of sheets or plates of foam aluminium to each other or to monolithic aluminium alloys of different alloying systems was of interest. Used as the blanks were sheets of FA of 0.6 to 0.7 g/cm^3 density and 4 mm thickness produced on 1995 alloy base (Al–Zn–Mg alloying system) (Figure 1). Experimental results showed that it does not seem possible to join FA blanks to each other by fusion welding. Carbon dioxide gas contained in the cavities, evolves in welding and does not allow production of a common pool of molten metal of the edges, or formation of a weld, especially in electron beam welding in vacuum [2].

In this connection FA joining through inserts of series-produced aluminium alloys seems rational. A similar joining schematics can also be used in other welded structures, where blanks produced by both the traditional technology and from foam aluminium, are used.

Figure 2 shows different schematics of edge preparation for joining blanks of the same and different thickness. A feature of the technology of arc welding is conducting the process with minimal melting of foam aluminium, with the aim of reduction of the degree of weld metal porosity. Manual arc welding was used for experiment performance in the following modes: I_w = 30 to 50 A; υ_w = 5 – 6 m/h; argon consumption — 5 to 6 l/min. In the case when blanks of the same thickness were joined (Figure 2, *a*), the best results were achieved in welding from both sides with up to 0.5 mm gap. In welding from one side weld porosity markedly increases.

Joining of blanks of different thickness (Figure 2, *b*) in welding from one side is not rational, either, as cracks often form in the zone of transition from FA to the weld metal

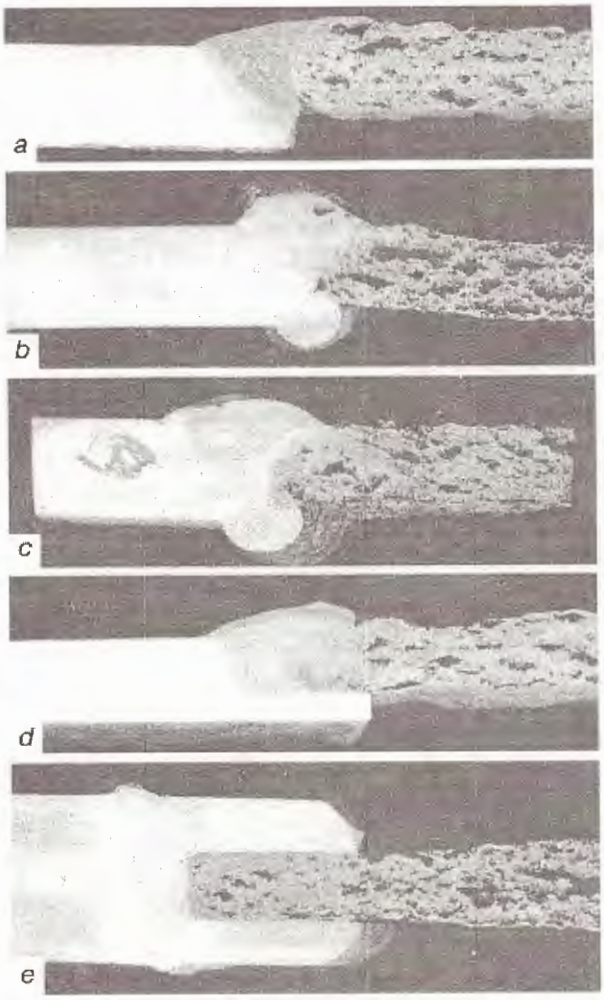

Figure 3. Macrostructure of the joints of foam aluminium with series-produced aluminium alloys, made by argon-arc (*a*, *b*, *c*, *d*) and electron beam welding (*e*) (×2).

(Figure 3, *a*, *b*). More rational is making the joint with root welding from the back side (Figure 3, *c*) or making the weld from one side on a backing (Figure 3, *d*).

Electron beam welding was performed in U212M unit using U-250 power unit in the following mode: U_{acc} = = 30 kV; I_m = 80 mA; υ_w = 60 m/h. The geometry of the butt given in Figure 2, *d*, allows reducing the interaction of the electron beam with foam aluminium and making the joint of braze-welding type (Figure 3, *e*).

During optimization of the technology, laser cutting (Figure 4) was used for cutting out blanks of the required size from FA.

The performed experiments allowed determination of the ability, in principle, of production of sound permanent joints of foam aluminium to each other and to aluminium alloys (Figure 5). The joint strength usually is equal to 0.8 to 1.0 of FA ultimate strength depending on the welding conditions and process.

Figure 4. Appearance of a cut made in FA (*a*), and side surface of the cut edge (*b*).

Figure 5. Welded model sample of a panel from 20 mm FA for thermal and sound insulation of engine compartment.

Thus, it is shown in the paper that FA, as a new material, can be used with equal success as other aluminium alloys in welded structures for various applications.

REFERENCES

1. Arbuzova, L.A., Zenina, M.V., Shmakov, Yu.V., Andreev, D.A. (1997) Foam aluminium as a new promising material for aircraft, cars and ships. *Tsvetn. Metalli*, 2, 62 – 64.
2. Bondarev, A.A., Tretyak, N.G., Bondarev, Andr. A., Arbusov, L.A. (1998) On the methods of foam aluminium joining. In: *Welding and allied technologies for the XXI century*, 14 – 15. Kyiv: The E.O. Paton Electric Welding Institute.

PLASMATRONS FOR POWDER SPRAYING OF COATINGS

V.L. DZYUBA, ODE HALIL ABU DARVISH and S.N. SERGIENKO
Donbas Mining-Metallurgical Institute, Donetsk, Ukraine

ABSTRACT

Peculiarities of design and service characteristics of plasmatrons for powder spraying and dispersion are presented. Basic parameters of the plasmatrons are estimated.

Key words: *spraying, dispersion, plasmatron, shielding gas, characteristics.*

The commercially manufactured plasmatrons intended for powder spraying and dispersion are characterized by a number of drawbacks, such as a small size of the zone of interaction with the particles heated, low efficiency and productivity in treatment, as well as short service life of electrodes. These problems have been partially resolved by the Institute of Gas of the National Academy of Sciences of Ukraine through using a gas-air mixture as the plasma gas and varying the discharge channel [1]. Plasmatrons developed by the Institute can operate in sub- or supersonic modes using an internal or remote arc. At a rated power of 30 – 180 kW, the plasmatrons with a capacity of 40 kW have an efficiency of up to 90 %. However, because of using the methane-air mixture and a short life of electrodes, they have a limited application under actual production conditions. Allowing for all these drawbacks, the authors developed plasmatrons for spraying, which could operate in air with or without a shielding gas. Schematics of the discharge channels of these plasmatrons are shown in Figure 1. It can be seen that they differ in sizes of the discharge channels, configuration, length and quantity of the inter-electrode inserts (IEI), distribution of current and gas flow rate along the channel length, location and direction of the material treated and design of individual units and components.

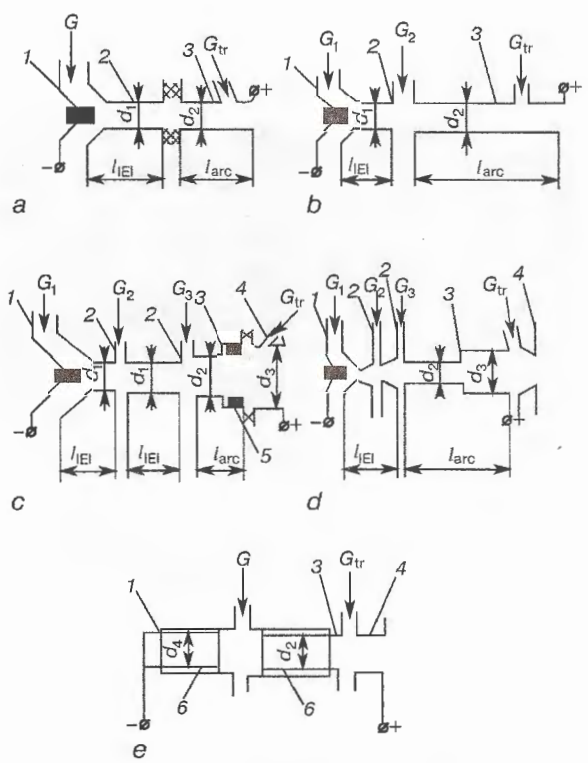

Figure 1. Schematics of discharge channels of different plasmatrons: *a* — P-9; *b* — P-10; *c* — PL-6; *d* — P-11, *e* — PL-8: *1* — cathode, *2* — IEI; *3* — anode; *4* — powder feeding unit; *5* — thermochemical inserts; *6* — screw thread.

Consider the object of our development and investigation by an example of the PL-8 plasmatron (Figure 2). This is a one-chamber linear plasmatron with a vortex-gas stabilization. It comprises cathode *1* and anode *2* units housed in collector casing *3* made from an insulating material. Air-tightness of detachable joints is provided by gaskets pressed by means of four screws. The cathode unit consists of a cylindrical cathode located in a steel cathode holder. This arrangement allows a multiple use of the cathode holder and quick replacement of the cathode in case of its failure. The cylindrical channel of the cathode has grooves threaded on its surface, which provide splitting of the arc in its cathodic zone and formation of several reference spots, thus leading to an extension of its service life. Water cavities of the cathode unit are hermetically sealed by means of a gland and a seal ring. The anode holder in the anode unit consists of a metal flange and a disk connected to each other with air-tight welds. The flange provides removal of heat from the anode. It has two diametrically opposing holes for passage of the cooling water. The disk also has water channels. The six-

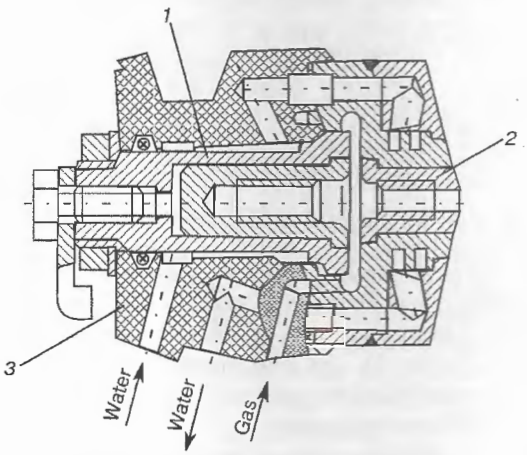

Figure 2. PL-8 plasmatron (see designations in the text).

start square thread is made on the inside cylindrical surface of the flange, on the side of the cathode holder, to provide a vortex feed of the working gas into the discharge channel of the plasmatron. The outside surface of the anode holder has a hole with a thread to connect the power terminal and secure the unit for feeding the spraying material. The copper anode is made as a hollow cylinder with transverse grooves threaded on its inside surface (similar to those threaded on the inside surface of the cathode) to split the anode zone of the arc.

For design of basic parameters of the PL-8 plasmatron, the authors used the engineering method described in [2], allowing for the data given in [3 – 5, etc.]. The source data for the design were as follows: plasma gas - air, initial air temperature — 300 K, final air temperature — 3000 K, air flow rate — $G = 1.5\times10^{-3}$ kg/s, air pressure at the plasmatron outlet — $p = 10^5$ Pa.

The relative length of the electrodes is taken as equal to $\bar{l} = l / d = 10$. To eliminate heat choking in the anode channel, its inside diameter was selected to be 10 % larger than critical, i.e.

$$d = 1.1 d_{cr} = 2.2 \sqrt{\frac{G}{\pi \rho_{cr} a_{cr}}},$$

where ρ_{cr} is the density of air at the final temperature, kg/m^3, and a_{cr} is the velocity of sound at the final temperature, m/s.

Based on the above equation, the inside diameter of the anode was 5×10^{-3} m and the discharge channel length was $l \cong 55\times10^{-3}$ m.

Determine now values of power and voltage:

$$N = \frac{G(h - h_0)}{\eta},$$

$$U = 550\, G^{0.44} d^{0.1} p^{0.25} I^{-0.29}.$$

Assuming that efficiency η for plasmatrons of the PL-8 type is equal to 0.7, the arc voltage is $U = 120$ V and arc current is $I = 300$ A.

The gas-dynamic and thermal calculations show that pressure of the working gas at the plasmatron inlet should be $p_{inp} \geq 3\times10^5$ N/m^2 and pressure of water at the plasmatron inlet should be $p_{inp} \geq 3\times10^5$ N/m. The total flow rate of the cooling water for the plasmatron should be not less than 80 g/s.

In calculation of service lives of the electrodes in the PL-8 plasmatron, the authors took into account not only their dependence on the specific erosion, which for a copper tubular electrode is equal to $\bar{G}_{sp} = 10^{-9} - 10^{-10}$ kg/C, but also their design characteristic consisting in the capability of splitting both anode and cathode zones of the arc.

The volume of the eroded material is:

$$V_{er} = 0.5\, \pi\, h_{er}\, \Delta\, l_{er} \left(d + \frac{2}{3} h_{er} \right),$$

where h_{er} is the depth of the eroded zone, m (in our case it is equal to the depth of the grooves, i.e. 1 mm for the anode and 1.5 mm for the cathode); $\Delta\, l_{er}$ is the length of the eroded zone, m (in our case it is the length of the threaded grooves, which is 11 mm for the anode and 25 mm for the cathode).

The time of continuous operation of the electrodes is

$$\tau_e = \frac{\rho\, V_{er}}{\bar{G}_{sp}\, I} n,$$

where ρ is the copper density, kg/m^3; n is the number of the simultaneous fixations of the arc to the electrode (assumed to be equal to 4).

Allowing for the assumptions made, the time of continuous operation of the electrodes (anode and cathode) is more than 70 h.

The designed specifications of the PL-8 plasmatron are as follows:

power, kW	40
arc current, A	300
working gas flow rate, kg/s	15×10^{-3}
efficiency	0.7
service life, h	> 70
expected productivity, kg/h	up to 2

Therefore, the plasmatron developed for processing of powdered materials can be recommended for commercial application in machines for powder spraying and dispersion.

REFERENCES

1. Petrov, S.V., Karp, I.N. (1993) *Air-gas plasma spraying*. Kyiv: Naukova Dumka.
2. *Fundamentals for calculation of linear-type plasmatrons* (1979) Edited by M.F. Zhukov. Novosibirsk. Nauka.
3. Zhukov, M.F., Dautov, G.Yu. *et al.* (1965) Method for design of d.c and a.c. plasmatrons. *Report*, **403/170**. Novosibirsk: IPTM SO AN SSSR.
4. Dzyuba, V.L., Dautov, G.Yu., Abdullin, Sh.Sh. (1991) *Electric-arc and high-frequency plasmatrons in chemical-metallurgical processes*. Kyiv: Vyshcha Shkola.
5. Dzyuba, V.L., Dautov, G.Yu. (1987) Design of electric-arc plasmatrons with the turbulent arc. *Problemy Spetselectrometallurgii*, **3**, 62 – 65.